Journal of Electron Spectroscopy and Related Phenomena, 48 (1989) 219–351
Elsevier Science Publishers B.V., Amsterdam — Printed in The Netherlands

Invited review

STUDY OF TRIPLET STATES AND SHORT-LIVED NEGATIVE IONS BY MEANS OF ELECTRON IMPACT SPECTROSCOPY

MICHAEL ALLAN

Institut de Chimie Physique de l'Université, CH-1700 Fribourg (Switzerland)

(Received 19 September 1988)

ABSTRACT

An elementary introduction of general aspects of electron impact spectroscopy is given, including instrumentation and application of the technique to the study of short-lived negative ions (resonances) and spin and dipole forbidden transitions of molecules.

The major part of this paper is devoted to the application of a recently developed type of instrument, the trochoidal electron spectrometer. This instrument is capable of measuring electron transmission spectra and also inelastic cross sections (a superposition of 0° and 180° scattering). The present work demonstrates that the properties of this instrument render it a broadly applicable extension of the standard instrumentation, despite the limitation of a fixed scattering angle. Its exceptional sensitivity and low energy capability make it superior to other types of instruments for many applications.

Selected results are described from electron energy-loss, electron transmission, and energy-dependence of vibrational and electronic excitation measurements, recorded in most instances with the new instrument on N_2, CO, CO_2, and nine representative polyatomic organic molecules. Dissociative attachment spectra are also presented in several cases. One section focusses on phenomena encountered in electron impact excitation of high vibrational levels. Existing data are reviewed and original research is presented. Characterization of the properties of the new instrument, and comparison with other instrument types, is accomplished by showing spectra recorded using the trochoidal electron spectrometer, which can be compared with older results obtained with other types of instruments given in the literature. Technical details of the trochoidal electron spectrometer are given in the Appendix.

TABLE OF CONTENTS

1. INTRODUCTION

1.1. Applications of electron–molecule collision studies

Electron–molecule collision phenomena play an important role in a number of systems of basic importance for science, technology and the environment. The roles played by electron–molecule collisions in many such systems have been reviewed in the monographs edited by Massey et al. [1], by Christophorou [2], and by Shimamura and Takayanagi [3]. Some representative examples of such systems and applications are listed below.

Plasmas in general [4]. These include technologically important plasmas in lasers [5, 6], plasma-etching in the electronic industry [6, 7], plasmas in diffuse discharge switches [6], plasma polymerization [8], discharges in luminescent tubes [6, 9], ionized gases in flames [6, 10] and others.

Upper atmosphere [11–13].

Ultrasensitive chemical detectors, e.g. for gas chromatography [6, 14].

Synthesis of ozone [6].

Power installations, e.g. spark-suppressors in power-switches [6, 15].

Biological systems [6, 16].

Electron-bombardment curing of polymers [17].

Knowledge of the gas-phase electron-collision phenomena is the key prereq-

uisite for understanding these systems, for the possibility of systematic intervention into them, and for optimization of the technological applications.

The capability of slow electrons to excite spin and/or dipole forbidden transitions is the basis of spectroscopic applications of electron–molecule collisions. In particular, electron energy-loss spectroscopy represents a general means of observing triplet states of organic molecules, the spectroscopic properties of which are of interest to photochemistry.

In the study of electron–molecule collision phenomena a special position is assumed by the investigation of resonances, that is of the short-lived negative ions [18]. Many ground states and most excited states of molecular radical anions in the gaseous phase are less stable than the corresponding neutral molecules, and are thus subject to autodetachment (spontaneous loss of an electron). The various electron-impact techniques are consequently in many instances the only means of investigating radical anions in the gas phase.

The studies of radical anions in the gaseous phase yield information of basic scientific interest to other areas of chemistry. Knowledge of the energy levels of the negative ion (specifically the shape resonances) provides insight into the energy levels of the virtual orbitals of MO theories, thus deepens our understanding of molecular electronic structure in general, and is of significance to the frontier orbital theory of chemical reactions. The study of dissociation of the radical negative ions (dissociative attachment), because of the special circumstances (competition with the extremely fast autodetachment), provides insight into the dynamic laws governing ultrafast (sub-ps) dissociations and thus chemical reactions in general. The knowledge of gas phase ground and excited state energies of the radical negative ions is an important prerequisite to understanding their chemistry and photochemistry in the condensed phase, where synthetic applications are starting to emerge (see for example ref. 19).

Further application of the various electron impact techniques to the investigation of the gas-phase properties of radical anions should stimulate further development of the chemistry of the anions, even in the condensed phase, in a fashion analogous to the role played by UV-photoelectron spectroscopy in promoting chemical and photochemical investigations of the radical cations, which prompted the development of other complementary experimental techniques, for example those in low temperature matrices [20].

At present the application of the electron-impact methods to chemistry-related problems appears to be much less widespread than investigation of the radical cations by UV-photoelectron spectroscopy. This is probably due not only to the greater complexity of the required apparatuses, but also to the more difficult interpretation of the experimental results, caused by the short lifetime of the anions and a multitude of other scattering phenomena besides the short-lived negative ions, which also influence the measured scattering cross sections.

The most important chemically relevant studies of radical anions have been

made by electron transmission spectroscopy (ETS) [21–23], probably because of the relatively simple instrumentation required for this experiment and its relatively wide applicability. ETS, however, when used alone suffers from certain drawbacks. The information obtained is spectroscopic, i.e., energy levels, and no indication of the decay channels is obtained. Furthermore, some types of negative ion states cannot be observed because they affect the total cross section only very weakly, and it is often difficult to identify weak and broad bands on the background of direct scattering, inherent to this method, which is also energy dependent.

A need for more comprehensive studies therefore exists, which would provide a more detailed picture of the electronic structure of the negative ion. This information may be obtained by the combined application of several electron-impact methods, probing several, often competing decay channels of the negative ion states. The four most relevant types of spectra are the electron-transmission spectrum (ETS), the energy-loss spectrum (ELS), the energy-dependence spectrum (EDS), measuring the efficiency of a given vibrational or electronic excitation as a function of the incident electron energy, and the dissociative attachment spectrum (DAS) [18]. Studies in which all four methods were applied simultaneously to a given sample and which cover wide energy ranges, e.g. 0–10 eV, are relatively rare, particularly for organic molecules, because they require a large investment of both instrumentation and investigation time.

The trochoidal electron spectrometer developed in Fribourg [24] has properties which facilitate such combined studies on more extended series of compounds. It is simpler in construction than the more conventional electrostatic instruments, its high sensitivity permits reasonably short acquisition times in most instances and it is also suitable for recording transmission spectra. Its most important drawback is the inability to vary the scattering angle, but as the examples in this work will show, a comprehensive picture of the radical-anion properties may in general be obtained with this instrument in spite of this limitation. Together with a standard dissociative attachment spectrometer, also available in our laboratory [25], it is possible to obtain all four essential types of spectra, ETS, ELS, EDS, and DAS using only two instruments.

Besides providing a brief general introduction to the mainly chemistry oriented applications of the various electron spectroscopic techniques, the goal of the present work is to illustrate the properties and the potential of the trochoidal electron spectrometer. The application of this instrument to the study of a number of mostly organic molecules is presented. To provide a comparison with other types of instrument, spectra obtained with the trochoidal electron spectrometer are shown, which can be compared with similar, previously published, spectra obtained with other types of instrument. The technical description of the trochoidal electron spectrometer is given in an Appendix. It is the author's hope that the present work will contribute to the further promotion

of the chemistry-oriented applications of electron impact spectroscopies, the potential of which we are only beginning to exploit.

1.2. Brief historical perspective

This section highlights some major developments in the electron scattering field. Space does not allow for a comprehensive representation and the events highlighted have admittedly been chosen somewhat arbitrarily. A more comprehensive account may be found in the review articles cited below.

The first measurements on electron collisions were conducted soon after the discovery of the electron. In their classic experiment Franck and Hertz [26] were able to measure discrete electron energy losses in mercury vapour and were thus able to provide early evidence for the quantum nature of matter in a particularly transparent way. Its fundamental importance has justly made this experiment a standard subject of undergraduate textbooks of physical chemistry (see for example the book of Berry et al. [27]).

The research field of electron–atom (molecule) collisions subsequently became active in the 1930s, when a number of different aspects of electron scattering cross sections were investigated and related to the then young quantum theory. A comprehensive review of this work has been presented by Massey and Burhop [28].

The early experiments had many limitations, for example insufficient vacuum and low resolution, not permitting the observation of narrower structures in the cross sections. It was the technological developments such as better vacuum techniques, electron monochromators, and electron multipliers, which permitted a renaissance of the electron scattering field in the 1950s and 1960s. An account of the development in this period, and in particular of the impetus given to research by the discovery of short-lived negative ions first in molecules and later in atoms, as well as of the substantial contributions made by G.J. Schulz, has been given in a Physics Today article by Biondi et al. [29].

Starting with this renaissance the field appears to be steadily gaining momentum. The research is developing along several, to some degree overlapping, directions, such as the study of elastic collisions, molecular excitation and dissociation, and collisional detachment. These developments have been extensively documented in the two classical review articles of Schulz [18]. The entire width of the electron-impact field and related areas has been documented in two previously mentioned monographs [2, 3], where a number of references to other excellent review articles may be found.

The beginning of applications to chemistry may perhaps be set at about 1965, when several groups initiated studies of hydrocarbons and other organic molecules, often using the trapped-electron or the SF_6^- scavenger methods [30–34] and the electron transmission techniques [35].

An important advance has been the application of the ETS-technique of

Sanche and Schulz [36] to organic molecules [37, 38]. The applications of this approach to problems relevant to chemistry have subsequently been pioneered by Jordan and Burrow [21–23]. This fruitful direction is now being adopted by a number of groups (see refs. 22, 39–42 for recent representative examples); a recent review containing a bibliography of the work published on ETS has been published by Jordan and Burrow [23]. This approach has yielded a wealth of fundamental knowledge of the electronic structure of the radical anions of organic molecules, their relation to the electronic structure of the neutral compounds, to the virtual orbitals, to the complementary relationship between the anion and the cation energies (the latter determined by UV-photoelectron spectroscopy) in alternant hydrocarbons, and in some cases to their reactivity [43, 44]. The relation of the gaseous phase ET-spectra to absorption spectra of radical anions in the condensed phase has also been investigated [22, 45].

The capability of electron-impact spectroscopy to excite forbidden transitions in molecules is also being exploited by several research groups with regard to organic molecules. References to representative work and review articles will be given in Section 3.1.

Our understanding of the electron scattering phenomena has been made possible by the great efforts of theory. Introductory treatments of the theory may be found for example in the articles by Herzenberg [46] and Morrison [47]. Advanced aspects of the subject have been reviewed and critically compared with experimental results by Lane [48]. A recent review of ab initio calculations of the electronic structure of anions, including resonances, together with a bibliography, has been given by Simons and Jordan [49].

2. BASIC ELECTRON IMPACT PHENOMENA

2.1. Electron–molecule collisions

An electron–molecule collision is shown schematically in Fig. 1. An electron with a given incident kinetic energy E_{in} collides with a gaseous target molecule. The electron interacts with the molecule and may lose (or gain if the target was excited) kinetic energy to (from) the internal excitation of the target. The collision is called inelastic in the former, and superelastic in the latter case. (Electron scattering in organic molecules offers in principle an additional possibility, analogous to chemiluminescence, where the energy of a ground state, but energy-rich molecule could be converted to the kinetic energy of the scattered electron. No case of such "chemically superelastic" scattering has, however, yet been reported.) The excitation may be rotational, vibrational, and electronic. Since the electron is much lighter than the molecule, the excitation of the translational motion is negligible and the energy distribution of the scattered electrons is related to the energy level scheme of the target, that is

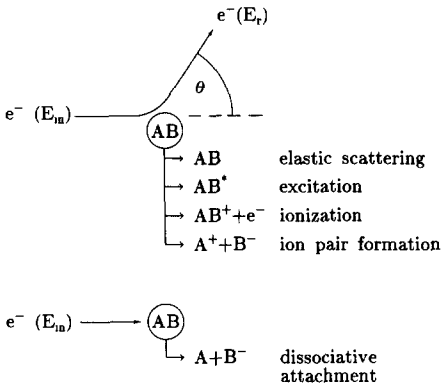

Fig. 1. Schematic diagram of a general electron scattering process with some of its possible outcomes. The incident electron with a known energy E_{in} strikes a target molecule AB, may lose the energy ΔE to the target, and is scattered into the direction θ with the residual energy E_r. The excited target AB* may further emit a photon or dissociate (dissociative excitation). The target may also permanently capture the electron and dissociate into a neutral fragment and a stable negative fragment, as shown in the lower part of the figure.

$$\Delta E = E_{in} - E_r = E_{el} + E_{vib} + E_{rot}$$

where E_{in} and E_r are the incident and residual energies, ΔE is the energy loss, and E_{el}, E_{vib}, E_{rot} are the electronic, vibrational, and rotational excitation energies. The scattered electron intensity is related to the corresponding cross section and is the subject of measurement in spectrometric investigations. The angular distribution is determined by the nature of interaction and contains information concerning the properties of the states involved in the excitation process.

2.2. Definitions of scattering cross sections

A convenient measure of the "scattering power" of the target molecule for electrons of a given energy is the scattering cross section, which can be understood in the following manner [50]. Suppose a beam of electrons enters a collision chamber which contains a low-pressure gas. The beam intensity I decreases as a function of the distance l along the beam in the gas chamber. Since the fractional loss of the intensity should be proportional to the number density N of the gas molecules, we have

$$dI = -\sigma_T \cdot I \cdot N \cdot dl$$

or

$$I_t = I_0 \cdot \exp(-\sigma_T \cdot N \cdot L)$$

where L is the length of the collision chamber, and I_0 and I_t are the incident and transmitted electron currents. The constant σ_T has the dimension of area and is called the total collision cross section.

If the electron were a classical point mass and the target atom a rigid sphere with a radius a, the collision cross section would be simply given by the geometrical cross section πa^2. The real electron, however, follows quantum mechanics and the wave nature of the electron comes in. Furthermore, the target atom or molecule has no defined boundary. For these reasons the collision cross section is not a constant, but depends on the collision energy E_{in}.

Very often the collision may have many different outcomes and it is desirable to distinguish all these individual processes. Often the angular distribution of the scattered electron is also required. When we look at the excitation to a discrete final state n and an electron going into a small solid angle $d\Omega$ in the direction (θ,ϕ), we can define the customary differential (in angle) cross section $d\sigma_n(E_{in},\theta,\phi)/d\Omega$.

In most scattering experiments the target molecules are randomly orientated and one can determine only cross sections averaged over molecular orientation. For this reason the differential cross section becomes independent of the azimuthal scattering angle ϕ. Furthermore, the measuring apparatus has associated with it a finite energy and angular resolution and the measured cross section represents a value averaged over these experimental variables. This measured differential cross section, at a given impact energy, is denoted as

$$DCS_n(\theta,E_{in}) = d\sigma_n(\theta,E_{in})/d\Omega$$

Integration of the differential cross section over all scattering angles yields the integral cross section

$$\sigma_n(E_{in}) = 2\pi\int (d\sigma_n(\theta,E_{in})/d\Omega)\sin\theta d\theta$$

The total (sometimes called "grand total") electron scattering cross section mentioned above is the sum of the integral cross sections for all energetically accessible processes

$$\sigma_T(E_{in}) = \sum_n \sigma_n(E_{in})$$

In many experiments the gas density (pressure) and the absolute sensitivity of the instrument are not known exactly and only relative cross sections (ordinate in arbitrary units) are obtained. The more elaborate experiments determine absolute cross sections.

In a certain class of experiments, where the diffusion of electrons in gases is investigated (swarm experiments), the variable obtained from the experiment is the so called momentum transfer cross section. This is the differential cross section integrated over all scattering angles and simultaneously "weighted" by an angle dependent factor $(1-\cos\theta)$, that is, for elastic scattering

$$\sigma^{m} = \int \sigma(\theta,\phi)\,(1-\cos\theta)\,d\Omega$$

The momentum transfer cross section is thus smaller then the total cross section for predominantly forward scattering, and larger for predominantly backward scattering.

2.3. Resonances in electron scattering

At certain incident energies the incident electron may be temporarily trapped in the field of the molecule and a short-lived negative ion occurs as an intermediate state in the scattering. This type of scattering is called resonant (as opposed to "direct" scattering) and the short-lived anion is often called a "resonance" [18]. The resonance causes a structure (often an enhancement) of certain scattering cross sections and may therefore be observed as a relatively narrow structure (often a peak) in the dependence of suitable cross sections on the incident electron energy. The negative ions discussed in this work, being formed by electron attachment to a closed shell molecule, are odd electron species, that is radical anions in chemical terminology.

The formation and decay of a resonance may be viewed as a two-step process, i.e., attachment and detachment, as is schematically shown in Fig. 2. One may thus define the attachment cross section and the branching ratios of the different decay processes.

2.3.1. Classification of resonances

In the discussion of the electronic structure of resonances a very useful concept is that of a parent (electronic) state. This is the state of the neutral molecule, which is obtained by the formal removal of the "extra" captured electron. A resonance whose configuration differs from the configuration of the target molecule only by the addition of one electron (into a virtual orbital), that is a "one particle" (1p) resonance, has the electronic ground state as a parent state. The "two particle–one hole" (2p–1h) resonances have an electronically excited parent state, whose configuration is obtained from the configuration of the target by promoting one electron from an occupied into an unoccupied orbital and capturing the incident electron in an unoccupied or-

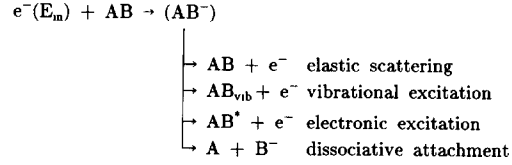

Fig. 2. Scheme of resonant electron scattering as a two-step process, with some of the possible decay channels of the resonance.

bital. (Note the analogy with the 1h ("Koopmans") and the 2h–1p ("non-Koopmans") states of positive ions.) A resonance may thus decay into its parent state by a one-electron process and the decay of a resonance into its parent state is, if energetically possible, in general the preferred decay channel. In some cases it is useful to invoke a parent vibrational state.

There are two mechanisms of temporary capture of an electron to the molecular core:

(a) The electron is trapped by the "shape" of the potential, which must have a centrifugal barrier. This case is called a *shape resonance.* The angular momentum must not be equal to zero, that is shape resonances are generally assumed not to occur in s-wave scattering. The shape resonance lies energetically above its parent electronic state and often decays into it very efficiently, resulting in a short lifetime.

(b) The electron is trapped by an excitation (electronic or vibrational) which it has induced, if the resonance lies energetically below its parent state. This case is called a *Feshbach resonance* (electronic in the former, nuclear in the latter case). The decay of the Feshbach resonance requires a change of the electronic configuration (or vibrational state) of the core since the decay into the parent is energetically not possible, often resulting in a longer lifetime.

The lifetime of the resonances, determined by the efficiency of the electron trapping, may often be determined indirectly from the energy broadening of the observed features and lies in the 10^{-13}–10^{-15} s (1–100 fs) range in most cases, although longer lifetimes may be encountered at low energies and with Feshbach resonances. Because of the uncertainty principle, the short lifetimes often result in energy widths of several tenths of an eV to several eV, discernible even with the moderate resolution of electron spectrometers. The longer-lived resonances typically display well defined structure due to nuclear motion, whereas those in which the electron detaches in a time short compared to that required for appreciable motion of the nuclei are broad and featureless. An introductory level discussion of these phenomena has been given by Herzenberg [46].

The often encountered types of resonances are:

(a) The "simple" or 1p shape resonances, whose parent is the electronic ground state of the molecule. The formation of the 1p shape resonances, being a one electron process, is characterized by a large attachment cross section and they are consequently pronounced in experiments relying on total cross section, like transmission spectroscopy. Their preferred decay channel is in general the formation of the parent electronic state, often accompanied by vibrational excitation. Energy dependence of vibrational excitation is thus a second suitable means of observing them. The energies of the 1p shape resonances are often interpreted in terms of virtual orbital energies and Koopmans' theorem [49], providing valuable information on the unoccupied orbitals of a molecule.

(b) The "core excited" or 2p–1h shape resonances result when electron cap-

ture is accompanied by electronic excitation. The parent state is in general a valence state but may also be a Rydberg excited state of the molecule. These resonances are not or are only weakly observed in the transmission spectrum because their formation from the electronic ground state, being a two electron process, is characterized by a small attachment cross section, and they affect the total cross section only weakly. The core excited shape resonances do, however, often decay into their parent electronically excited states and may be observed in the excitation functions of these states. The distinction between "simple" and core excited resonances is often only approximate and not always applicable because states of temporary negative ions are sometimes encountered, which show the characteristics of both simple and core excited shape resonances, indicating mixing of both the (1p) and the (2p–1h) configurations. Dramatic examples of such configuration mixing are found in *p*-benzoquinone [51, 52], and in naphthalene and anthracene [22, 23].

(c) The 2p–1h Feshbach resonances often have a Rydberg state of the target molecule as a parent, but many organic molecules with larger electron affinities are also expected to have valence Feshbach resonances. Having the decay channel into the parent state closed, they often have longer lifetimes and pronounced vibrational structure. They have a multitude of decay channels, such as elastic scattering, dissociative attachment, and the ejection of very slow electrons in molecules. Suitable means of their observation in molecules are the dissociative attachment and the threshold electron spectra. Their narrow width renders them more easily discernible on the large background of direct scattering and therefore also observable with lower intensity in the electron transmission experiments and (in atoms) in energy dependence of electronic excitation. The Feshbach resonances associated with Rydberg states of the target molecules have band shapes very similar to the band shapes of the *parent* Rydberg state and the *grandparent* state of the positive ion (photoelectron spectrum).

TABLE 1

Classification of resonances

Configuration	Energy vis-a-vis parent	Parent	Name of resonance
1p	Above	Ground electronic state	"Simple" shape
2p, 1h	Above	Electronically excited state (often valence)	Core excited shape
2p, 1h	Below	Electronically excited state (often Rydberg)	Feshbach

(d) The nuclear excited Feshbach resonances occur at low energies and may be important in s-wave scattering.

The classification of resonances is summarized in Table 1.

2.3.2. Trapping mechanism in shape resonances

This section describes qualitatively the trapping mechanism of an electron in a one-particle shape resonance with the aim of illustrating the nature of autodetaching electronic states of the anions. A conceptually useful picture of temporary anion formation has been developed from studies on atoms and diatomic molecules [18]. Jordan and Burrow [21, 53] have discussed qualitatively how the essential ideas may be carried over to polyatomic organic molecules.

Let us first consider electron scattering from the spherically symmetric potential field of an atom. The incident beam of electrons may be represented as a plane wave containing all components of angular momentum. If the atom possesses an energetically accessible unfilled orbital, characterized by a particular value of the orbital angular momentum l, then an incident electron with this appropriate orbital symmetry may be temporarily "captured". Figure 3 illustrates the qualitative form of the potential encountered by the incoming electron. At large electron–atom separation the interaction consists of two important terms, an attractive polarization potential and the repulsive centrifugal potential associated with the angular momentum of the electron

$$V(r) = -\alpha/2r^4 + l(l+1)/2r^2$$

where α denotes the polarizability and l the angular momentum associated with the orbital into which the electron is captured. When $l \neq 0$, these two terms

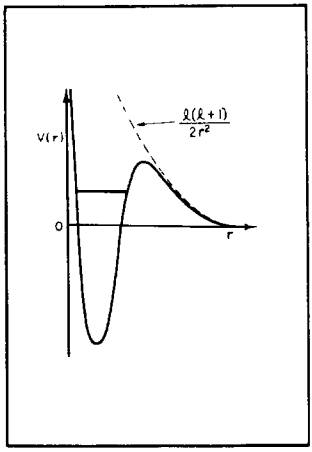

Fig. 3. Hypothetical potential curve of an electron with angular momentum l in the field of an atom as a function of the electron-atom separation. (From ref. 21.)

in general combine to form a barrier. The usual view is that in the absence of an angular momentum barrier, there is no temporary electron capture or time delay of the scattered electron [46]. At closer distances, a pronounced dip is produced by the short-range screened Coulomb forces. If the energy of the incoming electron is appropriate, that is its wavefunction "fits" into the potential well, it becomes accumulated there, forming the temporary negative ion. The resonance has a finite lifetime due to back-tunnelling of the electron through the angular momentum barrier. The term "shape" resonance refers to the fact that the electron is temporarily bound because of the "shape" of the potential field it experiences. Examples of such pure *p*-wave and *d*-wave shape resonances in atoms are provided by the ETS measurements in Mg, Zn, Cd, and Hg [54].

The concept of shape resonances can be extended to molecules, although the situation becomes more complex because of the noncentral potential in which the electron moves. Quantitative electron–molecule potentials are obtained in certain theoretical treatments [55] and examples of such quantitative potentials are given in Fig. 4. These calculations show that the anisotropy is quite weak for non-polar (and weakly polar) molecules; for example H_2 is not much more than a large atom from the point of view of the incoming electron.

The energy of the anion state is largely determined by the strength of the attractive portion of the potential. The lifetime of the temporary anion is a function both of the size of the barrier, which is strongly dependent on *l*, and of the anion energy since the combination of these factors determines the relative height and thickness of the barrier through which the electron must tunnel in order to detach. This point is illustrated in Fig. 5, which shows model potentials given by Teillet-Billy [58] for three extreme cases of diatomic molecules. In N_2, with a high barrier, a resonance is found at 2 eV with a lifetime sufficiently long to show vibrational structure [18]. In H_2, with a lower barrier, an extremely short-lived resonance is found, with no vibrational structure in most channels of observation [18, 59]. In HCl the barrier is absent and no shape resonance is found at low energies [46, 60].

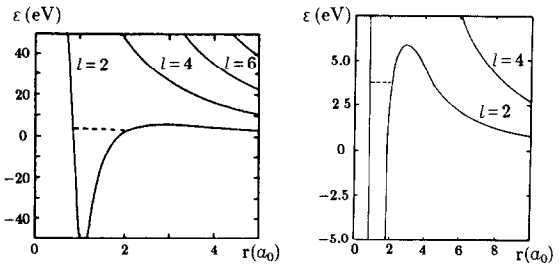

Fig. 4. Quantitative static electron–molecule potential curves for N_2 for several values of *l*. The curves are shown vertically expanded on the right for better visibility of the barrier. The $^2\Pi_g$ resonance is indicated by a dashed line. (From refs. 56 and 57.)

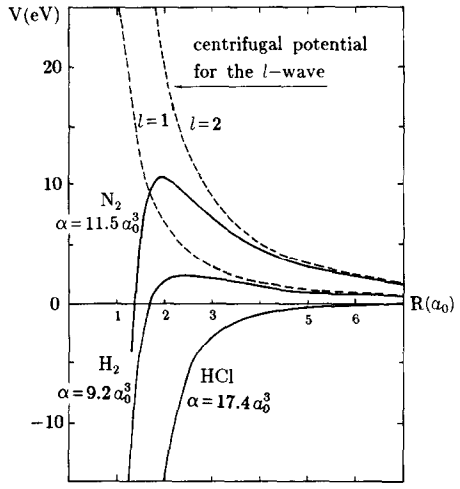

Fig. 5. Electron-molecule potential curves for H_2 ($l=1$), N_2 ($l=2$), and HCl ($l=0$), as given by Teillet-Billy [58]. The barriers of varying height are formed by the repulsive centrifugal potential and the attractive polarization potential of varying strength.

In molecules, each unoccupied orbital of the target molecule has a characteristic charge distribution whose symmetry determines the possible angular momentum components which may be captured. The relative contribution of these components will be determined by the detailed shape of the orbital. For molecules with a high degree of symmetry, only the lowest few allowed components will be necessary to describe the scattering behaviour. These important angular momentum components can be visualized by expanding the orbital charge distribution in spherical harmonics.

For example the $^2\Pi_g$ shape resonance of N_2 is well described by a d-wave angular scattering contribution. CO, on the other hand has important $l=1$ and $l=2$ components in its angular distributions, the former arising from the different size of the oxygen and carbon $2p$ orbitals. Molecules such as benzene and ethylene have sufficiently high symmetry that their shape resonances should be dominated by a single angular momentum component. On the other hand, many polyatomic molecules with no overall symmetry have been found by ETS to have shape resonances [21]. This implies that the wavefunctions of the "extra" electrons in these systems have a sizeable mixture of components with $l>0$.

2.4. Nonresonant electronic excitation

Understanding of the mechanism of electronic excitation by electron impact is crucial for the second application of electron-impact spectroscopy, the de-

tection of forbidden transitions in neutral molecules. The electronic excitation may be *resonant* or *nonresonant* ("direct").

In particular the core excited resonances decay strongly into the electronically excited states and the energy loss spectra recorded at energies up to about 5 eV above threshold are often dominated by the resonant mechanism (see, e.g. refs. 24 and 61). The spin-forbidden transitions are strongly observed in this range of E_r, and the different preferred decay channels of the different resonances may be used to sort out several transitions. Recent theoretical work of Teillet-Billy et al. [62] and Gauyacq et al. [63] suggests that within the first few electronvolts above threshold even what might on first sight appear as a nonresonant contribution to the excitation cross section is in reality resonant excitation caused by shape resonances lying several electronvolts lower.

The rest of this section concentrates on the nonresonant excitation mechanism, which appears to be dominant at higher residual energies, above ≈ 5 eV. Brief discussions of the relevant theory may be found in the review articles of Trajmar and Cartwright [50b], Lassettre and Skerbele [64] and Hudson et al. [65]. Two basic physical phenomena lie behind the angular and incident energy dependence of electron-impact transition intensities.

(a) *Electron exchange* scattering contributes to spin-forbidden transitions. The short-range nature of this interaction results in a nearly isotropic angular distribution. In order for the exchange terms to be large, the wavelength of the incident electron must be comparable to the "wavelength" of the valence electrons of the target, that is roughly 2–20 eV above threshold. At 50 eV above threshold the cross sections will have fallen by more than two orders of magnitude.

(b) Spin-allowed transitions can be induced by the *Coulomb interaction* between the incident and the molecular electrons. Since it is a long-range interaction it can be caused by large-parameter collisions, which produce little deflection for high-energy electrons, resulting in forward-peaked scattering.

The intensities of the spin-allowed transitions are conveniently discussed in terms of the apparent generalized oscillator strength f^{AG} and the momentum transfer $\mathbf{K}$, two variables which are more directly related to the physics of the excitation than the differential scattering cross section DCS and the scattering angle θ. The momentum transfer is the momentum transferred to the target during the collision, illustrated in Fig. 6. It is given by the relation (see for example ref. 66)

$$(Ka_0)^2 = (1/R)\{(2E_{in} - \Delta E) - 2\sqrt{E_{in}(E_{in} - \Delta E)}\cos\theta\}$$

where K is the momentum transfer in Å^{-1}, $a_0 = h^2/me^2 = 0.5292$ Å the Bohr radius, $R = me^4/2h^2 = 13.602$ eV the Rydberg energy, θ is the scattering angle, and E_{in} and ΔE are the incident energy and energy-loss in eV. The momentum transfer approaches zero in the limit of high incident energies and low scatter-

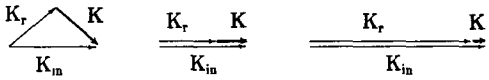

Fig. 6. Examples of the momentum transfer vector **K**. ΔE has the same magnitude for the three parts of the figure. **K** becomes larger as θ is increased or E_{in} is decreased.

ing angles, and increases both with decreasing electron energy and increasing scattering angle.

The apparent generalized oscillator strength is a convenient expression for the electron-impact transition intensity [67–69]. It can be calculated from the experimental differential cross sections DCS using the expression

$$f_n^{AG}(K) = 0.5\Delta E(k_0/k_n)K^2 \mathrm{DCS}_n(K).$$

It is a function of the differential cross section $\mathrm{DCS}_n(K)$, for excitation to the state n as a function of the momentum transfer K. k_0 and k_n are the magnitudes of the electron momentum before and after scattering, and ΔE is the energy loss.

Theoretically, f^{AG} may, within certain approximations, be expressed in powers of the magnitude of the momentum transfer and the resulting expression offers a valuable insight into the behaviour of the electron impact intensities as a function of the incident energy and the angle [64, 65]

$$f_n^{AG} = 2\Delta E[\mu_1^2 + (\mu_2^2 - 2\mu_1\mu_3)K^2 + (\mu_3^2 - 2\mu_2\mu_4 + 2\mu_1\mu_5)K^4 + \ldots]$$

where μ_1 is the transition dipole moment, μ_2 the transition quadrupole moment, μ_3 the transition octupole moment, etc. f^{AG} thus converges to the optical oscillator strength f_{opt} and the dipole-selection rules become active in the zero momentum-transfer limit ("the limit theorem"). This limit may only be approached, but not reached experimentally, because even for $\theta = 0$ and high impact energies, the momentum transfer is small, but nonzero. f_{opt} may, however, be obtained by extrapolation [70].

Dipole forbidden ($\mu_1 = 0$), but quadrupole allowed ($\mu_2 \neq 0$) transitions will become observable with higher momentum transfer, when the second term in the expansion becomes nonzero. The dependence of the generalized oscillator strength on the momentum transfer is thus a curve characteristic of a particular transition. An example of three such curves, calculated by Read and Whiterod [71] for three transitions in benzene are given in Fig. 7 (see also discussion by Ziegler and Hudson [68]). In instances where this dependence was obtained experimentally, such as for the $^1B_{2u} \leftarrow {}^1A_{1g}$ first singlet–singlet transition in benzene (ref. 72, reviewed in ref. 68), it was very helpful in characterizing the transition. Obtaining this curve is, however, experimentally very tedious and in practice the dipole forbidden transitions are simply sought under conditions of nonzero momentum transfer. One thus obtains qualitative rules for the observation of the different types of transitions:

(1) Conditions suitable for the observation of the spin-forbidden transitions with variable angle instruments are low residual energy E_r and a large scattering angle θ.

(2) At conditions of small momentum transfer, that is $\theta=0$ and high electron energies, the dipole allowed transitions are almost exclusively observed, and the energy loss spectrum strongly resembles the optical absorption spectrum.

(3) The spin-allowed, dipole-forbidden transitions are best observed at intermediate electron energies, where the singlet–triplet transitions are no longer strongly excited and do not congest the spectrum, and at conditions of nonzero momentum transfer, i.e., at nonzero scattering angles.

(4) The trochoidal electron spectrometer described in this work permits the variation of E_r, but not θ. The values of momentum transfer (in $Å^{-1}$, for $\Delta E=5$ eV), which may readily be realized with this instrument range from about 0.27 ($E_r=20$ eV, $\theta=0°$) to about 2.76 ($E_r=5$ eV, $\theta=180°$). (The trochoidal spectrometer accepts electrons scattered into 0° and 180°, see Appendix.) Singlet–triplet transitions are best observed at $E_r=0$–3 eV where they are resonantly excited, and dipole-forbidden transitions may be observed at intermediate residual energies $E_r=1$–10 eV where relatively large momentum transfers are realized and the intensity of the singlet–triplet transitions starts to diminish. The spectrum generally becomes very similar to the optical spectrum for $E_r \gtrsim 20$ eV.

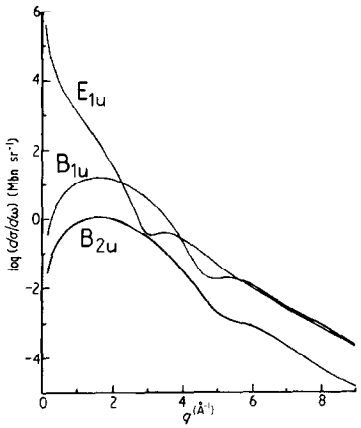

Fig. 7. Calculated differential cross sections for the excitation of three benzene transitions as a function of the momentum transfer q (from ref. 71). The dipole-allowed $^1E_{1u} \leftarrow {}^1A_{1g}$ transition peaks at zero momentum transfer; the two dipole-forbidden transitions must be observed in experiments with higher momentum transfer.

3. ELECTRON IMPACT EXPERIMENTS

3.1. Overview of instrumentation

The general instrumental arrangement required for electron impact spectroscopy is depicted schematically in Fig. 8. The fundamental parts are a source of nearly monoenergetic electrons, a collision region filled with a diluted gas, an energy analyzer for the scattered electrons or stable fragment negative ions, and a collector for the unscattered electron beam. Since negative ions may also emanate from the collision region, and generally follow the same paths in electrostatic systems as electrons, some mass selective device, with a resolution sufficient at least to differentiate ions from electrons, is also desirable, although not always incorporated in real instruments. (The lack of the mass filter generally does not cause problems because the dissociative attachment cross sections are much smaller than the inelastic electron scattering cross sections, but cases of misinterpretation of data have been reported [73].)

The electrons are usually taken from a hot filament, then passed through the monochromator, that is an energy dispersing device which selects a narrow slice from the initially broad energy distribution. The electrons pass the monochromator with a suitable low and fixed energy, are then accelerated (or decelerated) to the desired incident energy by means of a variable voltage V_M and enter the collision region. The electrons scattered in a particular direction θ are first decelerated (or accelerated) to a fixed energy suitable for the operation of the analyzer; those which pass its transparency window are counted. In instruments studying the dissociative attachment the stable fragment an-

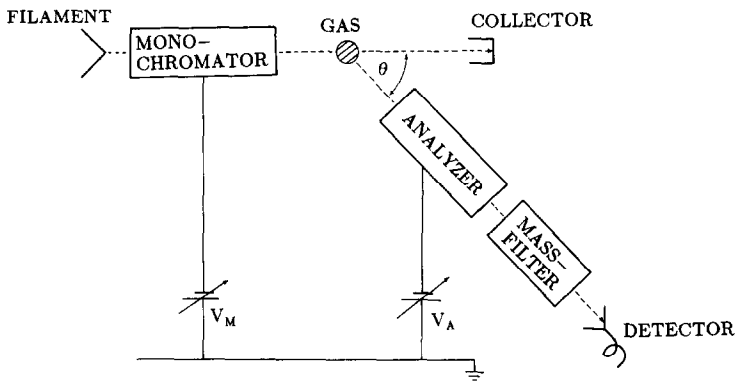

Fig. 8. Schematic diagram of the general instrumental arrangement for electron-impact spectroscopy. Electrons emitted from the filament pass through the monochromator with a low fixed energy and are then accelerated (or decelerated) to the desired collision energy E_{in} by means of a variable voltage. Scattered electrons (or stable negative ion fragments) are collected at an angle θ, decelerated to the pass energy of the analyzer, energy- (and possibly also mass-) analyzed and counted.

ions are collected, energy analyzed, and should pass a mass filter before detection.

Several realizations of the general arrangement of Fig. 8 have been developed in various laboratories. They differ mainly in the type of the energy dispersing elements used in the monochromator and the analyzer (e.g., cylindrical or hemispherical electrostatic, trochoidal, or a Wien-filter), in whether they use a stationary gas sample in a collision chamber or a molecular beam, type of mass filter (e.g., sector magnet, quadrupole, time-of-flight) and other technical details. One important class of instrument, the electron transmission spectrometers, lacks the analyzer altogether. The instrumental considerations will be discussed in greater detail in section 4.

3.2. Spectra

Four different types of spectra may be obtained with the general arrangement shown in Fig. 8, although most real instruments are specialized and not able to record all four.

3.2.1. Electron transmission spectrum (ETS)

In the electron transmission experiment the analyzer is not used and the total "transmitted" electron current I_t arriving at the collector is monitored. From the drop of the electron current caused by the gas the approximate (because of certain limitations imposed by the incomplete rejection of the scattered electrons [74]) total scattering cross section σ_T is determined as a function of the incident electron energy (see Section 2.2.). The existence of a temporary negative ion often causes a relatively narrow structure in the total cross section and electron transmission spectroscopy is therefore used as a means of determining the electronic states of the negative ion. To improve the visibility of weak variations of the cross section caused by resonances ET spectra are often shown in the derivative representation, displaying the derivative of the scattered current, dI/dE_{in}, against E_{in}.

3.2.2. Energy-loss spectrum (ELS)

In the energy-loss experiment scattered current is monitored as a function of the electron energy loss ΔE. This can be achieved either by keeping the voltage V_A (and thus the residual energy E_r) at a fixed value and scanning the voltage V_M (incident energy E_{in}), or vice versa. The former method is often more practical because the physics of the excitation is a function of the excess energy above the excitation threshold and the constant E_r spectra have a more uniform character across the entire energy-loss range.

A peak in the energy loss spectrum signifies that the target molecule was capable of absorbing the given amount of energy and possesses an excited state

(vibrational or electronic) at this energy. The energy loss spectrum thus probes the excited states of the neutral target molecule.

Electron energy-loss spectroscopy can be a very valuable alternative to optical spectroscopic methods, because transitions to excited states which are forbidden by electric dipole or spin selection rules may be observed by this technique. Studies utilizing this approach revealed a number of new electronic states in various molecules [75–83]. The exploitation of this feature of electron-impact spectroscopy has been reviewed, e.g., by Hudson et al. [65], Hall and Read [66], Kupperman et al. [84] and Celotta and Huebner [85].

Electron impact spectra have considerably lower resolution than is typical for optical spectra in the outer shell excitation. The highest resolution obtained with electrostatic instruments (8 meV [86]) corresponds to about 70 cm^{-1}, and that of the trochoidal electron spectrometer (25 meV) to 200 cm^{-1}. This disadvantage is compensated by the ability of electron energy-loss spectroscopy to sort out different types of transitions by recording spectra at different scattered electron energies E_r, and, when permitted by the instrument, at different scattering angles. In inner shell excitation the resolution of the electron impact experiments is, however, superior to that of the optical experiments (see for example refs. 87–89).

3.2.3. Energy-dependence spectrum (EDS)

In the energy dependence experiment the probability to excite a certain state of the neutral molecule as a function of the incident electron energy is measured. This is achieved by scanning both E_{in} and E_r simultaneously, and thus keeping ΔE fixed at the desired energy loss feature. The existence of a temporary negative ion state often causes an increase or variation of the excitation probability and the energy dependence spectrum thus bears information about the electronic states of the negative ion. The two important subclasses of this experiment are the energy dependence of vibrational and of electronic excitation. The former is extremely useful for the detection of very broad shape resonances because the cross sections for nonresonant vibrational excitation are often very small and the method thus does not suffer from the background problem, inherent in ETS (see Sections 5.2.2. and 6.2.2.). Strong excitation of IR-active vibrations may, however, also be observed without the presence of a resonance. The energy-dependence of electronic excitation is often useful for detecting core-excited resonances (see Sections 5.2.3. and 6.2.3.).

3.2.4. Dissociative attachment spectrum (DAS)

In the dissociative attachment experiment a mass filter in series with the analyzer is required and is set to transmit only a certain stable fragment anion, such as O^-, H^-, Cl^-, CH_3^-, or C_2H^-. The yield of this fragment ion as a function of the incident electron energy is recorded. The kinetic energy spectrum of the negative ions is often also desirable, as it is helpful in elucidating

the dissociation mechanism (see for example ref. 90). In most instances the production of the stable fragments is only possible through the dissociation of a temporary molecular anion and this spectrum consequently reflects the electronic states of the negative ion.

3.3. Results

The ETS, EDS, and DAS experiments give information on the total, elastic and the various inelastic cross sections as a function of the incident electron energy. The three experiments are thus to a certain degree complementary, their combined outcome being a comprehensive picture of the electronic states (ground and excited) of the molecular anion. It must be pointed out, however, that structures in cross sections may also have causes other than temporary negative ions and judgment is required in their assignment. Thus structures in the total cross section may be caused by the Ramsauer–Townsend minima (see for example refs. 28, 91, 92), Wigner cusps [36, 93] and virtual states (an example in the elastic scattering in CO_2 was given by Ehrhardt et al. [94]).

The incident electron energies at which the resonances occur, that is the energies of the (ground and excited) states of the anion are called the attachment energies (AEs). The values of the AEs multiplied by -1 are the (first and higher) electron affinities (EAs). The scope of the electron impact techniques is evidently limited to the cases where the negative ion is less stable than the neutral molecule and a free electron, that is to negative EAs.

4. INSTRUMENTS

This section briefly reviews the three types of instrument most frequently used in electron–molecule collision studies. They are the electron-transmission spectrometer, the electron energy-loss spectrometer, and the dissociative attachment spectrometer. More detailed reviews have been given for example by Schulz [18], Massey and Burhop [28], Kuyatt [95] and Massey [96]. Many instruments other than those discussed here have been developed to measure some more specialized aspects of electron scattering. To mention a few examples, the trapped electron spectrometer is used to measure the integral cross sections near threshold [97], the Ramsauer-type instruments (see for example ref. 98) and the time-of-flight transmission apparatus [99] are both used for the measurements of the absolute total scattering cross sections.

The key to an experimental study of structures in electron scattering is the ability to energy analyze low energy (less than 50 eV) electrons with narrow resolution and good transmission; two mutually exclusive requirements. In general, electrons leave a hot filament with an energy spread of the order of 1 eV, and an energy analyzer (in this case often called an "electron monochromator") is thus required for the incident beam. The incident and scattered elec-

trons are energy analyzed by dispersion in either an electrostatic or magnetic field, or a combination of the two. To maximize transmitted current through an analyzer one seeks good focussing conditions at the post-dispersion exit aperture, and this is the condition which limits the number of possible geometries.

Three types of analyzers are now in wide use. Two of them are purely electrostatic, with fields of either cylindrical or spherical symmetry. The third, the trochoidal electron monochromator, uses perpendicular electrostatic and axial magnetic fields to disperse the electrons according to their forward velocities.

Experimental difficulties abound with the slow-electron devices, and in general become more serious as the energy is decreased. The slow electrons are easily deflected from their proper paths by even very weak residual magnetic fields or stray electrostatic fields. Concerning the former, good magnetic shielding is required and the use of even weakly "magnetic" materials in the vicinity of the beam must be avoided. (Fulfilling this requirement is not always trivial because some "nonmagnetic" alloys containing nickel, chrome, or iron, like many kinds of stainless steel, are notorious for becoming slightly magnetic during machining or welding.) Stray electric fields are caused mainly by surface potential variations, which may exceed 1 eV on "dirty" surfaces and persist to a lesser degree even after meticulous cleaning. To worsen the matter, the effect of these "patches" is a function of the background gas composition, and an instrument which performs well in vacuum or with inert gases may fail completely upon the introduction of certain organic vapours. Consequently, the choice of the proper material and cleaning procedure is highly relevant, and every laboratory seems to have its own recipe for success [100]. The frequently used metals include molybdenum, non-magnetic stainless steels, and copper–nickel alloys.

4.1. Electron transmission spectrometer

The most popular [21, 53] version of the ETS technique has been introduced by Sanche and Schulz [36]. The instrument uses the trochoidal monochromator of Stamatovic and Schulz [101, 102], whose capacity to generate electron beams with constant intensity with energy up to about 1 part in 10^4, and to retain it down to very low energies (≈ 30 meV) makes it superior to the electrostatic types for this application in most respects. An often used feature is the modulation technique [36], which permits direct measurement of the derivative with respect to the electron energy of the transmitted current and results in a substantial increase in sensitivity of detection of the structures in the cross section. A schematic diagram of a typical instrument is shown in Fig. 9. The trochoidal electron spectrometer (TES), developed in the course of the present work, may also be operated in the ETS mode (see Appendix), and is then nearly equivalent to the instrument in Fig. 9.

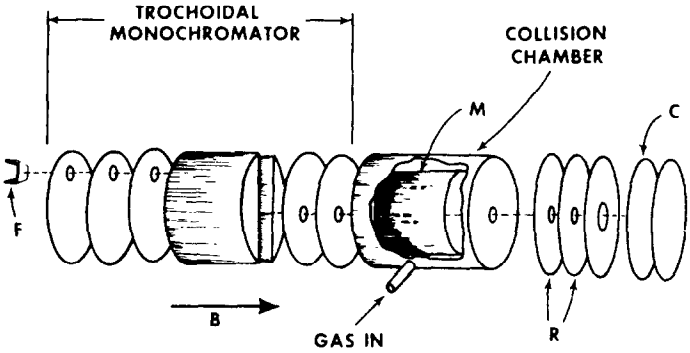

Fig. 9. Schematic diagram of an electron transmission spectrometer. Electrons emitted from the filament F are aligned by a magnetic field B and energy selected by a trochoidal monochromator. The monochromatic electron beam then passes through the collision chamber where it is attenuated by the target gas and is detected at the collector C. The retarding electrodes R may be used to provide a potential barrier to reject scattered electrons. In the derivative mode of operation a small modulating voltage is applied to the cylinder M and the a.c. component of the collected current is detected synchronously. (From ref. 38.)

In characterizing this technique it must be pointed out that its conceptual simplicity is deceptive and the actual operation of the real instrument involves many subtleties and problems, which have been analyzed and described in detail by Johnston and Burrow [74]. Most of these subtleties are concerned with the different modes of scattered electron rejection. The important practical consequences of the analysis of Johnston and Burrow [74] are that the rejection is in general far from complete and depends strongly upon the height of the retarding barrier after the collision chamber, the dimensions of the apertures of a particular instrument and the strength of the magnetic field. The differences in rejection mechanism may well produce profile alterations from one spectrometer to another. With a given instrument, one may obtain "high rejection" and "low rejection" spectra with "tight" or "open" retardation potential, which differ appreciably in the relative visibility of the different bands and the fine (vibrational) structure.

This section should perhaps be concluded with a word of caution. The above mentioned subtleties of ETS operation make the technique prone to several types of artifacts ("focussing", "retardation cusps", etc.), examples and analysis of which were also given by Johnston and Burrow [74]. These artifacts can be recognized and avoided by an experienced user and no case of a published spectrum containing them is known to the author. The application of ETS does, however, require substantial experience from the user and is in this respect perhaps more demanding than, for example, UV-photoelectron spectroscopy.

4.2. Electron energy-loss spectrometers

4.2.1. Electrostatic instruments

Electrostatic analyzers have been almost exclusively used in energy-loss spectrometers. They offer several advantages, among them the possibility of varying the scattering angle in a wide range, and the high resolution, which is typically 20–30 meV, but may reach 8 meV [86]. The use of electrostatic analyzers also brings several problems, such as high complexity of the apparatus, the necessity to continuously refocus the electrostatic lenses as the energy is varied, the difficulty of retaining the electron beam down to energies below 1 eV, and the difficulty of calibrating the "transmission function", that is the instrument's sensitivity as a function of energy, knowledge of which is required for energy-dependence spectroscopy.

Figure 10 shows a schematic diagram of the electrostatic instrument described by Boness and Schulz [103], which is representative for this type of spectrometer. A rotatable hemispherical electrostatic analyzer is used to produce a monoenergetic beam of electrons which is crossed with an effusive mo-

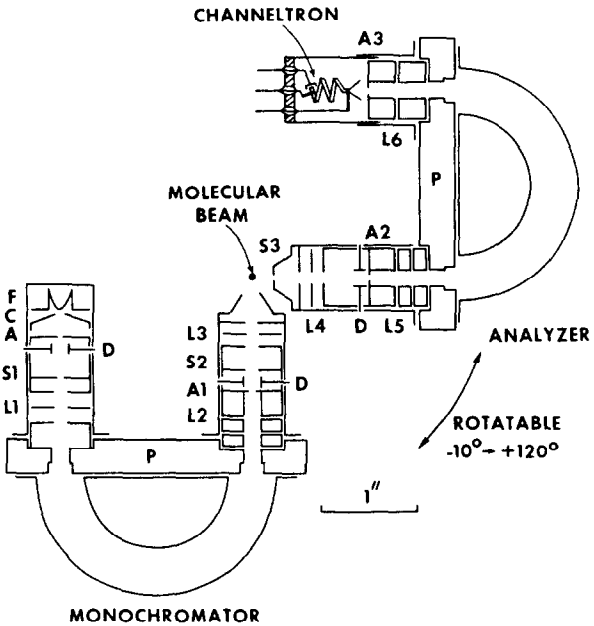

Fig. 10. Schematic diagram of the double hemispherical electron spectrometer. The electrons emitted by the filament are formed into a beam by the cathode C, anode A, and pupil defining angular stop S1. The beam is then projected by the lens L1 onto the entrance of the hemispherical deflector. The energy-dispersed beam is first projected by the lens L2 onto the resolution-defining aperture A1 and then by the lens L3 onto the molecular beam. The optical system of the analyzer is to a large degree symmetrical to that of the monochromator. D designates trajectory-correcting deflectors and P mounting plates. (From ref. 103.)

lecular beam. The energy dependence of the scattered electrons is analyzed by means of a second identical hemispherical selector. The instrument uses virtual slits of the type described by Simpson [104].

Imaging and energy control of the electron beam are performed by a number of electrostatic lenses. Accurate data for the imaging properties of a wide range of electrostatic lenses, required for the design of the electron-optical part of the spectrometer, were calculated by Harting and Read [105].

A number of instruments of this general type have been constructed in several laboratories, with particular suitability for different types of experiments. Some concentrate on high resolution and sensitivity and are primarily suitable for "spectroscopic" applications, determining the dipole-forbidden transitions in molecules. Noteworthy progress in this direction has been achieved by the group of Comer [106] through the employment of a position-sensitive detector, resulting in a major increase in sensitivity, which also indirectly permitted operation with higher resolution.

One of the most difficult tasks in the development of electron spectrometers remains sustaining the electron beams down to very low energies and controlling the instrument's transmission function, required for recording the energy dependence of vibrational and electronic excitation, particularly in the fundamentally important energy regions near threshold. This goal has only been achieved by a few instruments (see for example refs. 107–110).

4.2.2. Trochoidal electron spectrometer

This section briefly characterizes the properties of this instrument; the technical details are described in the Appendix. It has been briefly described previously [24, 111] and is shown schematically in Fig. 11. It uses trochoidal analyzers both to prepare a beam of monoenergetic electrons and to analyze the energies of the scattered electrons. The use of trochoidal motion of electrons in an axial magnetic and perpendicular electrostatic fields for energy dispersion was first reported by Stamatovic and Schulz [101, 102]. The trochoidal analyzer has subsequently often been used to prepare monoenergetic electron beams for transmission and dissociative attachment studies [18]. Several attempts had been made to implement the trochoidal monochromator in an energy-loss spectrometer [112], but severe background problems and insufficient resolution prevented broader use. These deficiences have been largely overcome in the present instrument. Its crucial feature is the use of two analyzers in series. This arrangement permits the attenuation of the intense unscattered electron beam which also enters the analyzer in the magnetically colimated instruments with their linear geometry, and caused a large background of stray electrons in the first version of the instrument which used only a single analyzer stage.

The instrument measures a superposition of 0° and 180° cross sections, because the backward scattered electrons are efficiently reflected on the po-

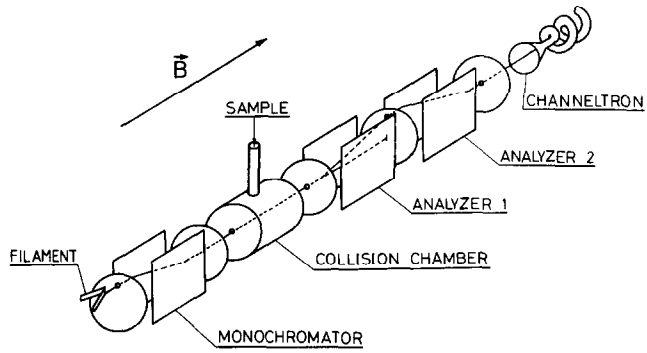

Fig. 11. Schematic diagram of the trochoidal electron spectrometer. The electrons are collimated by the axial magnetic field B. They are dispersed with respect to their forward velocities by the combination of the axial magnetic and perpendicular electrostatic fields and enter the collision chamber. The forward and backward scattered electrons (the latter after a reflection on the potential barrier at the monochromator exit) enter the analyzer, together with the unscattered beam. The first analyzer is operated at low resolution and essentially separates the scattered and unscattered beams, the second analyzer operates at higher resolution. In the transmission mode of operation all electrodes of the analyzer are connected together and serve as collector for the transmitted beam. (From ref. 24.)

tential barrier near the monochromator exit, traverse the target chamber a second time, and also enter the analyzer and are detected. Several advantages and drawbacks of the present instrument in comparison with an electrostatic apparatus may be recognized. Among the drawbacks is the inability to vary the scattering angle. The resolution of the instrument, about 35 meV, suffices to resolve the vibrational structure in most cases, but is less than the best obtained with electrostatic instruments. These drawbacks are however outweighed by several advantages for many applications. Most important is the high sensitivity, which appears to surpass that of the electrostatic instruments by several orders of magnitude. Second is the low energy capability; both the incident and the scattered electron energies may be varied down to 30 meV. The energy dependence spectra are relatively easy to correct for the instrumental transmission function. In addition there are some practical advantages like low sample consumption and the capability of the instrument to record both the transmission and the energy-loss spectra.

4.3. Dissociative attachment spectrometer

Valuable early work has been done with low resolution using essentially conventional mass spectrometers [113]. Most modern instruments incorporate the trochoidal electron monochromator, because of its capability of sustaining an intense electron beam down to very low energies (<30 meV). Both prop-

erties are essential, because many dissociative attachment processes occur near zero energy and the often very small cross sections cause sensitivity problems.

The importance of analyzing the kinetic energies of the fragment ions was recognized early by Chantry [114], who incorporated a low resolution Wien filter in the ion path of his instrument, but ion energy filters have later been incorporated in only a few instruments because of the loss of intensity they cause. An example of a typical instrument utilizing a trochoidal electron monochromator in the incident electron beam, no ion-energy analyzer, and a quadrupole mass filter is shown in Fig. 12. It must be borne in mind that even the instruments without an ion-energy analyzer often show a pronounced sensitivity peak for zero-energy ions, and therefore also some inherent ion-energy selectivity.

The instrument developed in Fribourg [25, 115], and shown schematically in Fig. 13, incorporates a high resolution cylindrical electrostatic analyzer in the ion path.

The most complete control of the experimental parameters is permitted by the instrument described by Schermann et al. [116] and Le Coat et al. [117], which consists essentially of an electrostatic energy loss instrument similar to that described in the previous section, modified by adding a miniature quad-

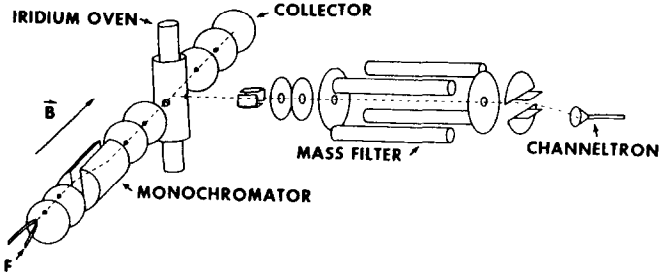

Fig. 12. Diagram of a typical dissociative attachment spectrometer. (From ref. 120.)

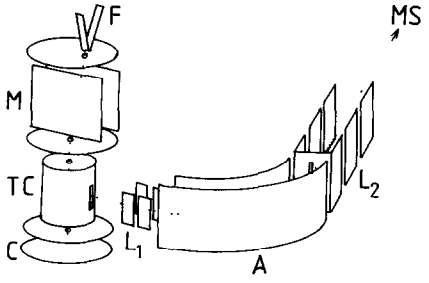

Fig. 13. Diagram of the dissociative attachment spectrometer constructed in Fribourg and used in the course of this work [25]. F is the filament, M monochromator, TC target chamber, C beam collector, L_1 and L_2 ion lenses, A ion energy analyzer, and MS mass spectrometer.

rupole mass filter in front of the detector. In this manner both the ion kinetic energy and the scattering angle are controlled, for the price of some loss in sensitivity and low energy capacity.

Certain instruments use time-of-flight mass filters for both mass and ion-energy analysis [118, 119].

5. NITROGEN

5.1. Electronic structure of neutral N_2

Electron energy loss spectra in N_2 in the electronic excitation region have been reported by Vichon et al. [77], Wilden et al. [79], Lassettre et al. [121, 122] and Mazeau [123]. This list is not complete and references to further work are given in the above references. The present section does not review the published results in detail, but presents spectra covering a wide range of energy losses and residual energies, with the aim of illustrating the behaviour of different types of transitions as a function of the energy above excitation threshold, when recorded with the trochoidal electron spectrometer. It is shown that the unique combination of 0° and 180° scattering enables this instrument to detect and distinguish the dipole and/or spin forbidden transitions despite the lack of the capacity to vary the scattering angle.

Figures 14–16 show global valence excitation spectra. Even at the very low residual energy, (E_r=0.07 eV) the $^2\Pi_g$ ground state of N_2^- (prominent in the transmission spectrum, Fig. 21) affects the energy loss spectrum by weakly exciting high vibrational levels (v=6–12) of the $X^1\Sigma_g^+$ electronic ground state of the neutral N_2. The vibrational excitation will be treated in more detail in Section 5.2.2. The resonant vibrational excitation is very weak near threshold, more than two orders of magnitude less than the strongest electronic excitation. This is in contrast to the behaviour found in many polyatomic molecules, where intense peaks in threshold spectra are caused by the "unspecific" vibrational excitation mechanism, described in more detail in Section 15.

The electronic excitation at threshold is dominated by triplet states, with the exception of the dipole-forbidden singlet–singlet transition to the $a''\,^1\Sigma_g^+$ Rydberg state. The most intense signal arises from both the dipole- and spin-forbidden transition to the lowest Rydberg state $E^3\Sigma_g^+$. The triangle-shaped continuum signal at 9–10 eV is caused by the 0.07 eV electrons arising from the autodetachment of N^-, which is formed by the dissociative attachment to N_2, and was first observed by Spence and Burrow [124] and Mazeau et al. [125]. It will be discussed in more detail in Section 5.2.4.

Substantial changes in the spectrum result from increasing the residual energy by only 80 meV, to 0.15 eV. The 0.07 eV electrons from the decay of the

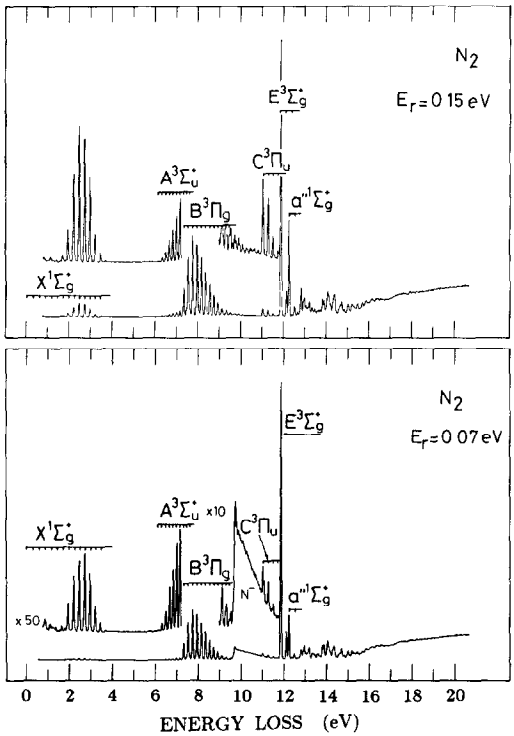

Fig. 14. Electron energy-loss spectra of nitrogen, recorded with the trochoidal electron spectrometer at the residual energies indicated. The spectra are dominated by singlet–triplet transitions at these low residual energies.

quasidiscrete N^- state no longer pass the analyzer. The relative intensity of the $E^3\Sigma_g^+$ state has dropped; that of the resonant vibrational excitation has increased.

At the next higher residual energy, 1 eV, the vibrational excitation dominates the spectrum, being about an order of magnitude more intense than the electronic excitation. Its centre has simultaneously moved to the left, because at higher E_r the fixed incident energy of the $^2\Pi_g$ resonance is reached at a lower ΔE. The excitation of the valence states is still dominated by the singlet–triplet transitions; the relative intensities of the different transitions have, however, changed.

At $E_r = 4$ eV low vibrational levels are still excited via the high energy tail of the $^2\Pi_g$ resonance. Interestingly, very high vibrational levels are excited in the $\Delta E = 4$–6 eV region with $E_r = 4$ eV and $E_r = 5$ eV. This excitation, studied in detail by Huetz et al. [61], is caused by the $^2\Pi_u$, $(\pi_u)^{-1}$ $(\pi_g^*)^2$ core excited resonance at ≈ 9 eV, which, besides decaying into its parent state ($A^3\Sigma_u$), also weakly decays into high vibrational levels of the electronic ground state. In the region of the electronic excitation the intensities of the triplet states continue

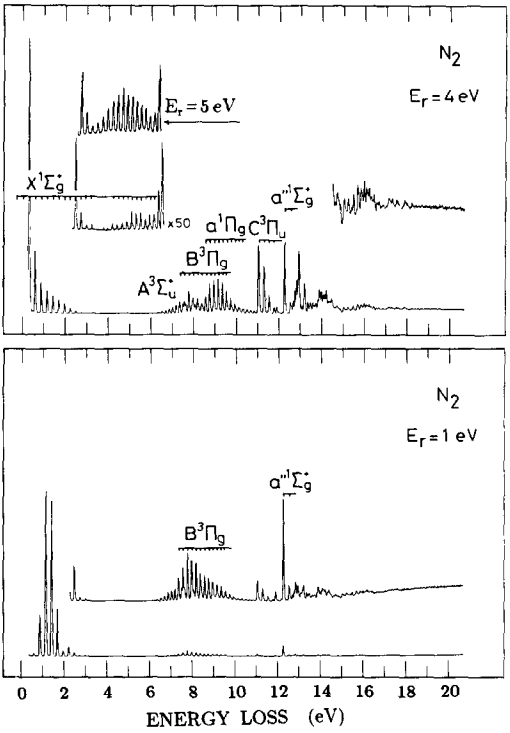

Fig. 15. Continuation of Fig. 14 at higher residual energies. The singlet-triplet transitions still dominate the spectra, and their relative intensities depend upon E_r. In addition, two spin allowed but dipole-forbidden transitions to the $a\,^1\Pi_g$ and the $a''\,^1\Sigma_g^+$ states now appear clearly.

to change, and additionally the dipole-forbidden transition to the $a\,^1\Pi_g$ state becomes prominent. The spectrum at $E_r = 5$ eV confirms the resonant nature of the excitation of the high vibrational levels, since the maximum of the excitation moves to lower vibrational levels on the energy loss scale as the residual energy is increased.

At $E_r = 16$ eV the spin-forbidden transitions have become very weak, and the dipole-forbidden singlet–singlet transition to the $a\,^1\Pi_g$ state dominates the energy-loss region below 12 eV. At higher energies the dipole allowed transitions dominate.

Finally, at $E_r = 64$ eV even the dipole-forbidden singlet–singlet transition to the $a\,^1\Pi_g$ state becomes weak and the spectrum closely resembles the VUV-absorption spectrum.

The spectra in Figs. 14–16 thus show how different transitions may be selectively enhanced by varying the residual energy. They also illustrate the role of resonant enhancements, and how they may be identified by their shift to lower ΔE as E_r is increased.

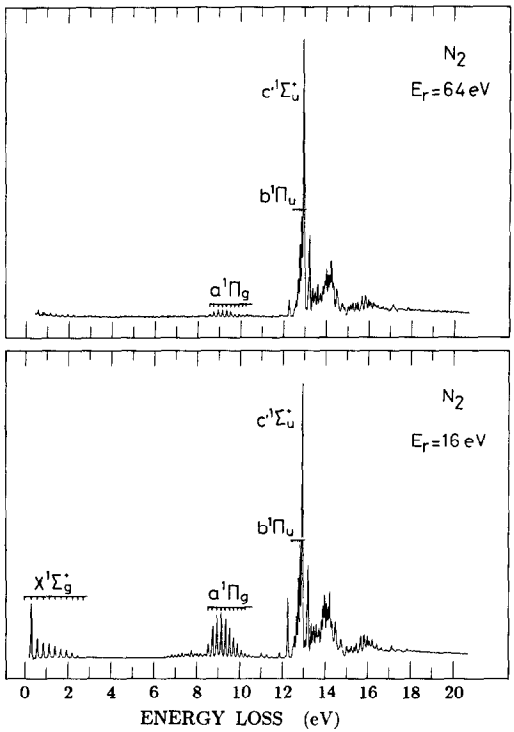

Fig. 16. Continuation of Figs. 14 and 15. The singlet-triplet transitions strongly diminish in intensity and become virtually invisible at $E_r = 64$ eV. The dipole-forbidden transition into the $a\,^1\Pi_g$ state dominates in the valence region below 11 eV. The spectrum at $E_r = 64$ eV is dominated by dipole-allowed transitions.

The remaining three figures of this section (Figs. 17–19) give examples of spectra recorded at higher resolution. The apparent width at half maximum of the $E^3\Sigma_g^+$ peak is 35 meV in Fig. 18 and 30 meV in Fig. 19. Several energy-loss spectra of N_2 in this energy range have been reported previously. Geiger and Schröder [127] recorded a very high resolution spectrum at 25 keV incident energy, which shows the dipole-allowed transitions. Several spectra at different incident electron energies were given by Lassettre [128]. Joyez et al. [129] reported a spectrum with $E_{in} = 14.3$ eV and a threshold spectrum with a resolution of 30 meV. They were able to identify the $F\,^3\Pi_u\,\{N_2^+\,\tilde{A}\,(3s\sigma_g)\}$ and $G^3\Pi_u$ $\{N_2^+\,\tilde{X}(3p\pi_u)\}$ states, predicted earlier by Leoni and Dressler [130]. The threshold spectra interpretation, requiring the disentanglement of overlapping bands, was facilitated by the calculation of the $b\,^1\Pi_u$ intensities by Dressler and Leoni [131]. Chutjian et al. [132] obtained the absolute differential and integral cross sections for a number of transitions in this energy range at incident energies of 40 and 60 eV and discussed the properties of the generalized oscillator strengths as a function of momentum transfer. They also reported two

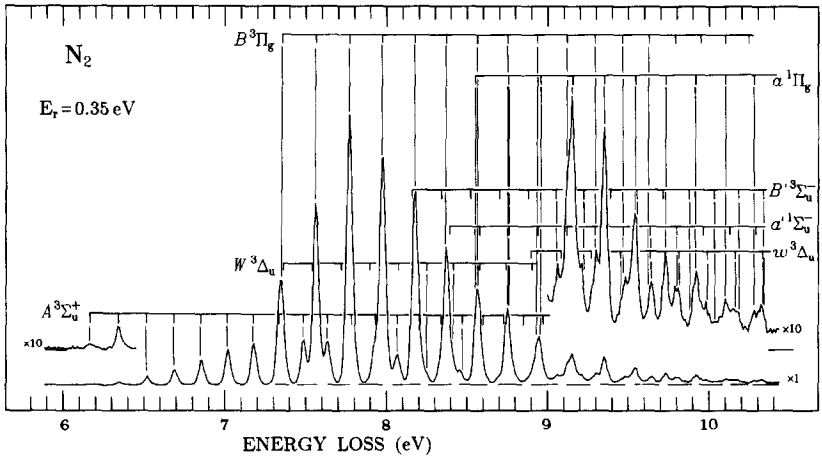

Fig. 17. Electron energy-loss spectrum of N_2, recorded 0.35 eV above threshold and showing the valence region below the lowest Rydberg transition. The energies of the vibronic states indicated above the spectrum were calculated from the constants given by Loftus and Krupenie [126].

new unidentified "triplet like" states at 13.155 and 13.395 eV. Wilden et al. [79] reported high resolution spectra in the 6.5–11 and 14–26 eV ranges.

Figure 17 shows the energy-loss region below the lowest Rydberg state. It illustrates the number of valence excited states which may be detected at this low residual energy.

Figure 18 shows the 11.7–16.7 energy-loss range, recorded at three representative residual energies. The N_2 spectrum in this region is very complex and a brief review of the known Rydberg states has been given recently by Sharpe and Johnson [133]. At $E_r = 20$ eV the dipole allowed transitions dominate the spectrum. The most interesting feature of these transitions is the extensive interaction of several states in the $^1\Sigma_u^+$ and the $^1\Pi_u$ manifolds, which has recently been understood in detail theoretically by Stahel et al. [134]. The interactions were shown to result in dramatic irregularities in both spacings and band intensities, making the interpretation of this spectral region virtually impossible without an extensive theoretical support.

At residual energies of 0.5 and 0.1 eV a number of new bands appear. The F and G triplet states originally reported by Joyez et al. [129] may be discerned as well as the 13.4 eV unidentified triplet-like state originally reported by Chutjian et al. [132]. In addition, a number of other bands appear, whose increasing relative intensity with decreasing residual energy points to dipole-forbidden, presumably singlet–triplet, transitions. The more prominent of these bands are marked by vertical unlabelled lines above the $E_r = 0.1$ eV spectrum in Fig. 18. Some of them are tentatively grouped into two progressions, one of them having a band profile reminescent of the Franck–Condon profile of the $\tilde{A}$ state, the other the $\tilde{X}$ state of N_2^+. A number of the peaks in the $E_r = 0.1$ eV

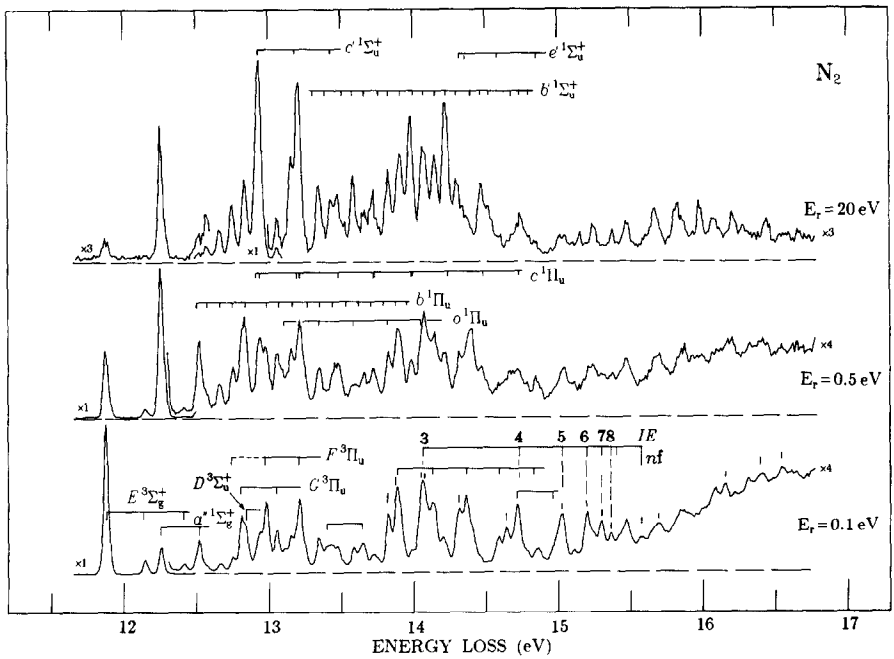

Fig. 18. Energy-loss spectra of N_2 in the 11.6–16.7 eV region at three representative residual energies. The assignments of the dipole allowed transitions are taken from ref. 134. These transitions are characterized by extensive valence-Rydberg mixing. The assignment of the *F* and *G* triplet states is from ref. 129. A number of bands appearing only in the near-threshold spectrum coincide in energy with the non-penetrating *nf* states reported in ref. 135. Several unidentified (presumably singlet-triplet) transitions observed in the $E_r = 0.1$ eV spectrum are marked by short unlabelled vertical lines.

spectrum, labelled by the numbers $n = 5, \ldots, 9$ in Fig. 18, have the energies $(\mathrm{IE} - \mathrm{Ryd}/n^2)$ with $\mathrm{IE} = 15.581$; that is they fit the Rydberg formula with $\delta = 0$. They could thus correspond to the non-penetrating *nf* Rydberg states which have been observed in absorption by Chang and Yoshino [135]. Many triplet Rydberg states converging to both the $\tilde{X}$ and $\tilde{A}$ cationic states are expected in this energy region [136–138] and a funded assignment of all observed peaks from the present (in comparison with optical spectroscopies) low-resolution spectra does not appear possible.

Figure 19 shows a detail of the 11.5–14.1 eV region recorded at threshold.

5.2. Study of the negative ion

Nitrogen is one of the most studied molecules and the published work has been reviewed for example by Schulz [18] and Trajmar et al. [139]. The present section presents an overview of the main results brought by the three basic experiments ETS, EDS, and DAS.

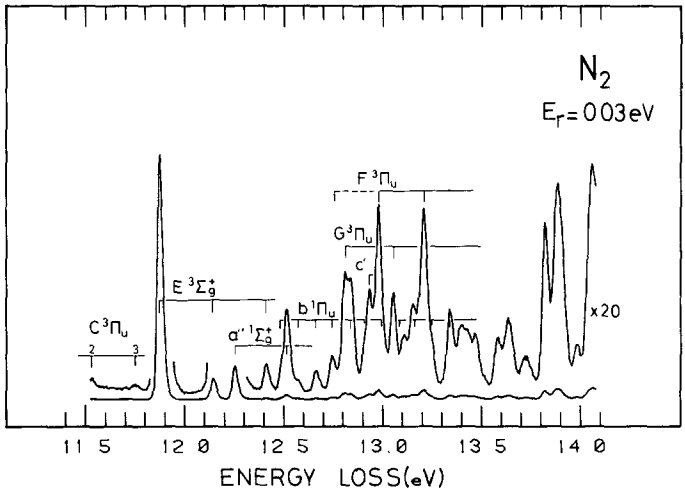

Fig. 19. Threshold energy-loss spectrum in the 11.5–14 eV region. The apparent width of the $E^3\Sigma_g^+$ peak, indicative of the resolution of the trochoidal electron spectrometer, is 30 meV.

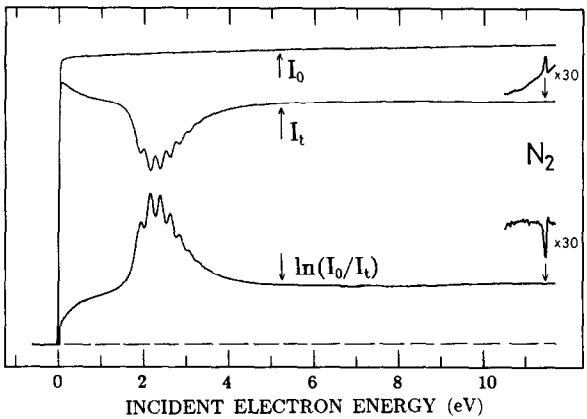

Fig. 20. Illustration of the transmission experiment in N_2. The top curve shows the incident electron current, below it is the current transmitted through a chamber filled with 10^{-2} mbar N_2. The bottom curve is an approximation (because of the incomplete rejection of the scattered electrons) of the total scattering cross section. The structured cross section rise in the 2–3 eV region is due to the $^2\Pi_g$ first shape resonance (electron capture into π^* orbital), and the narrow drop ("window resonance") at 11.48 eV to the $^2\Sigma_g$ Feshbach resonance (two electrons in a 3*s* Rydberg orbital around the $^2\Sigma_g^+$ N_2^+ core).

5.2.1. Electron transmission

Figure 20 shows the individual stages in recording the electron transmission spectrum. The top curve shows the current collected behind the collision chamber without sample gas, which is identical to the incident current I_0. (Caution must be exercised in determining the incident current because the

filament emissivity is often influenced by the background pressure of the sample gas in the main vacuum chamber.) The second curve shows the transmitted current I_t, collected with about 10^{-2} mbar of N_2 in the target chamber. If the rejection of the scattered current were complete, the total scattering cross section could be calculated according to

$$\sigma_t = N^{-1}L^{-1}\ln(I_0/I_t)$$

where N is the gas density and L the length of the target chamber. The curves in Fig. 20 were recorded under the "low rejection" conditions (see ref. 74) and the rejection was thus far from complete. Furthermore, the absolute sample pressure was not known. In spite of these limitations the shape of the $\ln(I_0/I_t)$ curve in Fig. 20 is highly reminiscent of the total cross section (given above 0.5 eV by Kennerly [99]) and is useful for the discussion of the electronic structure of the negative ion.

The experimental $\ln(I_0/I_t)$ curve, which could be called the "ETS-cross section", can conceptually be divided into the "direct scattering" contribution, which forms a nearly constant background in the 1–12 eV range, and the resonant contribution, which causes a strong enhancement of the cross section in the 2–3 eV region and a much weaker sharp dip at 11.48 eV. (The two contributions must of course be added coherently.) The 2.5 eV band is caused by the $^2\Pi_g$ resonance, which may be pictured as a result of a temporary capture of the incident electron into the lowest unoccupied orbital (π^*) of N_2. The dip at 11.48 eV is caused by the $^2\Sigma_g$ Feshbach resonance with the configuration $(\sigma_g)^{-1}(\sigma_g 3s)^2$. It may be pictured as an electron captured in the field of the lowest Rydberg state of N_2, $E^3\Sigma_g$, which is thus its parent state. The parent state may be found at 11.87 eV (Figs. 14 and 19), the resonance is 0.4 eV more stable than its parent state, this value being typical for a $3s^2$-type resonance [18, 140]. The grandparent concept may be introduced, in which this resonance is considered as having two electrons moving in the $3s$ orbital around its grandparent state, the $^2\Sigma_g$ ground state of N_2^+. This state is located at 15.60 eV [141]; the resonance is 4 eV below its grandparent state, this value also being in the typical range [18, 140, 142].

Figure 21 shows the transmission spectrum in its common form of presentation, as the derivative of the transmitted current, dI_t/dE, which was in the present case not obtained by the modulation technique, but calculated digitally from the corresponding curve of Fig. 20. The capability of the derivative representation to enhance the sharp variations of the I_t and suppress the nearly constant background of direct scattering are evident.

5.2.2. Energy dependence of vibrational excitation

The efficient vibrational excitation of N_2 by electron impact in the 2.3 eV region was the first observed manifestation of a resonance in electron molecule scattering [143] and the first case where the interesting "boomerang" vibra-

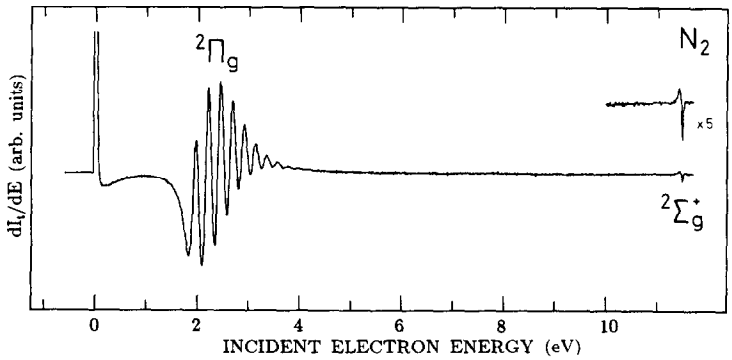

Fig. 21. The derivative representation of the ET spectrum of N_2, with enhanced visibility of the sharp structures.

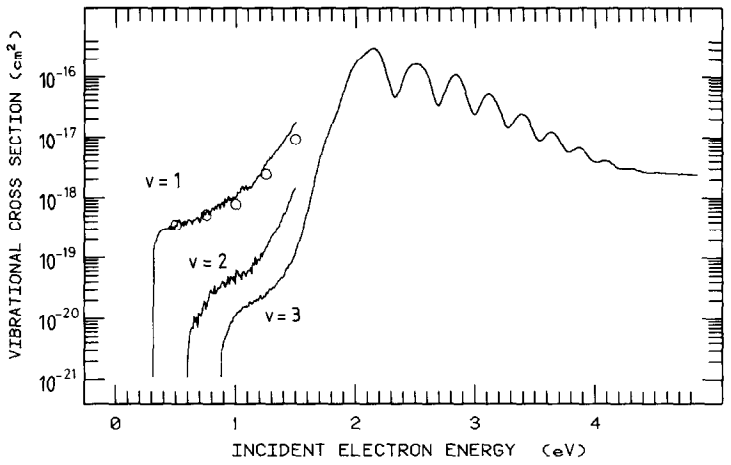

Fig. 22. Energy dependence for the $v=0\rightarrow 1$, 2 and 3 excitations shown on a semilogarithmic scale, illustrating the dramatic increase of the cross section in the resonance region. The open circles indicate the results of a swarm experiment [146, 147]. (From ref. 148.)

tional structure was observed [144] and explained [145]. The ability of the $^2\Pi_g$ resonance to excite vibrational motion has already been encountered in the energy-loss spectra of Figs. 14 and 15. It will be discussed in more detail in the section on the excitation of high vibrational levels.

Figure 22 shows, on a semilogarithmic scale, the cross section for exciting $v=3$ below and in the $^2\Pi_g$ resonance region (together with the $v=1$ and $v=2$ cross sections below the resonance region). The cross section is very small below the resonance region because the energy transfer between the heavy nuclei and the light electron is very inefficient, but rises dramatically (by about four orders of magnitude) within the resonance region. It is the small magnitude of the vibrational cross sections outside the resonance region which makes

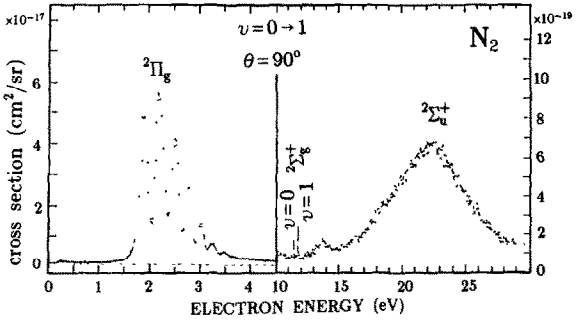

Fig. 23. Differential cross section for excitation of the $v=1$ level of the $X^1\Sigma_g^+$ ground state of N_2 at 90° in the 0–30 eV range, showing the two shape resonances at 2.3 and 22.5 eV with trapping of the electron in the $1\pi_g$ and $3\sigma_u$ unoccupied valence orbitals. The $^2\Sigma_g^+$ Feshbach resonance at 11.48 eV also causes sharp peaks in the cross section. (From ref. 149.)

this experiment a powerful method for detecting resonances, not affected by the problem of background due to direct scattering, inherent to the ETS. This property allows the observation of weak and broad resonances, which cannot be differentiated from the background in ETS. Figure 23 shows a wide range spectrum of Tronc and Malegat [149], which reveals a broad σ^* resonance.

Finally, it has been shown by Huetz et al. [61], that the $^2\Pi_u$ core excited resonance also decays into high vibrational levels of the electronic ground state, although this decay is not a one-electron process. Evidence for this decay channel has already been seen in the $E_r=4$ eV and $E_r=5$ eV spectra in Fig. 15. The $^2\Pi_u$ resonance appears very clearly in the global view of the $v=14$ excitation in Fig. 24.

5.2.3. Energy dependence of electronic excitation

Huetz et al. [61] and Mazeau et al. [150] studied the energy dependence of the $A^3\Sigma_u$ and the $B^3\Pi_g$ states in N_2, and observed the enhancement caused by the $^2\Pi_u$ core excited resonance. Two curves recorded by the trochoidal electron spectrometer are shown in Fig. 25. Both curves show resonant enhancement in the 8.5–10 eV region. The enhancement in the $A^3\Sigma_u$ excitation is probably due to the $^2\Pi_u$ resonance with the configuration $(\pi_u)^{-1}(\pi_g)^2$. This core excited resonance has an attachment cross section too small to appreciably affect the total scattering cross section, and is consequently not observed in ETS (Figs. 20 and 21). On the other hand its decay into the electronically excited states represents a sensitive means of detection. From the available spectra it does not appear possible to decide whether there are two core excited shape resonances in the 8–11 eV range, with the parent states $A^3\Sigma_u$ and the $B^2\Pi_g$, or whether there is only one resonance, decaying into both channels. The cross section for electronic excitation is appreciable even outside the $^2\Pi_u$ core excited region. This cross section could be attributed to "direct" excitation; on the

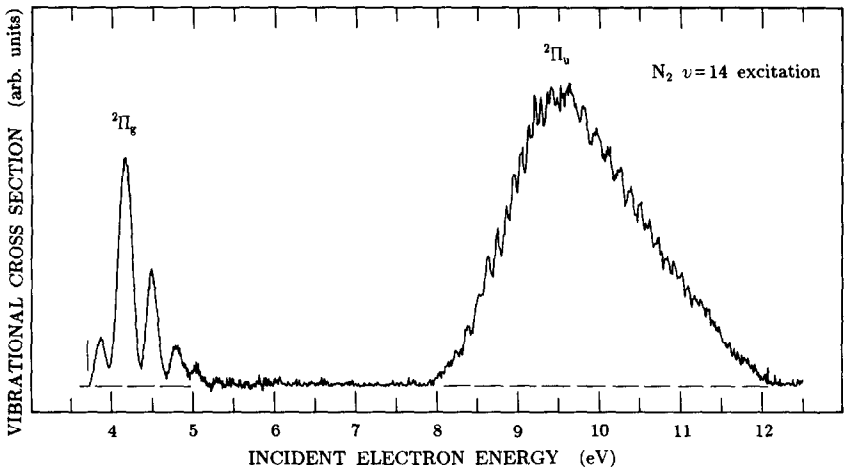

Fig. 24. Energy dependence of the excitation of the $v=14$ level of the electronic ground state in N_2, showing the high-energy tail of the $^2\Pi_g$ shape resonance and the $^2\Pi_u$ core excited resonance in the 8–12 eV range.

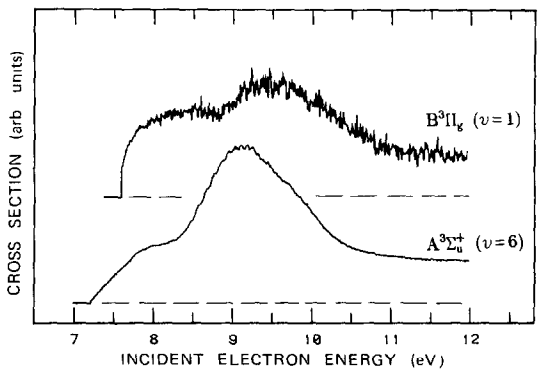

Fig. 25. Energy dependence of the excitation of the two lowest electronically excited states in N_2. Cross section enhancements due to core excited shape resonances in the 8.5–10.5 eV region can be seen. Fine structure due to vibrational motion in the intermediate anionic state is discernible on the lower curve.

other hand the theoretical work of Teillet-Billy et al. [62] and Gauyacq et al. [63] on the electronic excitation of O_2 implies that low-lying shape resonances (in N_2 the $^2\Pi_g$ resonance) may contribute significantly to electronic excitation at much higher energies.

5.2.4. Dissociative attachment

A proper dissociative attachment is not possible in N_2, because the N atom has a negative electron affinity and cannot form a stable negative ion fragment [151]. A process closely related to dissociative attachment, where N_2^- disso-

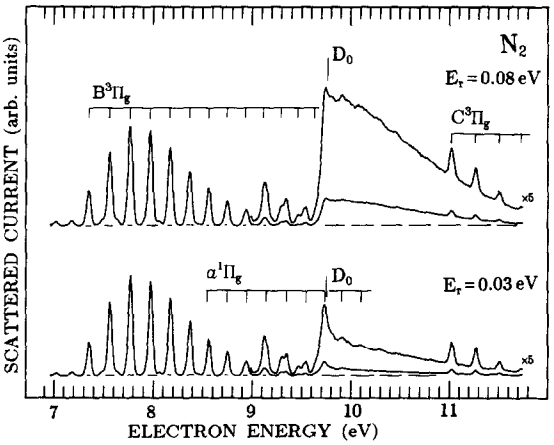

Fig. 26. Energy-loss spectra in N_2, taken with the two constant residual energies indicated. The continuous signal above 9.83 eV is due to 0.07 eV electrons resulting from autodetachment of N^- atomic ions formed through dissociation of an intermediate state of N_2^-. The intensity of the $v=6$ level of the $a^1\Pi_g$ state is anomalously enhanced at these low residual energies.

ciates into N and N^-, has, however, been observed by Spence and Burrow [124] and Mazeau et al. [125]. Since the lifetime of N^- is relatively long (autodetachment width 16 meV [125]) the detachment occurs at a relatively late stage of the dissociation, when the two nuclei are sufficiently far apart for the detached electron spectrum to be characteristic of N^- and not N_2^-. This process causes the triangle-shaped band in the $E_r = 0.07$ eV energy-loss spectrum in Fig. 14.

The pertinent energy region, recorded with the trochoidal electron spectrometer, is shown in detail in Fig. 26. These spectra confirm, with a somewhat higher resolution, the conclusion of Spence and Burrow [124] that the excitation of the $v=6$ level of the $a^1\Pi_g$ state is anomalously enhanced near threshold and thus causes a "false" threshold for the slow electrons at an energy below the dissociation energy D_0. The true threshold for the 0.07 eV electrons from N^- detachment is at $D_0 + |EA|$, 0.07 eV above D_0.

6. CARBON MONOXIDE

6.1. Electronic structure of neutral CO

Electron energy loss spectra of CO in the electronic excitation region have been reported by Mazeau et al. [152] and Wallbank et al. [153]. Hammond et al. [154] have reported threshold electron spectra covering electronic excitation.

The energy loss spectra obtained with the trochoidal electron spectrometer very near threshold and 0.5 eV above threshold are shown in Figs. 27 and 28.

The $E_r = 0.03$ eV spectrum is very similar to the threshold spectrum of Ham-

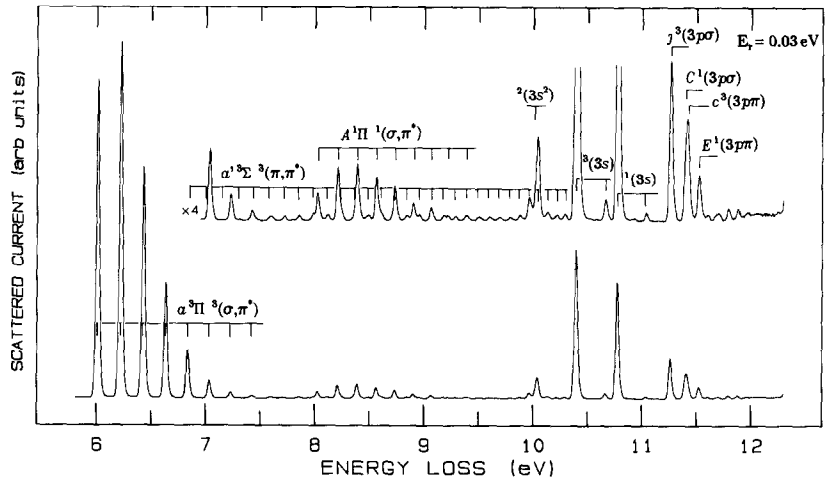

Fig. 27. Electron energy-loss spectrum of carbon monoxide, recorded with a residual energy of 0.03 eV. The excitation of the levels $v = 26$ and 27 of the $a'\,^3\Sigma$ state is strongly enhanced by the $^2(3s^2)$ resonance at 10.04 eV, whose energy is indicated above the spectrum.

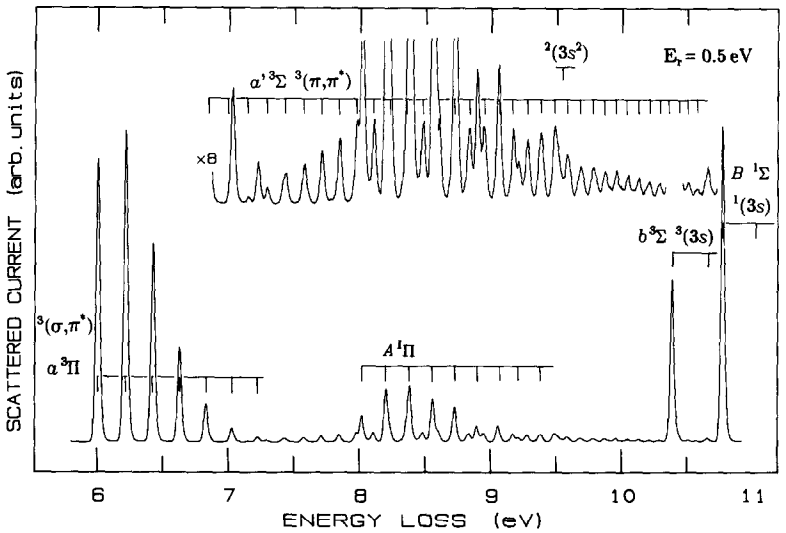

Fig. 28. Electron energy-loss spectrum of carbon monoxide, recorded with a residual energy of 0.5 eV. At the higher energy above threshold, the $^2(3s^2)$ resonance at 10.04 eV causes only a slight enhancement of the levels $v = 21$ and 22 of the $a'\,^3\Sigma$ state.

mond et al. [154]. The only significant difference is the absence of the O^- signal observed by Hammond et al. [154] around 9.6 eV, because in their electrostatic instrument both electrons and negative ions follow the same trajectories and reach the detector. The absence of the O^- signal in the present spectra confirms that ions do not reach the detector in the trochoidal electron

spectrometer and the energy-loss spectra recorded with this instrument are not affected by dissociative attachment processes.

The relative intensities of the $^3(3s)$ and $^1(3s)$ peaks have been shown by Hammond et al. [154] to be dependent on residual energy within the first ≈ 50 meV above threshold. The relative intensities of these two peaks in Fig. 27 are consistent with the spectra of Hammond et al. [154] under the assumption that the residual energy in the present spectra has been 0.03 eV, as indicated. These observations indicate that the present version of the trochoidal electron spectrometer is not capable of detecting electrons with energies lower than about 20 meV, this fact probably being caused by a small potential barrier at the exit aperture of the target chamber.

A comparison with the energy-loss spectra of N_2, shown in Figs. 14, 15 and 17 is revealing. In both molecules the $^3(\sigma,\pi^*)$, $^3(\pi,\pi^*)$, and $^1(\sigma,\pi^*)$ transitions dominate the energy-loss region below 10 eV; the order of the first two transitions is reversed in CO with respect to N_2, however, reflecting the higher energy of the highest σ orbital, revealed by photoelectron spectroscopy [155]. The lowest Rydberg states of CO are at lower energies and closer to the low-lying valence transitions in CO, reflecting the lower ionization energy of CO. The analogy suggests a possible interpretation of some of the weak bands in the 11.6–12.0 eV ("m" and "n" series of Wallbank et al. [153]) region of Fig. 27 as a $^3\Pi$ state corresponding to the $^3\Pi_u$ state of N_2.

6.2. Energy dependence of vibrational excitation

This section discusses briefly the general features of the vibrational excitation; the excitation of high vibrational levels will be discussed more specifically in Section 15.

An energy-loss spectrum showing pure vibrational excitation 0.2 eV above threshold is shown in Fig. 29. The energy dependence of the excitation of selected vibrational levels is shown on a semilogarithmic scale in Fig. 30. Comparison with the corresponding Fig. 22 for N_2 underlines the similarity of the lowest $^2\Pi$ resonances and the vibrational excitations in both molecules. The only important differences are the somewhat shallower vibrational structure in CO, reflecting the shorter resonance lifetime in this molecule, and the relatively larger $v=1$ cross section below the resonance in CO, caused by direct excitation of this IR-active transition in forward scattering.

6.3. Energy dependence of electronic excitation

Resonant phenomena in electronic excitation have been reviewed by Schulz [18] and investigated by Swanson et al. [156]. High-resolution metastable excitation functions have been reported by Newman et al. [157].

Excitation functions of a number of electronic transitions obtained with the

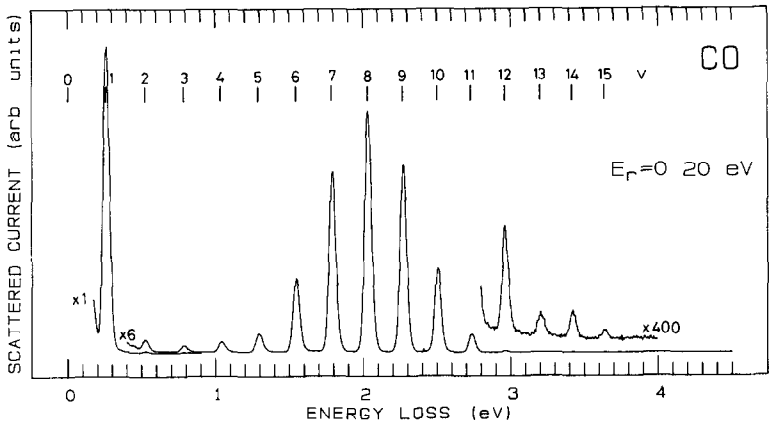

Fig. 29. Energy-loss spectrum of carbon monoxide in the region of pure vibrational excitation.

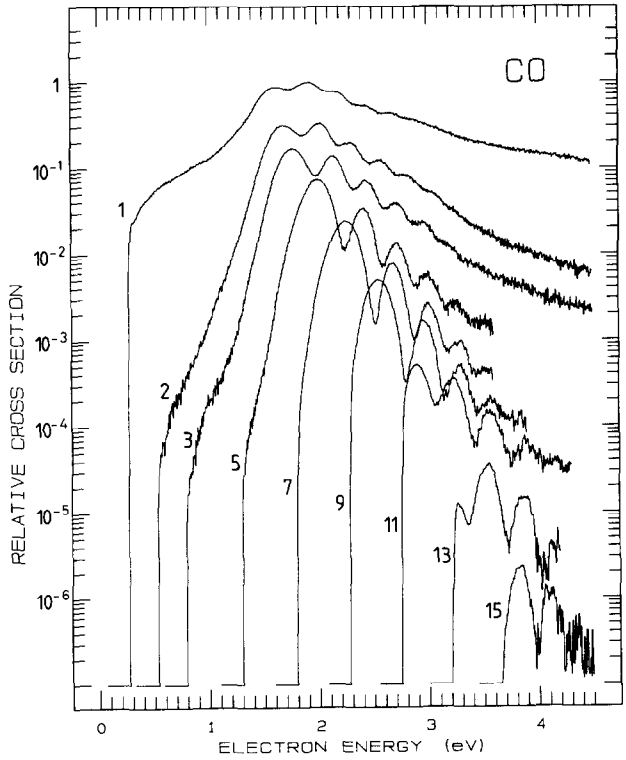

Fig. 30. Energy dependence of the excitation of selected vibrational levels in CO, shown on a semilogarithmic scale.

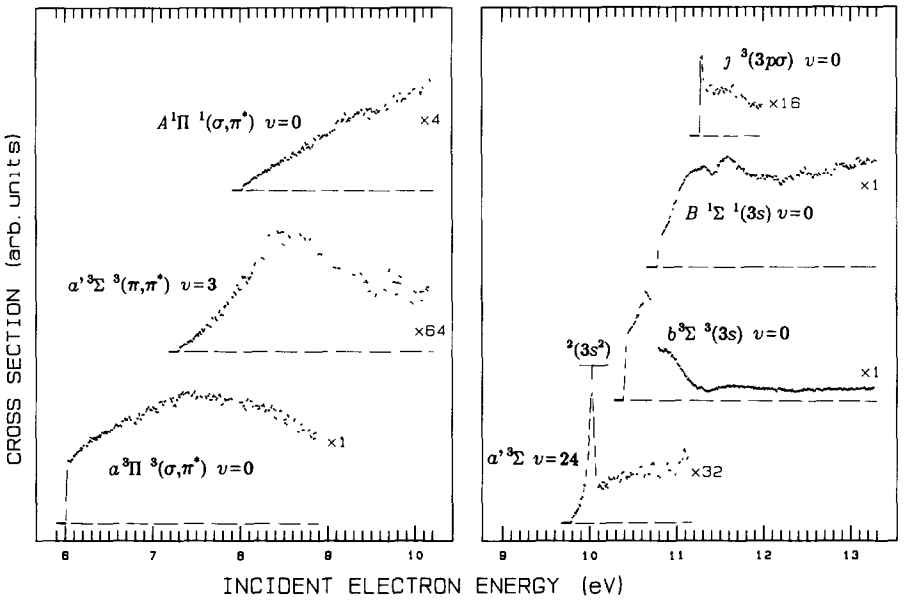

Fig. 31. Cross sections for the excitation of several valence and Rydberg excited states in carbon monoxide. All curves are shown on the same vertical scale, expanded vertically as indicated by the multiplication factors for clarity. The sharp peak in the excitation of the $v=24$ level of the $a'\,^3\Sigma$ state is caused by the $^2(s^2)$ resonance (see also Figs. 27 and 28).

present instrument are presented in Fig. 31. Like all data obtained from the trochoidal electron spectrometer, the spectra are a superposition of 0° and 180° differential cross sections and their shapes may consequently differ from the shapes of the integral cross sections if the angular distributions vary with energy. Meaningful comparison should nevertheless be possible with the recent calculations of Huo et al. [158], who obtained both the integral cross sections and the angular distributions.

The present spectra exhibit a clear threshold peak only in the excitation of the $j^3(3p\sigma)$ state. This is at variance with the observation of Swanson et al. [156], who report threshold peaks in their 45° differential cross sections for many electronic states, in particular the $a^3\Pi$ lowest valence state. The difference could be caused by the different angle of observation; a more probable explanation involves an instrumental effect, an increased sensitivity of the instrument of Swanson et al. [156] for low energy electrons. In the experimental section of their paper Swanson et al. [156] report that they applied a small accelerating voltage to the scattered electrons, which increases the acceptance angle, and consequently the collection efficiency, for low-energy electrons. The excitation functions have not been corrected for this effect and Swanson et al. [156] conclude that, "this increase in collection efficiency ... may be responsible for the threshold peaks". The transmission function of the

present instrument has been calibrated and the spectra corrected accordingly (see Appendix); the shapes of the present cross sections are therefore more reliable. When a "correction function", diminishing the intensity near threshold, is applied visually to the cross sections of Swanson et al. [156], a qualitative agreement with the present cross sections is obtained for all states, suggesting that the shape of the cross sections is similar for both angles of observation.

The correctness of the shapes of the present cross sections, in particular for the $a^3\Pi$ state, is further confirmed by comparison with the metastable excitation function of Newman et al. [157]. The above mentioned problem of energy-dependent collection efficiency is inherently much less severe in the metastable detection experiment. In the 6–8 eV range, the metastable excitation function is essentially equal to the integral cross section for the excitation of the $a^3\Pi$ state summed over all final vibrational states (the cross section for the $a'^3\Sigma$ state being much smaller). The experimental cross section of Newman et al. [157] in this energy region consists of a series of steps corresponding to the individual final vibrational levels, indicating that the cross section for each vibrational level is essentially a step function, without a threshold peak. This result confirms the step-like shape of the present cross section for the $v=0$ level, shown in Fig. 31, and also suggests that the shape of the cross section does not dramatically depend on angle.

The present excitation function for the $b^3\Sigma$ state is very similar to the cross section obtained by Mazeau et al. [159] (reviewed in ref. 18) at 40°.

7. BENZENE

7.1. Electronic structure of neutral benzene

The extensive literature on the spectroscopy of benzene, including earlier electron energy-loss work, has been reviewed by Ziegler and Hudson [68]. This section reviews and extends the published [24] results obtained with the trochoidal electron spectrometer.

Figure 32 shows an example of a wide-range spectrum, recorded at a very low residual energy, $E_r=0.15$ eV. The general features show similarity with the previous example N_2. In the 1–2 eV range pure vibrational excitation is caused by the $^2E_{2u}$ state of benzene anion, which will be further discussed in connection with ETS in Section 7.2.1. Note that the unspecific vibrational excitation mechanism, discussed in more detail in Section 15, causes the vibrational to be more intense relative to the electronic excitation than in the near-threshold spectra of N_2 (Fig. 14). The resonant nature of this excitation is revealed in the energy-loss experiment by the shift of this band to the left on the energy-loss scale with increasing E_r. Many valence and Rydberg transitions are observed in the 3–9 eV range.

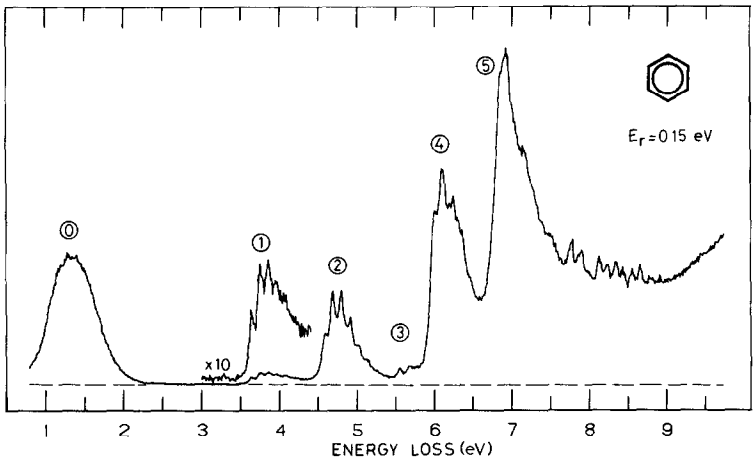

Fig. 32. Global energy-loss spectrum of benzene. The region 0 contains pure vibrational excitation, enhanced by the lowest shape resonance $^2E_{2u}$ in the 1-2 eV range of incident energies. At this low residual energy mostly singlet-triplet excitations appear in the predominantly valence regions 1-5. Rydberg transitions cause the structure above region 5.

The valence region is shown for several residual energies in Fig. 33. At low residual energies the spectrum is dominated by the three lowest singlet–triplet transitions. The relative intensities of the individual transitions are a function of the residual energy, and can be understood in terms of the decay of core excited shape resonances (Section 7.2.3.). The present spectra, recorded with $E_r = 0$–2 eV and with the scattering angles fixed at 0° and 180° are very similar to the spectra obtained previously at intermediate (10 eV) residual energies and large scattering angles in both gaseous [160] and solid [161] phases, illustrating that variable scattering angle need not be essential for the observation of the triplet states. At $E_r = 20$ eV the relative intensity of the triplet states has dropped dramatically and the spectrum is nearly identical to an optical absorption spectrum such as given by Bolovinos et al. [162] and Philis et al. [163], both in relative intensities of the electronic transitions and the envelopes of the individual bands. In particular the origin of the first singlet–singlet band $^1B_{1u}$ is not seen and only the optically-active vibronic transitions are observed. Whether the dipole-forbidden origin of this band is excited at low E_r cannot be tested, because the region is obscured by the $^3E_{1u}$ triplet band. The dipole-forbidden origin has been observed, however, by Klump and Lassettre [72], with high incident electron energy (300 eV), where the obscuring triplet state is no longer excited, and with nonzero momentum transfer ($\theta = 6.5°$, $K = 1.0$ Å^{-1}), where the transition is no longer forbidden. At intermediate energies the singlet and the triplet bands overlap.

The region 4 of the spectrum, $\Delta E = 6$–6.5 eV, is particularly challenging as it contains several overlapping transitions and is not yet fully understood. Fig-

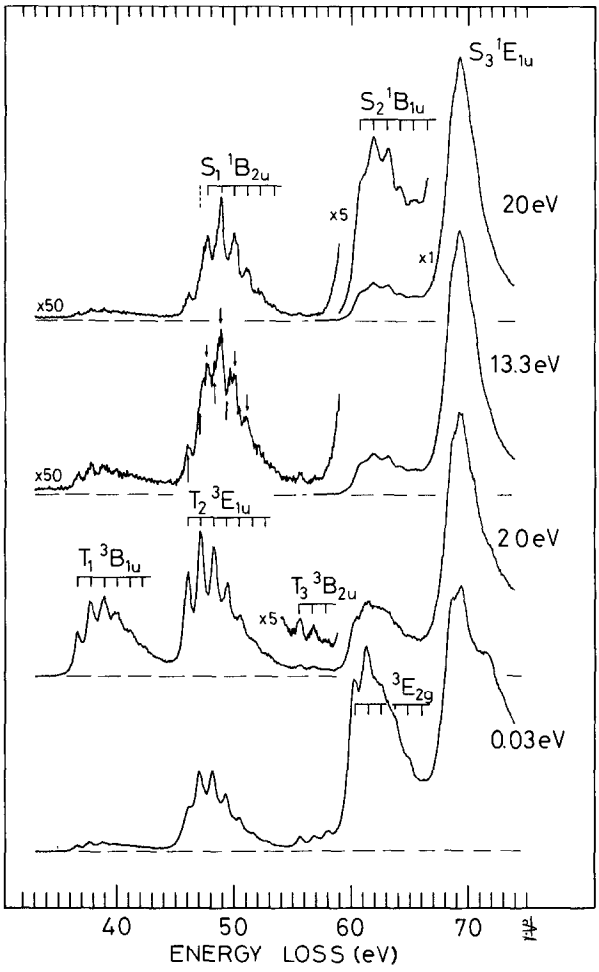

Fig. 33. Energy-loss spectra in the valence region of benzene. With $E_r = 20$ eV the spectrum is dominated by the optically-allowed transitions, and with $E_r = 0.03$ and 2.0 eV by the spin-forbidden transitions. At intermediate energies both kinds of transition overlap.

ure 34 shows the spectra of C_6H_6 and C_6D_6, recorded in this region with several residual energies. The dipole-allowed transition to the $^1B_{1u}$ state dominates this spectral region at high residual energy. A different band is observed at low E_r and has been assigned to the $^3E_{2g}$ state by Wilden and Comer [160]. The two narrow peaks at 6.33 eV (also observed by Wilden and Comer [160]) and 6.28 eV (first observed with the trochoidal spectrometer) at $E_r = 0.5$–0.7 eV were assigned to the lowest (3s) Rydberg transitions $^3E_{1g}$ and $^1E_{1g}$. Detailed comparison of the spectra of C_6H_6 and C_6D_6 is made in Fig. 35, where the magnitude of the isotope shift may be determined. The observed isotope shifts

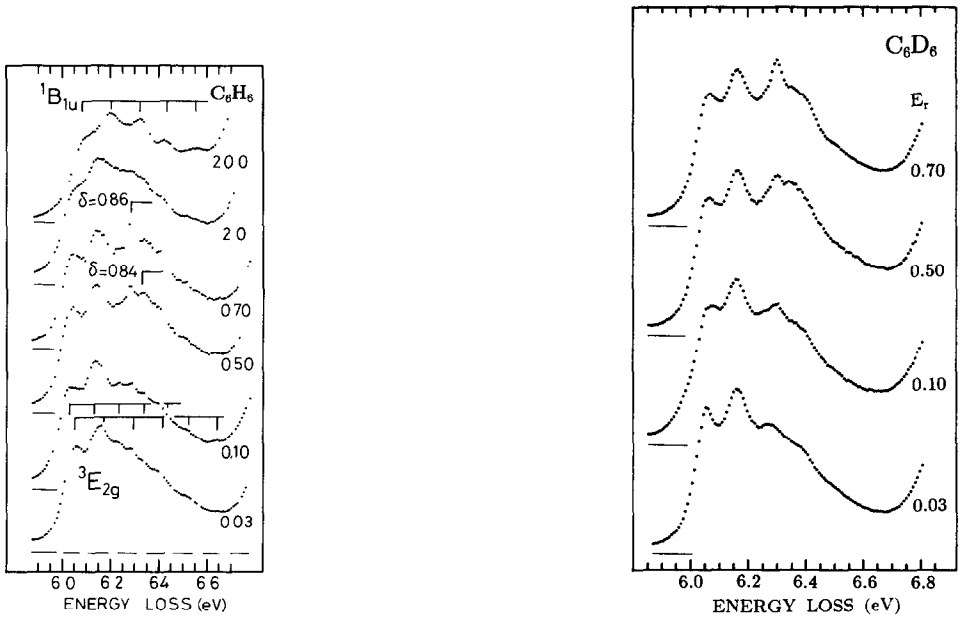

Fig. 34. Energy loss spectra in the 6-6.5 eV region in benzene (left) and hexadeuterobenzene (right). At low residual energies several overlapping bands are observed, whose relative intensities change with residual energy. The general pattern is very similar in both compounds, although some distinct fine differences in the band profiles occur, probably due to unequal isotope shifts of the individual overlapping transitions.

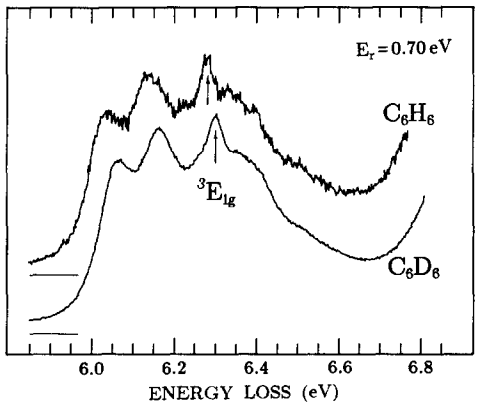

Fig. 35. Comparison of the energy-loss spectra of benzene and hexadeuterobenzene at $E_r = 0.7$ eV. The isotope shift of the sharp peak (6.28 eV in C_6H_6) is 20 ± 10 meV, consistent with its assignment to the $^3E_{1g}$ lowest Rydberg state in benzene. The isotope shift of the underlying valence transitions is slightly larger.

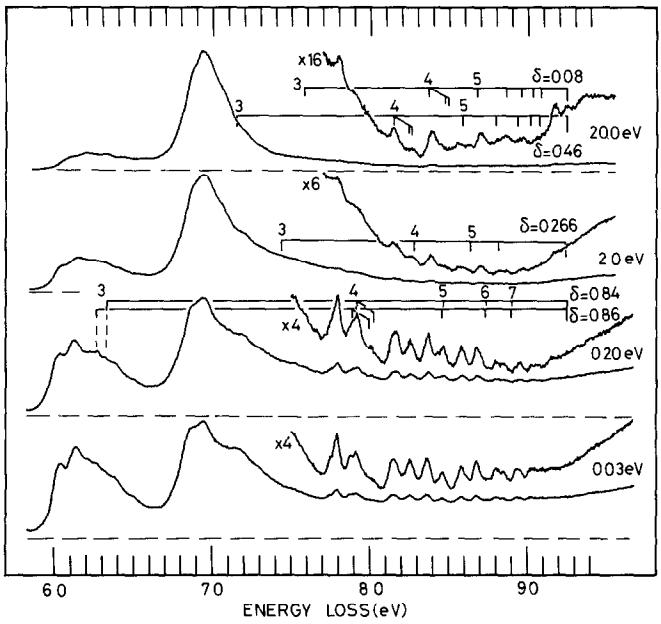

Fig. 36. Energy-loss spectra of benzene in the Rydberg region. The residual energies and true zeros are given for each curve. The vertically expanded curves have been offset vertically for clarity. Positions of the two optically allowed series ($\delta = 0.46$ and $\delta = 0.08$), as well as a quadrupole-allowed series with $\delta = 0.27$ [160] are indicated. The series with $\delta = 0.84$ and $\delta = 0.86$ are the ns-$^1E_{1g}$ [164] and ns-$^3E_{1g}$ [24] Rydberg states.

appear consistent with the above assignments. The region of Rydberg transitions is shown in detail in Fig. 36.

7.2. Benzene negative ion

Several studies on resonances in benzene have been reported and most of the pertinent references may be found in ref. 24 and throughout this section, which reviews and extends the existing data.

7.2.1. Electron transmission spectrum

Electron transmission spectra in the derivative form have been reported by Sanche and Schulz [37], Nenner and Schulz [38], and Burrow et al. [22, 165]. Mathur and Hasted [166] reported transmission spectra without the derivative feature.

Figure 37 shows the individual curves arising in the ET experiment, presented in the same format as for N_2 in Fig. 20. The "total" scattering cross section (with the same limitation as in N_2) may again be divided into the "direct" scattering contribution, which, however, varies much more with en-

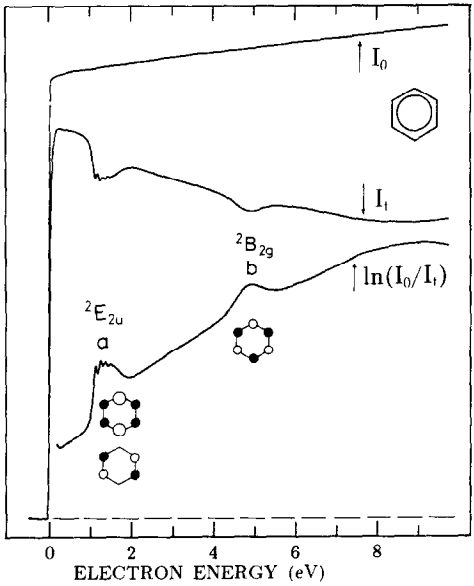

Fig. 37. The electron-transmission experiment in benzene. The curves show the incident and transmitted electron currents. The bottom curve is the approximate total scattering cross section. It consists of a "direct" scattering contribution, which is a slowly varying function of the incident energy and two superimposed narrower structures, due to shape resonances. The virtual orbitals in which the incident electron is trapped (disregarding a small admixture of core excited configurations) are also shown schematically.

ergy than was the case in N_2, and the resonant contribution. In spite of this energy-dependent background of direct scattering two clear enhancements may be discerned at 1.15 and 4.8 eV, caused by the $^2E_{2u}$ and $^2B_{2g}$ resonances. These resonances may be pictured as a temporary capture of the incident electron in the e_{2u} and b_{2g} orbitals, depicted schematically in Fig. 37. Whereas this single electron picture is probably quite correct for the first band, the decay of the $^2B_{2g}$ resonance into the triplet states (Section 7.2.3.) seems to indicate the admixture of some core excited configurations, making this state a not purely one-particle shape resonance.

The $^2E_{2u}$ band has vibrational structure, and the temporary anion must therefore have a lifetime at least comparable to the vibrational period. The $^2B_{2g}$ band is structureless, indicating a very short lifetime of this anion state.

The digitally calculated derivative of the transmitted current is shown in Fig. 38. The enhanced visibility of the resonant features in this representation is even more pronounced than in the case of N_2, and is best illustrated by the appearance of three additional bands, which were labeled *c*, *c'*, and *d*. These three features were reported previously [22, 53]. From the small intensity of these resonances in the ETS experiment, reflecting the weak effect they have

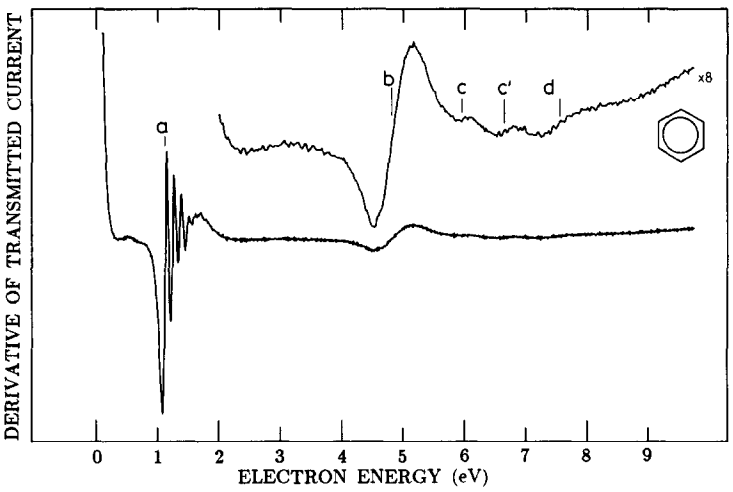

Fig. 38. The derivative representation of the ET spectrum. The enhanced visibility of weak features is demonstrated by the appearance of three additional resonances *c*, *c'*, and *d*.

on the total scattering cross section, we may conclude that the attachment cross section is small. These resonances will be seen to decay strongly into the valence excited triplet states of neutral benzene and will be assigned to core excited resonances in Section 7.2.3.

7.2.2. Energy dependence of vibrational excitation

The energy dependence of vibrational excitation in benzene has been studied previously by Azria and Schulz [167], who measured the energy dependence of the ν_1 (symm. C–H stretch) vibration in the 4–10 eV region. Wong and Schulz [168] presented the vibrational energy-loss spectra with incident energies of 1.18 and 4.8 eV without giving the energy dependencies. They assigned a number of the excited vibrations and discussed the symmetry-imposed selection rules involved in the excitation. The present trochoidal electron spectrometer permitted the recording of energy dependence spectra which are corrected for the analyzer transmission function and also include the near-threshold region.

Figure 39 shows the energy-loss spectra with residual energies chosen such that the incident energies fall into the two π^* shape resonances *a*, *b*, and the σ^* resonance *g*. The first shape resonance *a* is seen to lead to the excitation of the ν_2 ring stretch, ν_1 symm. C–H stretch, and a number of other unresolved vibrations. The higher energy resolution of an electrostatic instrument permitted Wong and Schulz [168] to identify the ν_{20}, ν_2 and $\nu_{16}+n\nu_2$ progressions. At the higher residual energies dominant $n\nu_1$ excitation is observed; with $E_r = 6.0$ eV six members of the progression may be discerned.

The energy dependence of the excitation of some overtones of these vibra-

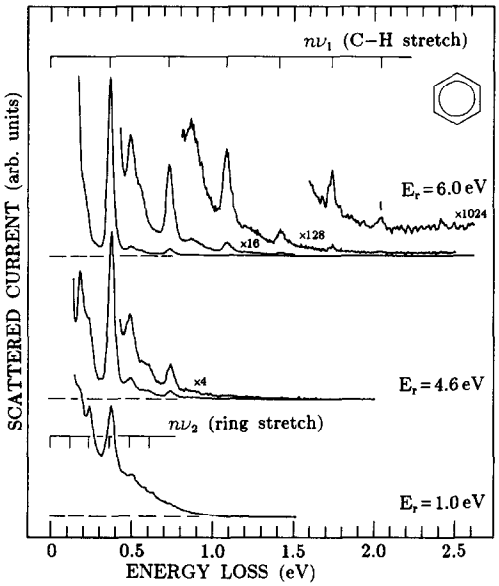

Fig. 39. Vibrational energy-loss spectra recorded with the constant residual energies indicated. The residual energies are chosen such that the incident energies fall into the shape resonances *a*, *b*, and *g*. The resonance *a* causes the excitation of ν_1, $n\nu_2$, and a number of unresolved vibrations. The resonances *b* and *g* cause excitation of long progressions in ν_1.

tions are shown in Fig. 40. In the energy region covered by both experiments the present energy dependence of the $2\nu_1$ excitation is quite similar to the $1\nu_1$ excitation given by Azria and Schulz [167], despite the lack of correction for the analyzer transmission function in the latter spectrum and the different angle of observation.

Excitation enhancements due to the first two shape resonances a^2E_{2u} and b^2B_{2g} are seen in all three spectra. Appreciable vibrational cross section is observed even outside the π^* resonances. It is more pronounced in the $2\nu_1$ and $3\nu_1$ excitation, where a very broad resonance with a maximum near 8.5 eV may be discerned. This resonance has already been reported [167] in the $1\nu_1$ excitation and labelled *g*. Similar broad resonances were observed in the energy dependence of C–H stretch excitation of a number of hydrocarbons and in analogy with these results the resonance *g* is assigned to a σ^*-shape resonance. Because of its width this resonance cannot be discerned in the ET spectrum; it cannot be distinguished from the background of direct scattering, which also has energy variations of similar width. The σ^* resonance is extremely broad in benzene, overlaps strongly with the second π^* resonance *b*, extends even to energies below the resonance *b*, and may even overlap weakly with the first π^* resonance *a*. The explanation of the large width may lie, apart from the very short lifetime, in the presence of two or several overlapping σ^* resonances

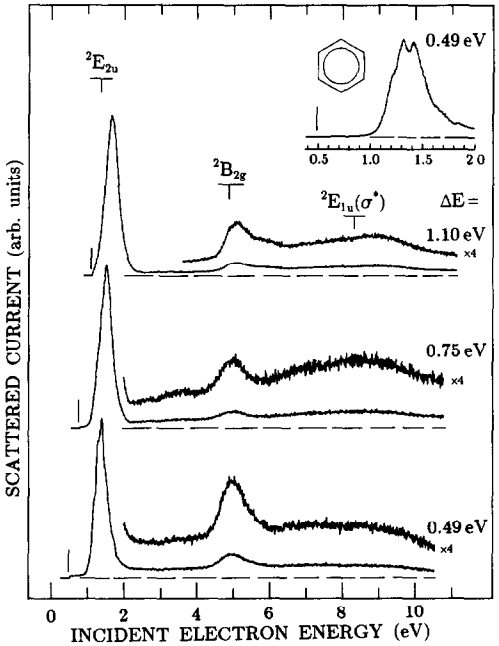

Fig. 40. Energy dependence of vibrational excitation in benzene. The vibrations excited are (from bottom to top) $3\nu_2$ (and overlapping vibrations), $2\nu_1$ and $3\nu_1$. The resonances *a* and *b* are apparent in all three curves, an additional very broad σ^* shape resonance centred at 8.5 eV is visible primarily in the $n\nu_1$ excitation. The insert shows the detail of the $^2E_{2u}$ resonance region in the $\Delta E = 0.49$ eV excitation.

(Section 7.2.8.). In fact a secondary weak maximum appears around 3.5 eV in Fig. 40, although this observation is not quite conclusive since the structure could be caused by a residual "focussing" artifact of the spectrometer (see Appendix).

The overlap of the σ^* resonance with the resonance *b* (and perhaps even *a*) opens the possibility of strong vibronic coupling, which has been predicted to have a pronounced effect on resonant vibrational excitation [169]. The π^* resonance is antisymmetric, and the σ^* resonance symmetric with respect to the molecular plane; the vibrations affected are consequently out-of-plane bending, presumably C–H bending. For resonance *b* the coupling modes are of the e_{2u} or b_{2g} symmetry under the assumption of $a^2(e_{1u})$ or $^2(a_{1g})\sigma^*$ resonances (Section 7.2.7.), that is ν_{19} (C–H bend, 975 cm^{-1}, 121 meV) and ν_{20} (ring deform., 410 cm^{-1}, 51 meV), or ν_7 (C–H bend, 995 cm^{-1}, 123 meV) and ν_8 (ring deform., 703 cm^{-1}, 87 meV). Wong and Schulz [168] report strong excitation of the ν_7 (b_{2u}, C–H bend, 995 cm^{-1}, 123 meV) vibration with incident energy of 4.8 eV, which they could only explain by invoking an $s(a_{1g})$-wave component in the scattering. The ν_7 vibration is, however, experimentally in-

distinguishable from ν_{19} with the resolution of an electron impact experiment, both in terms of its frequency and its isotope shift upon deuteration. In view of the present findings concerning the σ^* resonances it thus appears more plausible to assign the 120 meV vibration excited by 4.8 eV electrons to ν_7 and ν_{19}, with the excitation being induced by vibronic coupling of the π^* and σ^* resonances. Weak excitation of ν_{20} and ν_8 has also been observed experimentally by Wong and Schulz [168].

7.2.3. Energy dependence of electronic excitation

The energy-dependence of the excitation of the lowest triplet state has been investigated by Azria and Schulz [167]. The trochoidal electron spectrometer permitted inclusion of the near-threshold region in the spectra and recording the excitation functions, under higher resolution, for individual vibronic levels of several final states.

The excitation functions of the three lowest triplet states and the $S_3{}^1E_{1u}$ singlet state, from about 0.08 to 10 eV above threshold are presented in Figs. 41–43. Qualitatively they fall into two categories. The excitation of the triplet states has large cross sections at energies below 12 eV, with a number of peaks. In contrast, the cross section for the excitation of the $S_3{}^1E_{1u}$ state is relatively low at threshold and increases linearly with increasing residual energy. The cross section recorded at the energy loss of 6.03 eV, in region 4 of Fig. 32, does not fall into either of these two categories, reflecting the fact that several overlapping bands exist at this energy loss.

All the triplet excitation functions exhibit a series of broad, structureless

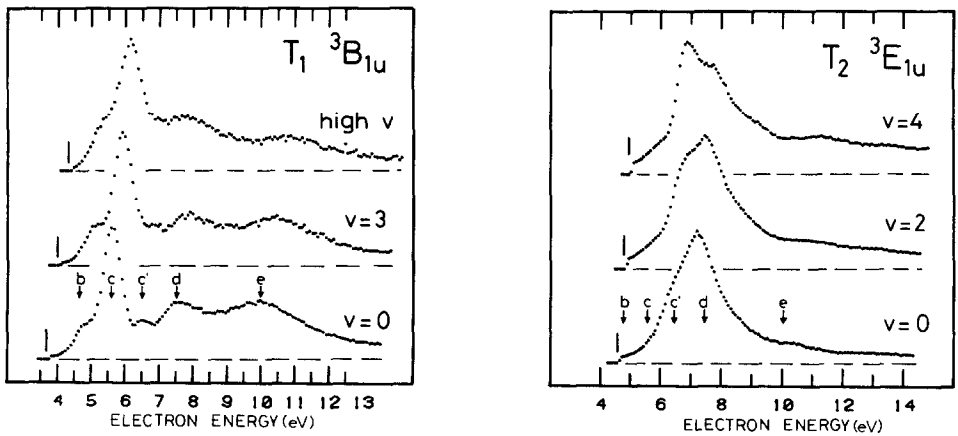

Fig. 41. Energy dependence of the excitation of individual vibronic levels of the lowest triplet state in benzene. Resonant enhancements are indicated by vertical arrows and appropriate labels. The curve labelled "high v" was recorded at $\Delta E = 4.30$ eV.

Fig. 42. Energy dependence of the excitation of the second triplet state in benzene.

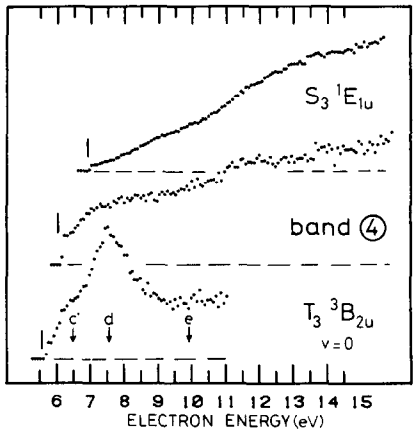

Fig. 43. Energy dependence of the excitation of the higher-lying states in benzene. The curves labelled 'band 4' and 'S_3' were obtained at energy-losses of 6.03 and 6.95 eV, respectively. To bypass the background in the excitation function of the T_3 state caused by the tail of the T_2 state, the signal obtained between the $v=0$ and $v=1$ levels was subtracted from the T_3 $v=0$ curve.

peaks with widths between approximately 0.5 and 2 eV, caused by resonant excitation. The underlying nonresonant (see, however, last sentence of Section 5.2.3.) excitation appears to be weaker, making the resonant excitation mechanism dominant within the first 8 eV above threshold. The nomenclature of the peaks in the triplet excitation functions was taken from ref. 167 and extended to accommodate the newly observed bands *c'* [24]. All the five resonances *b*, *c*, *c'*, *d*, and *e* populate all the triplet states which are energetically accessible, but not with equal probabilities; they have preferred decay channels when several possibilities are open. The $T_1{}^3B_{1u}$ state is populated preferentially by the resonance *c*, $T_2{}^3E_{1u}$ state by the resonances *c'* and *d* (the relative intensity being dependent upon the final vibronic level), and the $T_3{}^3B_{2u}$ state by the resonance *d*.

The position of the observed resonant peak depends upon which final vibronic state was used for the observation. This effect has also been encountered for example in the pure vibrational excitation in the preceding section or in the electron impact excitation of the $A\,^3\Sigma_u^+$ state of N_2 via the $A\,^2\Pi_u$ resonant state of N_2^- [61]. It is probably caused by the "final channel selectivity", the prototype case being the vibrational excitation via Feshbach resonances in H_2 [170]. Note that there is no resonance to excite the T_1 state at threshold and this is the reason for the low intensity of this state in the $E_r=0.03$ eV spectrum of Fig. 33, in comparison with, for example, the T_2 state, excited at threshold via the resonance *b*.

In Fig. 42 the resonances *c'* and *d* appear with different relative intensities in dependence upon the final vibronic level within the $T_2{}^3E_{1u}$ state. This fact is presumably caused by different equilibrium geometries of the *c'* and *d* states

of the anion and the resulting different Franck–Condon profiles. A consequence is the different band-shapes of the T_2 state when observed in energy-loss spectra with different residual energies (Fig. 44). This example illustrates that in energy-loss spectra, recorded under conditions where resonant excitation is significant, the observed band profile may differ from the natural Franck–Condon profile as a consequence of the nuclear relaxation occurring on the potential surface of the transient negative ion. Of further note is the peculiarity in the band shape of both the T_2 (Fig. 44) and the T_1 [24] states when excited via the resonance *b*. In both cases the vibrational structure is "washed-out" in comparison with the band shape when excited via the higher resonances. This observation could be indicative of vibronic coupling, but no definitive explanation can be given at present.

Figure 45 compares the transmission spectrum with the triplet excitation functions, recorded near the centers of the T_1 and T_2 bands. The coincidence in the band energies suggests that the same resonances *b*, *c*, and *c'* are observed in both experiments [22]. The relative intensities of the individual bands in the two experiments suggest the assignment of peak *b* to a predominantly one-particle shape resonance, with a large attachment cross section and a small branching ratio for electronic excitation. On the other hand, the fact that the

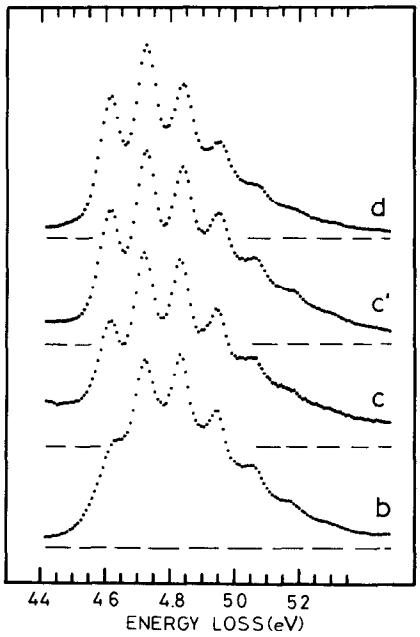

Fig. 44. The $T_2{}^3E_{1u}$ band, recorded with different residual energies, chosen such that the resonances indicated on the right were the intermediates in the excitation. The figure illustrates the dependence of the observed band profile upon the path of excitation.

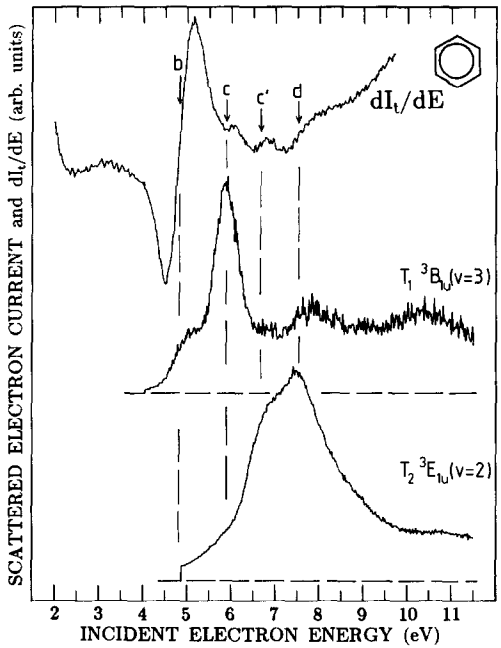

Fig. 45. Comparison of the transmission spectrum (in the derivative form, shown in the top curve) with the excitation functions of the two lowest triplet states in benzene. The vibronic levels lying close to the band centres of the final triplet states were chosen. The same resonances *b*, *c*, *c'*, and *d* appear in all channels, but with differing intensities, depending on the nature of the resonance.

resonance *b* does cause appreciable electronic excitation suggests that the correct description of its electronic structure requires the inclusion of core-excited configurations [38]. The peaks *c*, *c'*, and *d* may be assigned to core excited shape resonances with the configurations $^2(e_{1g}\pi,e_{2u}\pi^{*2})$ (i.e., the $^2B_{1g}$, $^2B_{2g}$, and $^2E_{1g}$ doublet states, with the relative order unknown). The observed selectivity of the decay could provide a guide to the assignment if the corresponding theoretical predictions were to become available.

7.2.4. Threshold electron spectra

In many polyatomic molecules [171, 172] and also, for example, in O_2 [80] the Feshbach resonances, whose decay channel into the parent electronic state is energetically forbidden, decay preferentially by the ejection of a very slow electron, even in cases where no suitable final state of the neutral molecule appears to be present at the energy of the Feshbach resonance, i.e., the resonance lies in the "Franck–Condon gap" of the neutral molecule. The behaviour of the autodetachment of the Feshbach resonances parallels in this sense that of the autoionization of many-atom molecules, where many autoionizing states were found to decay preferentially by the ejection of a very slow electron, re-

sulting in peaks in the Franck–Condon gaps in threshold photoelectron spectra [173, 174].

The above property of Feshbach resonances in polyatomic molecules renders near-threshold energy-loss spectra a very sensitive means of their detection. Benzene was probably the first "large" polyatomic molecule, where a Feshbach resonance was observed by this means [24]. The relevant spectra are shown in Fig. 46. The features due to the excitation of the $^3B_{2u}$ state of the neutral benzene may be differentiated from the features caused by the decay of the Feshbach resonance by the fact that the former remain fixed on the energy-loss (ΔE) scale, whereas the latter are fixed on the incident energy (E_{in}) energy scale and thus move to the left in Fig. 46 as the residual energy is increased. A narrow weak peak at an incident energy of 5.87 eV may be discerned, whose intensity diminishes rapidly with increasing residual energy until it disappears at $E_r > 0.18$ eV. This means that the Feshbach resonance decays by the ejection of an electron whose energy distribution peaks at zero and drops rapidly at higher energies.

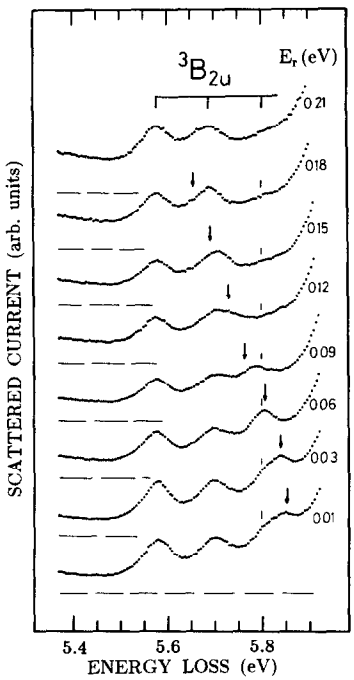

Fig. 46. Energy-loss spectra in the $T_3{}^3B_{2u}$ region, recorded very close to threshold, at residual energies indicated on the right (in eV). The position of a weak peak, due to the decay of the $^2E_{1g}$ Feshbach resonance at 5.87 eV by the ejection of a very slow electron, is indicated by vertical arrows. The peak moves to the left with increasing residual energy because the resonance occurs at a fixed incident energy.

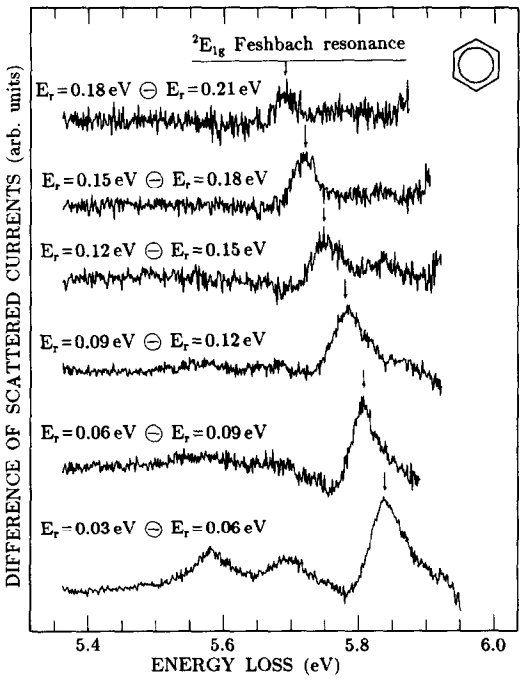

Fig. 47. Digitally calculated difference spectra obtained from adjacent pairs of spectra in Fig. 46. The subtraction factors were chosen visually to eliminate the $T_2{}^3B_{2u}$ state from the spectra as far as possible. The $^2E_{1g}$ Feshbach resonance, giving rise to a threshold electron peak occurring at the fixed incident energy of 5.87 eV, now stands out clearly. The vertical scales of the individual difference spectra were chosen arbitrarily for clear presentation; in reality the intensity of the peak diminishes rapidly with increasing residual energy.

The resonant feature fixed in the incident energy is quite weak in benzene and its visibility is substantially improved in the difference spectra shown in Fig. 47.

Using the known relations of the energies of Feshbach resonances and their parent states [18, 140, 142], the present Feshbach resonance may be assigned as the $^2(e_{1g}\pi,3s^2)^2E_{1g}$ state, with two electrons moving in the 3s-Rydberg orbital. Its parent state is the $3s$–$^3E_{1g}$ Rydberg state at 6.28 eV (see Fig. 35). Conversely, the observation of the Feshbach resonance at 5.87 eV lends support to the assignment of the energy-loss peak at 6.28 eV to the lowest Rydberg state in benzene.

7.2.5. Dissociative attachment

Negative ion yield from benzene without mass analysis was reported by Azria and Schulz [167], who observed a broad peak at 8.0 ± 0.3 eV and assigned it to the same resonance *g* which is seen in the energy dependence of vibrational excitation.

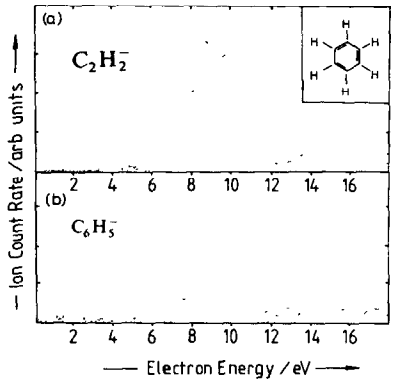

Fig. 48. Yields of fragment negative ions from benzene. (From ref. 175.)

Figure 48 shows the results of a more detailed study by Fenzlaff and Illenberger [175]. A weak band peaking around 4.5 eV may be discerned in the $C_2H_2^-$ yield and may be assigned to the dissociation of the b^2B_{2g} resonance. This assignment is supported by the fact that Fenzlaff and Illenberger [175] also observed an ion-yield band at this energy in some of the fluorinated benzenes, often with a much higher intensity than in benzene itself. The broad $C_2H_2^-$ band peaking around 9 eV may stem from the dissociation of the g^2E_{1u} σ^* resonance. Its narrower width, however, makes the assignment to the $^2(e_{2g}\sigma,3p^2)$ resonance, proposed to lie around this energy by Robin [176] equally probable. Fenzlaff and Illenberger [175] further observed a narrow $C_6H_5^-$ band at 8.0 eV. This band does not seem to have a counterpart in any of the other experiments and has about the right energy for the $^2(e_{2g}\sigma,3s^2)$ assignment.

7.2.6. Relation to fluorescence and metastable excitation

The relation of the T_1 excitation function, determined in electron scattering experiments, to the total metastable and the fluorescence yields has been discussed by Azria and Schulz [167]. Figure 49 compares the fluorescence and metastable yields of Smyth et al. [177] with the T_1 and T_2 excitation function determined by the TES. As already noted by Azria and Schulz [167], the T_1 excitation function is strikingly similar to the metastable curve, supporting the conclusion that the metastable particles are benzene molecules in their lowest triplet state. The differences in the relative intensities of the individual bands in the two experiments could stem from the difference in angle of observation (TES: 0° and 180°; metastable yield, integrated over all angles).

The electron impact excitation function of the $S_1{}^1B_{2u}$ state could not be determined because of the overlap with the $T_2{}^3E_{1u}$ state. The S_1 state does not, however, appear to be appreciably excited at electron energies below 10 eV, as can be seen in the energy loss spectra of Fig. 33. The fluorescence yield spectrum does exhibit a band which does not coincide with any of the bands in the

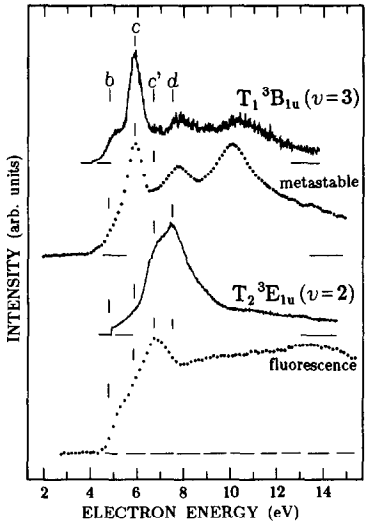

Fig. 49. Comparison of the present T_1 and T_2 excitation functions with the total metastable and total fluorescence production curves of Smyth et al. [177]. The similarity of the T_1 and the metastable curves is striking.

metastable yield, but which occurs at the same energy as the c' band in the T_2 excitation function. The possible explanations for this band appear to be:

(a) The resonance c' also decays into the S_1 state.

(b) There is an additional resonance (labelled *f* in ref. 167), accidentally at the same energy as c', which decays into the S_1 state.

(c) Finally, there is the interesting possibility that the T_2 state is formed initially by decay of resonance c' and subsequently undergoes a $T_2 \rightarrow S_1$ intersystem crossing, which could be quite fast because of the overlap of the two states, resulting in fluorescence.

7.2.7. Relation to core excitation

In electron energy-loss spectroscopy with incident energies of several kiloelectronvolts, peaks at energy losses of several hundred electronvolts may be observed, which correspond to excitation of electrons from the *K*-shell. The initial orbital is essentially an atomic 1*s* orbital and the final orbital an unoccupied valence MO. Because of the small overlap of the initial and final orbitals the transitions in a certain sense "map" the virtual MOs of the molecule and may therefore be meaningfully compared with the energies of the ("simple") shape resonances, observed in low-energy transmission and energy-dependence of vibrational excitation spectra.

The core excitation spectra of benzene have been reported by Hitchcock and Brion [178] and recently by Horsley et al. [179]. The spectrum of the latter authors is compared with the present vibrational excitation spectrum in Fig.

50. Horsley et al. [179] assign the three prominent bands in their spectrum to transitions to the $\pi^*(e_{2u})$, $\pi^*(b_{2g})$, and $\sigma^*(e_{1u})$ virtual MOs, the assignment being based on multiple scattering $X\alpha$ calculations and auxiliary experimental data. The striking similarity of the two types of spectra underlines the relation of both experiments to the same virtual orbitals. The correspondence of the bands further supports the assignment of Horsley et al. [179]. Conversely, the identification of the lowest σ^* orbital as e_{1u} by the $X\alpha$ calculation and experiments of Horsley et al. [179] suggest the assignment of the 8.5 eV band in the vibrational cross section spectrum to the $^2E_{1u}$ shape resonance.

The core excitation spectra generally also have bands corresponding to transitions to Rydberg orbitals. Thus Horsley et al. [179] assign the weaker feature at $\Delta E = 287.2$ eV in benzene to the $3p$ Rydberg level. It is interesting that the weak feature at 3.5 eV in the $n\nu_1$ excitation spectrum occurs at an energy corresponding to the $3p$ feature in core excitation (Fig. 50). This observation raises the speculation that a $^2(3p)$ resonance could be present in benzene at 3.5 eV. On the other hand the diffuse nature of the Rydberg orbital probably does not result in a sufficiently high centrifugal barrier to capture an electron.

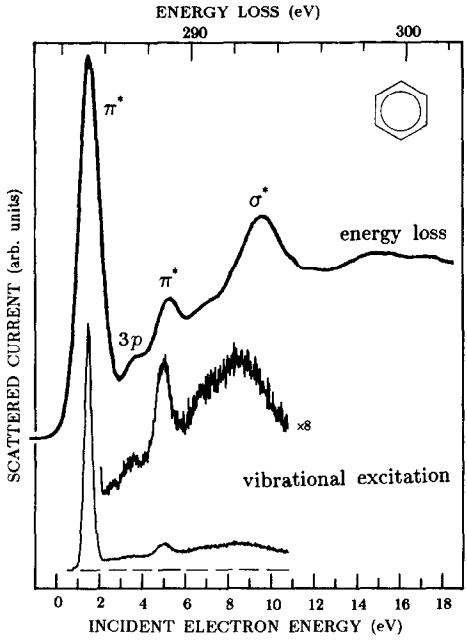

Fig. 50. Comparison of the present vibrational excitation ($2\nu_1$, lower two curves) with the core excitation energy-loss spectra of Horsley et al. [179]. The two spectra were arbitrarily aligned at the maxima of the first band. The bottom energy scale refers to the vibrational excitation, the top energy scale to core excitation. The qualitative similarity of the curves supports the interpretation where the same π^* and σ^* orbitals are occupied in the core excitation transitions and in the capture of low energy electrons to form shape resonances.

The $n\nu_1$ vibrational excitation around 3.5 eV is thus more probably due to a σ^* resonance.

A limitation of the comparison of core excited states with shape resonances is borne out by the significantly larger spacings between the bands in core excitation.

7.2.8. Relation to theory and conclusions

The results of the preceding paragraphs may be summarized in a diagram of the hitherto known short-lived negative ion states, shown in Fig. 51. This figure represents an extension of the diagram previously given by Azria and Schulz [167], augmented by a number of new resonances and more extensive information on the decay channels. The diagram emphasizes the necessity of investigating as many decay channels as possible, that is applying several electron impact methods, to obtain a comprehensive picture of the electronic structure of the negative ion. The knowledge of the decay channels is also

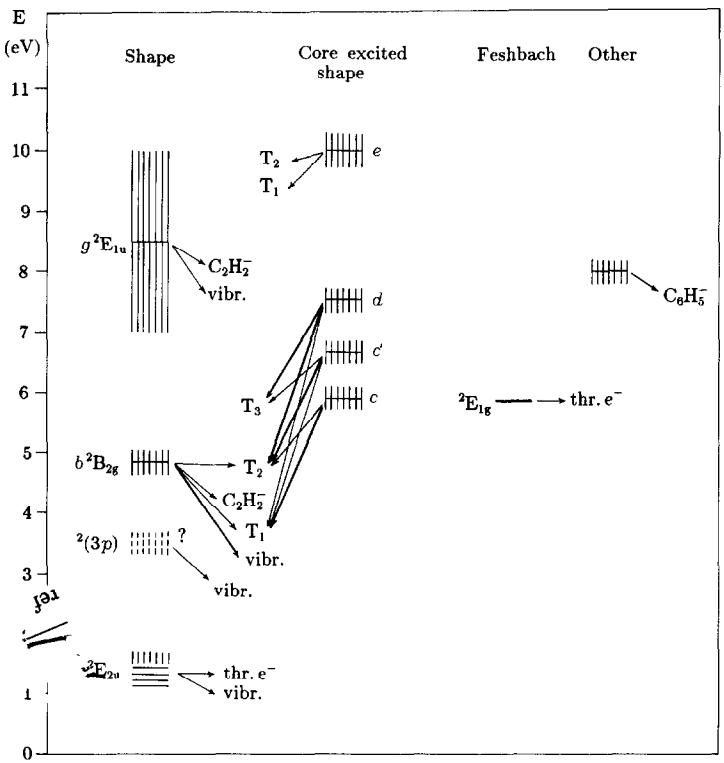

Fig. 51. Diagram of the short-lived negative ion states of benzene, including the important decay channels. In the designation of the decay channels T_1, T_2, and T_3 stand for the first three triplet states, 'vibr.' for vibrational excitation, and 'thr. e^-' for ejection of a near-zero kinetic energy electron.

essential for the assignment of the resonances. The energies of the resonances are listed in Table 2.

Several calculations of the energy levels of the benzene radical anion may be found in the literature. Kuhn et al. [180] calculated the transition energies in the frameworks of the PPP and CNDO approximations (these authors also give references to earlier calculations.) Lindholm and Åsbrink [181] calculated the energy levels by the semiempirical HAM method. Guerra et al. [39a] calculated the energies of the shape resonances with the MS-$X\alpha$ method. The results of these calculations are compared with the experimental results in Table 2, and may be commented upon as follows:

(a) The HAM method gives a very accurate value for the first attachment energy.

(b) The results of PPP, CNDO, and HAM-CI calculations all underestimate the energy of the b^2B_{2g} state by 1–1.5 eV. This fact could lead to speculations that the 4.8 eV band in ETS and other electron scattering experiments has a different origin. The experimental evidence for the assignment of this band to

TABLE 2

Experimental and theoretical resonance energies (eV) in benzene (experimental energies refer to band centers except where otherwise noted)

Label	Energy	Type	Dominant configuration	Theory			
				PPP[a]	HAM-CI[b]	HAM[c]	$X\alpha$[d]
a^2E_{2u}	1.13[e] 1.40[f]	π^* shape	$^2(e_{2u}\pi^*)$		1.1	1.11	1.3
{	3.5[g]	$(\sigma^*?)\}$					
b^2B_{2g}	4.8_4	π^* shape	$^2(b_{2g}\pi^*)$	3.37	3.76	4.86	4.6
$^2E_{1g}$	5.87	Feshbach	$^2(e_{1g}\pi,3s^2)$				
c	5.8_9	Core exc. shape	$^2(e_{1g}\pi,e_{2u}\pi^{*2})$	5.17(E_{1g})	5.9	6.53	
c'	6.6_7			6.93(B_{1g})	6.9	6.67	
d	7.54			6.95(E_{1g})	8.3	6.87	
	8.0[h]	Feshbach?	$^2(e_{2g}\sigma,3s^2)$?				
g	8.5	σ^* shape	$^2(e_{1u}\sigma^*)$				
e	10.0	Core exc. shape	?				

[a]The experimental attachment energy of 1.13 eV plus the calculated transition energies, ref. 180.
[b]Ref. 181.
[c]The HAM configuration energies without CI [181].
[d]MS-$X\alpha$ calculation, ref. 39a.
[e]First vibrational peak.
[f]Approximate band centre.
[g]Tentative observation.
[h]Observed only in dissociative attachment [175].

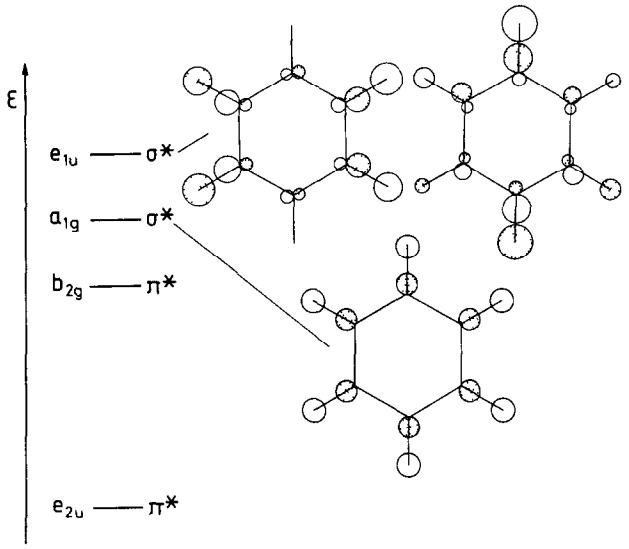

Fig. 52. Diagram of the energies and shapes of the virtual orbitals in benzene, obtained by an ab initio calculation with an STO-3G basis set [182]. The orbital diagrams have been drawn with the MOPLOT program [183, 184].

the second π^* shape resonance appears, however, too convincing to permit a reassignment.

(c) All calculations predict three $(\pi)^3(\pi^*)^2$ core excited states in the 5–8 eV region, in semiquantitative agreement with experiment.

(d) The HAM configuration energies without CI lie remarkably close to the experimental values. An excellent agreement with the experiment could be achieved if the magnitudes of the off-diagonal elements in the HAM CI-matrix would be reduced; in other words it seems to follow from experiment that the configuration mixing is somewhat overestimated.

Figure 52 shows a diagram of virtual orbitals in benzene. Qualitative information on the benzene shape resonances may be obtained from this diagram through the application of the Koopmans' theorem. The separation of the two π^* orbitals is much larger than the separation of the two corresponding resonances, underlining the qualitative nature of the orbital–resonant state comparison. The discrepancy could be caused by the small basis set used in the calculation and the neglect of CI, which would push the resonance b down in energy and thus reduce the separation. Two useful conclusions may, however, be drawn from the diagram in Fig. 52:

(a) Two σ^* levels, a_{1g} and e_{1u}, are found in the vicinity of the upper π^* orbital. The a_{1g} orbital, associated with s-wave scattering, may not result in a shape resonance. The very broad structure in the ν_1 vibrational excitation is thus probably due to a $^2(e_{1u})$ shape resonance.

(b) Both a_{1g} and e_{1u} orbitals have nodes between the C and H atoms. This implies that the corresponding shape resonance has appreciably longer C–H bonds, resulting in a large impulse along the ν_1 normal coordinate and dominant excitation of the ν_1 symmetrical stretch vibration.

The absorption spectrum of benzene anion in a low temperature matrix has also been reported by Shida and Iwata [185]. They observed a very broad band with a maximum near 3 eV and with a long tail towards lower energies, and a second narrower band with a maximum near 4.3 eV. The latter band agrees in energy with the $c \leftarrow a$ transition, for which the transition energy predicted from the gaseous phase data is $5.89 - 1.40 \simeq 4.5$ eV (difference of band centres). The gaseous phase data predict a transition energy of $4.84 - 1.4 \simeq 3.45$ eV for the lower energy transition $b \leftarrow a$, which is higher than observed in the matrix. The difference could perhaps be due to solvent effect, but the extreme width of the first absorption band in the matrix remains somewhat puzzling.

An important conclusion of this section is the indication of the importance of considering vibronic coupling of overlapping resonances for understanding the details of resonant vibrational excitation in benzene.

8. NAPHTHALENE

8.1. Electronic structure of neutral naphthalene

An extensive literature has been devoted to the optical spectroscopy of naphthalene. Gas phase absorption spectra have been given for example by George and Morris [186] and by Koch et al. [187]. Two triplet energies have been determined, among others, by absorption of ultrapure, four centimetres long single crystals at liquid helium temperatures by Hanson and Robinson [188] and by phosphorescence of crystals at 77 K by Priestley and Haug [189]. Electron energy-loss spectra with 100 eV incident energy, revealing a number of singlet excited states, have been reported by Huebner et al. [190]. Threshold electron spectra, obtained by the trapped-electron method with retarding potential difference (RPD) (used for reduction of electron energy spread), have been reported by Pisanias et al. [191] and interpreted in terms of states of both neutral naphthalene and its negative ion.

Energy-loss spectra obtained with the trochoidal electron spectrometer are shown in Fig. 53 and Table 3. The spectrum recorded with $E_r = 40$ eV agrees very well with the absorption spectrum of George and Morris [186]. The two triplet states $^3B_{1u}$ and $^3B_{2u}$, observed previously in the crystal absorption work of Hanson and Robinson [188], appear at $E_r = 2$ eV. A third π,π^* triplet state has been predicted at 4.25 eV by the CNDO/CI calculations of Hofer and Hedges [193], but no corresponding band can be reliably discerned in Fig. 53, perhaps because of the overlap with the $^3B_{2u}$ and the $^1B_{1u}$ bands. A further new band appears at $\Delta E = 5.20$ eV. The similarity of its band shape with the first pho-

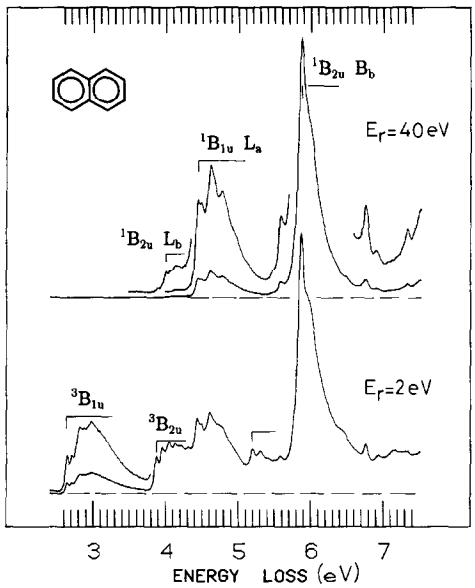

Fig. 53. Energy-loss spectra of naphthalene. The symmetry designation as well as Platt's notation [192] are given.

TABLE 3

Transition energies (eV) in naphthalene

Present work	Absorption		Assignment
	Gas[a]	Crystal[b]	
2.63		2.629	$^3B_{1u}$
3.87_4		3.817	$^3B_{2u}$
4.00	3.970	3.902	$^1B_{2u}$ (L_b)
4.43_7	4.452		$^1B_{1u}$ (L_a)
5.20			Rydberg, $\delta=0.85$
5.87_4	5.893		$^1B_{2u}$ (B_b)

[a]Ref. 186.
[b]Ref. 188.

toelectron band [141, 194] suggests that it could be a Rydberg band with a quantum defect $\delta=0.85$, although an assignment to a triplet valence state cannot be excluded. It is interesting to notice that the 1^1B_{3g} and 2^1A_g states, reported in two photon absorption by Dick and Hohlneicher [195] cannot be observed in the present energy-loss spectra.

8.2. Electron transmission spectrum

The ET spectrum of naphthalene has been reported by Jordan and Burrow [21], Mathur and Hasted [166], and Allan [196]. Detailed spectra and the first satisfactory assignment have been given by Burrow et al. [22]. The subject has been reviewed by Jordan and Burrow [23].

A non-derivative transmission spectrum obtained with the present instrument is shown in Fig. 54. The approximate "ETS" cross section varies considerably with the incident energy and, with the exception of the resonance at 1.65 eV, the resonant structure is weak, much weaker than, for example, in nitrogen (Fig. 20) or benzene (Fig. 37). Naphthalene thus demonstrates clearly the advantage of the derivative representation of the transmission spectrum, shown in Fig. 55, for detection of resonant structure. On the other hand the spectra in the Figs. 54 and 55 show that it is more difficult to assess visually the relative intensities of the ETS bands in the derivative representation; whereas it is immediately clear from Fig. 54 that the band *c* affects most strongly the cross section, this fact is much less obvious when regarding the derivative representation on Fig. 55. The experimental attachment energies are summarized in Table 4. The present spectrum was recorded and calibrated before the

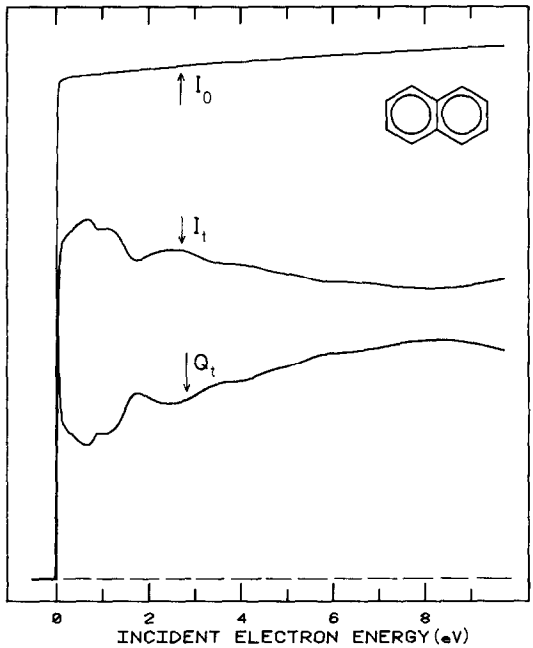

Fig. 54. Illustration of the electron transmission experiment in naphthalene. Shown are the incident and the transmitted electron currents and the ETS-approximation of the total cross section, Q_t, determined as $\ln(I_0/I_t)$.

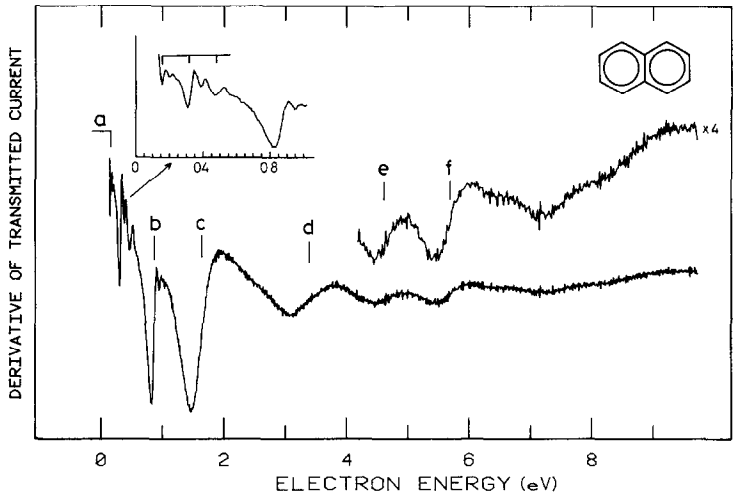

Fig. 55. The derivative representation of the transmission spectrum in naphthalene. An expanded view of the 0–1 eV range is shown in the insert.

TABLE 4

Attachment energies (eV) in naphthalene

Band	Present work	Burrow et al. [22]	Assignment (Burrow et al. [22])
a	0.16	0.19	π_1^*
b	0.87	0.90	π_2^*
c	1.65	1.67	π_3^*
c'		≈ 2.5	$\pi_4^* + \pi_5 \rightarrow \pi_1^*$
d	3.40	3.38 (two bands)	$\pi_4^* + \pi_5 \rightarrow \pi_1^*$; $\pi_5^* + \pi_3 \rightarrow \pi_1^*$
e	4.64	4.72	$\pi_5^* + \pi_3 \rightarrow \pi_1^*$
f	5.71	5.67	2p, 1h

publication of the data of Burrow et al. [22] and the good agreement of the two data sets demonstrates the reliability and reproducibility of the attachment energies determined by ET spectroscopy when the numerical values are determined in a consistent manner, that is as energies of the midpoints between the minima and the maxima of the derivative curve.

A detailed interpretation of the ET spectrum and comparison with the absorption of the naphthalene negative ion in a low-temperature matrix have been presented by Burrow et al. [22] and by Jordan and Burrow [23]. The first three ET bands have been interpreted as essentially a capture into the three lowest virtual orbitals of naphthalene whereas strong mixing of one par-

ticle (1p) and two particle, one hole (2p, 1h) configurations has been found to occur in the higher resonances.

8.3. Near threshold energy-loss spectra

The role of the resonance in vibrational and electronic excitation in the first 3 eV above threshold is illustrated in the near-threshold energy-loss spectra of Fig. 56. Two types of structure may be recognized in these spectra: structure which remains fixed on the energy-loss scale when the residual energy is varied corresponds to individual vibrational and electronic states of naphthalene; structure which moves to the left as the residual energy is increased corresponds to excitation enhancements caused by resonances.

The resonances *a*, *b*, *c* and *d* cause strong unspecific (see Section 15) excitation, that is they result in a strong production of slow electrons regardless of

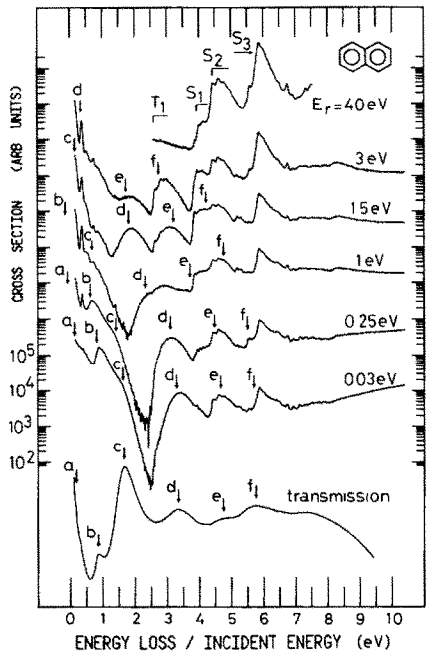

Fig. 56. Energy-loss spectra of naphthalene recorded at constant residual energies given on the right. The spectra are shown on a semilogarithmic scale to accommodate the large signal intensity variations (1:10^4 in the E_r=0.03 eV spectrum). The transmission spectrum is shown for comparison in the bottom curve. The ET spectrum is shown on a linear (i.e., not logarithmic) scale; a direct (i.e., not derivative) representation has been chosen to facilitate the comparison of band shapes, and the spectrum has been strongly expanded vertically and slightly "tilted" (cf. Fig. 54) to improve the visibility of the resonances. The incident energies corresponding to the individual resonances *a*–*f* have been labelled by vertical arrows above the spectra. The abscissa label "incident energy" refers to the transmission spectrum.

whether a suitable final state occurs (in the Franck–Condon region) at the energy of the resonance. As a result, structureless bands occur at incident energies corresponding to these resonances in the spectra. These bands are extremely intense in the $E_r = 0.03$ eV spectrum and their intensity (relative to the electronic excitation) diminishes with increasing energy above threshold. The same resonances also result in selective excitation of specific vibrational levels at low energy losses and $E_r \geqslant 1$ eV. These findings parallel those found in *p*-benzoquinone which are described in Section 9.2.

Two minor but interesting details in Fig. 56 are pointed out as a concluding remark:

The resonance *d* causes an intense structureless peak in the $E_r = 0.03$ eV spectrum at exactly its energy, $E_{in} = 3.4$ eV, although this energy falls between the two electronic states $^3B_{1u}$ and $^3B_{2u}$, which manifest their presence merely as a weak shoulder and a weak structure on the low and high energy sides of the *d* band. This observation underlines how unspecific, or unselective is the excitation at threshold; both very high vibrational levels of the electronic ground state and excited vibrational levels of the $^3B_{1u}$ and $^3B_{2u}$ electronically excited states could be the final states in the threshold decay of the resonance *d*.

Even the resonance *e* causes unspecific excitation, visible at $E_r = 1$ eV, where it fills the gap between the $^3B_{1u}$ and $^3B_{2u}$ states, and further a weak, yet discernible, structureless band in the gap below the lowest electronically excited state even at $E_r = 3$ eV.

8.4. Energy dependence of vibrational and electronic excitation

Figure 57 shows several examples of energy dependence spectra. The upper three curves are recorded at energy-losses corresponding to electronic excitations. It must be realized, however, that because of the unspecific excitation described in the preceding section the final states could partly be very high vibrational levels of the electronic ground state in the near threshold region. Thus the peak *d* in the excitation function with $\Delta E = 2.97$ eV could have contributions both from the excitation of the $^3B_{1u}$ lowest triplet state and the vibrational continuum of the electronic ground state.

The excitation function of the $^1B_{2u}$ states is essentially a linearly rising function of excess energy and resembles in this respect the excitation function of the $^1E_{1u}$ state in benzene (Fig. 43), underlining the related nature of the two states. The excitation function of the $^1B_{1u}$ (L_a) state has not been determined because of the overlap of this state with the $^3B_{2u}$ state.

The excitation functions of the two lowest triplet states show rich resonant structure. The strong decay of the resonances *e* and *f* into the triplet states supports the conclusion of Burrow et al. [22] that these resonances have considerable (2p, 1h) character. As in the case of benzene (Figs. 41 and 42), the position of the resonant peaks in the excitation functions depends to some

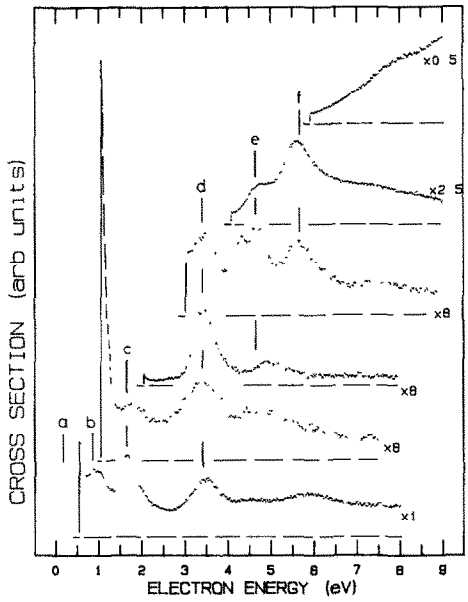

Fig. 57. Excitation functions in naphthalene, recorded at the energy-losses (from bottom to top) of 0.5, 1.0, 2.0, 2.97, 4.03 and 5.86 eV. The lower three curves correspond to pure vibrational excitation, the upper three curves to the excitation of the $^3B_{1u}$, the $^3B_{2u}$, and the $^1B_{2u}$ electronically excited states. All curves are shown approximately on the same vertical scale, expanded as indicated by the multiplication factors.

degree on which vibrational level of the electronic band is measured. This effect has probably a Franck–Condon origin. The peak positions agree best with the attachment energies determined in ET spectroscopy when excitation functions of centres of the electronic band are recorded. A shoulder appears in the $^3B_{1u}$ excitation at 4.3 eV, just below the energy of the resonance *e*, and could correspond to the (3p, 2h) state observed near 4.4 eV in the absorption spectrum of naphthalene anion [185], and not visible in the ET spectrum [22].

The three vibrational cross sections in Fig. 57 are recorded at relatively high energy-losses, where the unspecific excitation dominates. The curves reflect the observation already made in Fig. 56 that each of the resonances *a*–*d* leads to an intense production of threshold electrons, causing a threshold peak whenever the threshold falls within a resonance. Thus the tail of the resonance *a* appears to cause a threshold peak in the $\Delta E = 0.5$ eV excitation function and the resonance *b* causes a pronounced threshold peak in the $\Delta E = 1.0$ eV excitation function.

9. ANTHRACENE

This section discusses briefly the energy-loss and energy dependence spectra of anthracene. The transmission spectrum of this molecule has been discussed

in great detail by Burrow et al. [22]; the spectrum recorded in this laboratory is very similar to that of Burrow et al. and will not be reproduced here.

The energy-loss spectra recorded at two representative energies are shown in Fig. 58. The transition energies are summarized and compared with the results of optical absorption studies in Table 5. The present energies of the L_a and L_b singlet states agree well with the gas absorption data. The shift between the present gas phase energy of the first triplet state and the optically determined energy of this state in the crystal is only 0.045 eV. The dipole forbidden

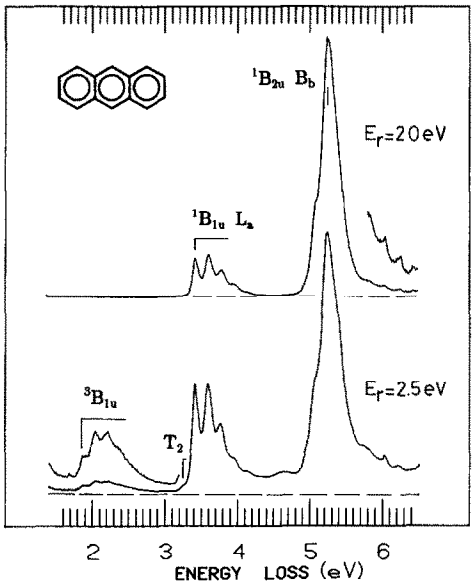

Fig. 58. Energy-loss spectra of anthracene.

TABLE 5

Transition energies (eV) in anthracene

Present work	Absorption		Assignment
	Gas[a]	Solid	
1.87_4		1.829 (crystal)[b]	$^3B_{1u}$
3.24_6		3.230 (polymer)[c]	$^3B_{3g}$
3.40_8	3.422	3.154 (crystal)[c]	$^1B_{1u}$ (L_a)
5.24_2	5.241		$^1B_{2u}$ (B_b)

[a]Refs. 197, 198.
[b]Ref. 199.
[c]Ref. 200.

transition to the $^1B_{2u}$ (L_b) state at 3.72 eV [197] is not discernible underneath the L_a band in the present spectra.

A shoulder appears at 3.24_6 eV at the $E_r = 2.5$ eV spectrum in Fig. 58 and other spectra with residual energies in the range 0.2–3.5 eV. The shoulder disappears at $E_r = 20$ eV and thus cannot be a hot band of the $^1B_{1u}$ state. The intensity of the shoulder is comparable to the intensity of the $^3B_{1u}$ state. The energy dependence of the shoulder, shown in Fig. 59 is characteristic of a triplet state; it is dominated by a single resonance near 4.6 eV. The shoulder is therefore assigned to the second triplet state T_2. Comparison with the theoretical prediction of Pariser [201] suggests that it is the $^3B_{3g}$ state.

The energy of the T_2 state has been determined to be 3.23 eV by Kellog [200], who added the energy of a transient $T_1 \rightarrow T_2$ absorption in polymethylmethacrylate to the T_1 energy of Padhye et al. [202]. Kellog [200] concluded that the T_2 state lies 0.08 eV lower than S_1 in solution (in contrary to the crystal where T_2 lies higher than S_1). This conclusion has been supported by the work of Fukumura et al. [203], who measured the activation barrier for

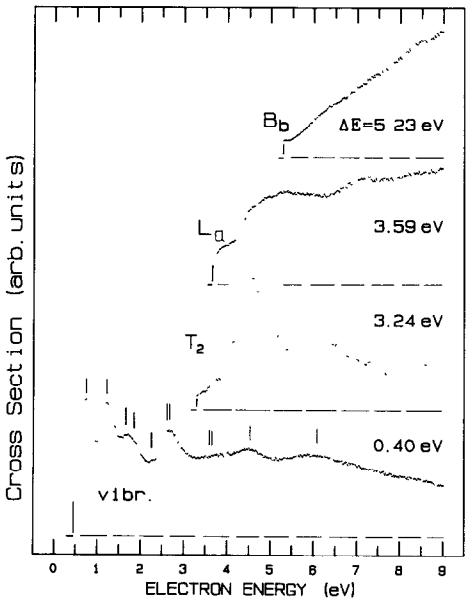

Fig. 59. Energy dependence curves in anthracene. Approximate positions of the resonances reported by Burrow et al. [22] in ETS are indicated by vertical lines above the energy dependence of vibrational excitation, $\Delta E = 0.4$ eV. The energy dependence with $\Delta E = 3.24$ eV is dominated by resonant excitation. It is qualitatively similar to the excitation function of the T_2 state in benzene (Fig. 42), supporting the assignment of the 3.24 eV shoulder to the T_2 state. The energy dependence of the $^1B_{1u}$ state is reminiscent of the excitation of the $^1B_{1u}$ state in benzene (Fig. 43), underlining the related nature of the two states. There is also a striking similarity in the excitation functions of the $^1B_{2u}$ state in anthracene and the $^1E_{1u}$ state in benzene.

the inverse $T_2 \rightarrow S_1$ intersystem crossing (in ethanol) to be 0.086 eV. The present work shows that in the gas phase T_2 lies below S_1 by 0.16 eV, an amount even larger than in solution.

All the resonances observed by Burrow et al. [22] in ETS (perhaps with the exception of the resonance near 3.6 eV) can be seen in the energy dependence of vibrational excitation in Fig. 59. The exact peak positions depend to some degree upon which energy-loss the spectrum has been recorded and the peak positions in Fig. 59 are therefore not exactly equal to the energies determined by ETS. It is interesting to observe that the resonance near 4.6 eV, assigned to $\pi_7^* + 2p, 1h$ by Burrow et al. [22], is pronounced in ETS, vibrational excitation and electronic excitation of the T_2 state. This observation supports the conclusion of Burrow et al. [22] that configuration interaction in the negative ion states is much more important in anthracene than in benzene (Section 7.2.3.). Because of configuration interaction both the electronic ground state and an electronically excited state may be considered parent states of the resonance, making both the vibrational and electronic excitation decay channels important.

10. AZULENE

10.1. Electronic structure of neutral azulene

A striking feature of azulene is the unusual properties of its lower excited states, reported by Beer and Longuet-Higgins [204]. They had found a rather strong fluorescence $S_2 \rightarrow S_0$ from the second excited singlet state, but they had not been able to detect an $S_1 \rightarrow S_0$ fluorescence or a $T_1 \rightarrow S_0$ phosphorescence. These properties have been ascribed to the unusually small S_0–S_1 and unusually large S_1–S_2 energy gaps, which cause the radiationless deactivation of the S_1 state to be fast and that of the S_2 state unusually slow.

The triplet energy of azulene has been determined by triplet quenching experiments (see for example ref. 205) to be 1.69 ± 0.025 eV. A very reliable value for the energy of the T_1 state has been obtained by Klemp and Nickel [206], who have recently been able to detect the $T_1 \rightarrow S_0$ phosphorescence in azulene-doped phenazine crystals at 30 K, and found the energy of the *O–O* transition to be 1.720 eV. This results in the T_1 state being only 0.060 eV below the S_1 state in the solid state.

The present energy-loss spectra are displayed in Fig. 60 and data summarized in Table 6. The spectrum recorded at the higher residual energy is very similar to the gas phase absorption spectra reported by Heilbronner and Wieland [207], Weigang [208], and Kitagawa et al. [209] (the last spectrum being offprinted in ref. 210). The spectrum is also similar to the condensed phase spectra (see for example ref. 211), except that the Rydberg transitions above

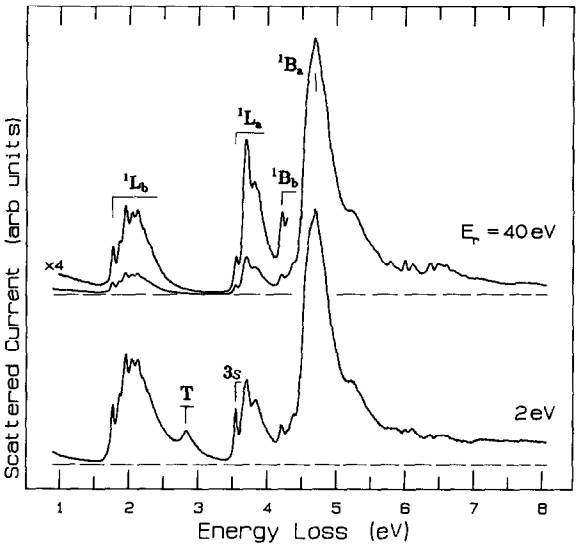

Fig. 60. Energy-loss spectra in azulene.

5.6 eV disappear in the condensed phase and the solvent shifts are different for different electronic transitions.

Three interesting observations can be made on the spectrum recorded 2 eV above threshold:

(1) No band which could be assigned to the T_1 state can be discerned. This finding supports the conclusion of Klemp and Nickel [206] that the T_1 and S_1 states nearly coincide the energy.

(2) A band observed at 2.83 eV can be assigned to a triplet state. The absence of vibrational structure on this band points to a rapid intersystem crossing to the S_1 state. The CNDO/2 calculations of Hofer and Hedges [193] predict four triplet states in the 1.6–3.4 eV range and it is not immediately obvious which assignment should be given to the newly observed triplet state.

(3) The intensity of the peak at 3.55 eV relative to the immediately following peaks at 3.705 and 3.835 eV is greatly enhanced in the $E_r = 2$ eV spectrum. This enhancement is more dramatic than the usual dependence of a band shape on the residual energy, which has been encountered for example in benzene (see Fig. 44). The only convincing explanation of this experimental observation is to assume a separate electronic transition at 3.55 eV. The 3.55 eV peak in UV absorption is generally assumed to be the 0_0^0 vibronic transition of the ^1L_a band and the new transition in the energy-loss spectrum appears to coincide with the UV band within 0.01 eV.

Valence MO calculations do not predict any additional singlet $\pi\pi^*$ transitions in this energy region. The new transition could be a triplet state, or a Rydberg transition with a quantum defect $\delta = 1.12$ (using IE = 7.43 eV [213,

214]), such as the $2a_2\pi \rightarrow 3s$ transition which has been predicted to be "totally engulfed by the $\pi \rightarrow \pi^*$ absorption in the 3.1–4.3 eV region" by Robin [215].

10.2. Electronic structure of the negative ion

The transmission spectrum of azulene was measured by Burrow [216]. Figure 61 shows the transmission spectrum obtained with the trochoidal electron spectrometer. A threshold energy-loss spectrum, shown in Fig. 62 (similar, but lower resolution spectra were given in ref. 217), indicates one further resonance, *a*, causing intense unspecific vibrational excitation in the 0–0.5 eV energy-loss region. The energies of the resonances, determined from the two spectra, are summarized in Table 7.

The resonance *c* results in a strikingly high intensity of threshold electrons (Fig. 62, $E_r = 0.03$ eV), about ten times higher than the intensity of the electronic excitation in the 3.5–6 eV energy-loss region, and higher than any other resonance with the exception of resonance *a*. (This effect resulted in the very intense threshold electron signal in the SF_6^- scavenger spectra of Huebner et al. [218].) Spectra with $E_r = 0.03$–1.0 eV indicate, furthermore, that this resonance is more efficient at exciting the S_1 electronically excited state (and perhaps the underlying T_1 state), than at exciting the vibrational continuum below $\Delta E < 1.5$ eV, suggesting that S_1 and T_1 could be the parent states of the resonance *c*.

Electronic transition energies of the azulene negative ion have been calculated using the semiempirical open shell PPP-CI procedure by Nykl et al. [219] (and reviewed by Čársky and Zahradník [220]), and by Shida and Iwata [185]. The values given in Table 7 were calculated in our laboratory using a procedure very similar to that of Čársky and Zahradník [220]. The calculated energies may be compared with the present attachment energies when the electron affinity is known.

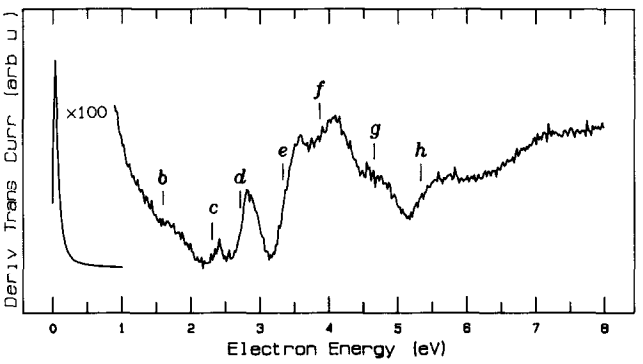

Fig. 61. Electron transmission spectrum of azulene.

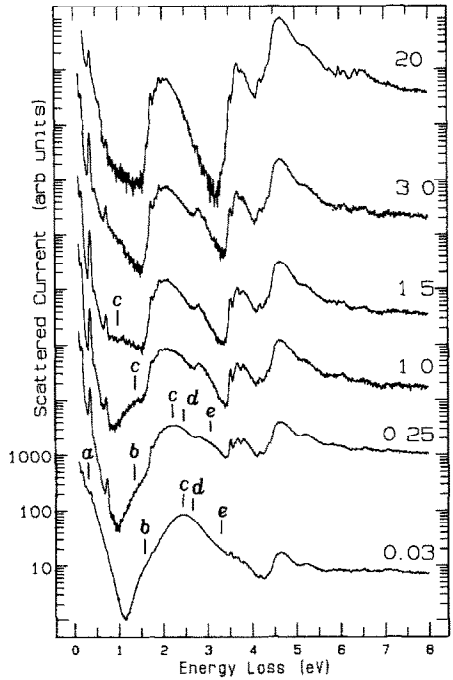

Fig. 62. Energy-loss spectra of azulene, recorded at the constant residual energies indicated on the right. The spectra are shown on a semilogarithmic scale to accommodate the large range of signal intensities. Positions of resonances are indicated by vertical lines and italic letters.

TABLE 6

Transition energies (eV) in azulene; 0_0^0 energies are given except where otherwise noted

Present work	Absorption	Assignment[a]
1.77	1.769[b]	^1L_b
2.83 (band max.)		Triplet $\pi\pi^*$
3.55_3	3.563[c]	3s Rydberg[d] and 0_0^0 of ^1L_a
3.70_5	3.701[e]	^1L_a
4.22	4.236[f]	^1B_b
4.70 (band max.)	4.635 (0_0^0)	^1B_a

[a]For assignments and summary of previous work see refs. 211, 212.
[b]Ref. 208.
[c]Ref. 207; average of feature "2".
[d]Tentative assignment, could also be a triplet valence state.
[e]Ref. 207, average of features "3" and "5".
[f]Ref. 207, feature "13".

TABLE 7

Electron attachment energies (eV) of azulene

Band	Experiment[a]	Theory[b]	Assignment[c]
a	0.3	0.6	π_2^*
b	1.6	2.3	2p, 1h
c	2.4	2.3	(π_5^{-1}, π_1^2)
d	2.7	2.6	2p, 1h+π_3^*
e	3.3	3.3	π_4^*+2p, 1h
f	3.9	3.7	π_4^*+2p, 1h
g	4.6	4.2	π_5^*+2p, 1h
h	5.3		

[a]Resonance *a* estimated from threshold energy-loss spectrum; other resonances from ETS.
[b]Calculated (PPP-CI) transition energies minus the estimated electron affinity of 0.3 eV (see text).
[c]Dominant configurations from the PPP-CI calculation.

Wentworth et al. [221] measured electron-capture coefficients in an electron-capture detector of a gas chromatograph and obtained the electron affinity of +0.59 eV for azulene. In the same work, however, an electron affinity of +0.15 eV was reported for naphthalene, which has been found to have the electron affinity of −0.16 eV by the ETS techniques (Section 8.). It will be assumed here that the same systematic error occurs in all the electron affinity values obtained by Wentworth et al. [221], and that ETS compatible values can be obtained by adding a correction of −0.29 eV to their values. This leads to an estimate of +0.3 eV for the electron affinity of azulene. Grimsrud et al. [222] measured charge-transfer equilibria in a high pressure mass spectrometer and obtained the value of +0.69 eV for the electron affinity of azulene. However, the list of electron affinities obtained by these authors does not contain a compound which could be directly compared with the results of ET spectroscopy. The theoretical values given in Table 7 were therefore obtained by subtracting 0.3 eV from the calculated transition energies. Using an uncorrected value of 0.6–0.7 eV for the electron affinity would not change the conclusions drawn from the qualitative comparison of the theoretical results and experimental attachment energies.

In assigning the calculated values to the observed resonances, resonance *c* has been assumed to contain a large contribution from the (π_5, π_1^{*2}) configuration, because this assignment makes S_1 and T_1 the parent states of this resonance, explaining its striking decay into the S_1 (and perhaps T_1) states near threshold.

The last column of Table 7 indicates that configuration mixing in the azulene anion is even more pronounced than in the naphthalene anion [22, 23];

it is involved in all states with the exception of the ground and first excited states. This effect is caused by the unusually large gap between the π_2^* and the π_3^* orbitals.

11. NORBORNADIENE

11.1. Electronic structure of neutral norbornadiene

Electron energy-loss spectra have been reported by Frueholz et al. [223] and by Doering and McDiarmid [224]. Frueholz et al. [223] detected two triplet states in the 3–4.5 eV region, although the resolution and signal-to-noise ratio did not suffice to resolve vibrational structure. Doering and McDiarmid [224] conducted an extensive study of the angle and energy dependence of the relative intensities of many singlet–singlet transitions in the 4.5–9 eV range and were able to assign four valence and nine Rydberg transitions.

Photoelectron [225, 226] and electron transmission studies revealed that the close proximity of the two $\rangle C{=}C\langle$ bonds causes the through-space interaction to dominate over the through-bond interaction for both the occupied π and unoccupied π^* orbitals in norbornadiene. Both π and π^* orbitals thus have the natural ordering, in-phase combination below the out-of-phase combination. A qualitative diagram of the π and π^* orbitals, together with the symbols used to designate them in this section, is given in Fig. 63.

The energy loss spectra are displayed in Fig. 64 and the transition energies are summarized in Table 8. Doering and McDiarmid [224] have already pointed to the peculiar fact that the relative positions of the valence singlet bands S_1, S_2 and S_3 are essentially equal to the differences of the corresponding orbital energies, indicating a small or constant role of electron rearrangement. The same qualitative statement can be made of the triplet energies T_1, T_2 and T_3, observed at low residual energies.

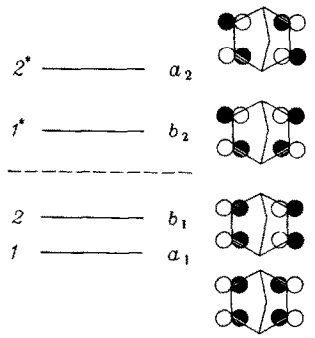

Fig. 63. Qualitative diagram of the energies of the occupied and unoccupied π orbitals in norbornadiene. The occupied orbitals π_1 and π_2 are labelled 1 and 2, the unoccupied orbitals π_1^* and π_2^* are labeled 1* and 2* for brevity.

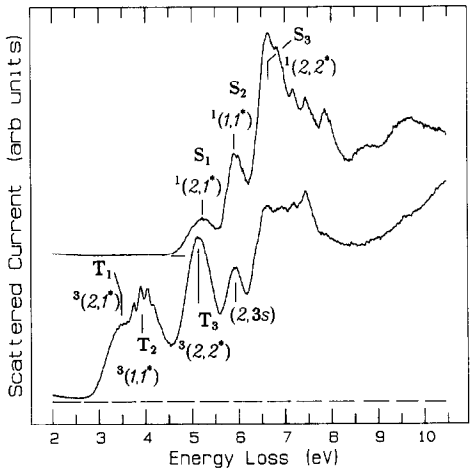

Fig. 64. Energy-loss spectra of norbornadiene. The upper spectrum has been recorded with a residual energy of 20 eV; the lower spectrum is a sum of spectra recorded at residual energies of 0.5, 1.0, 2.0, and 5.0 eV.

TABLE 8

Transition energies (eV) of norbornadiene; band maxima are given except where otherwise noted

Present work	Ref. 224	Assignment
2.88 (onset)	—	$T_1{}^3A_2\,{}^3(2,1^*)$
3.47 (max.)	—	
3.76 ($O_0{}^\circ$)[a]	—	$T_2{}^3B_2\,{}^3(1,1^*)$
5.15	—	$T_3{}^3B_2\,{}^3(2,2^*)$
5.23	5.25	$S_1{}^1A_2\,{}^1(2,1^*)$
5.92[b]	5.95	$S_2{}^1B_2\,{}^1(1,1^*)$ and $(2,3s)$ at low E_r
6.35[c]	6.38[d]	$(2,3p)$
6.65	6.65	$S_3{}^1B_2\,{}^1(2,2^*)$
6.84	6.85	$(1,3s)$
7.18	7.18	$(2,3d)$
7.44	7.45	$(2,4s)$
7.86	7.87	$(2,4d)$
8.7		
9.6		

[a]Further vibrational peaks at 3.90, 4.05, and 4.19 eV; vibrational spacing 0.145 eV, $1170 \pm 80\ cm^{-1}$.
[b]Weak vibrational peaks observed at 5.91 and 6.00 eV, at $E_r = 20$ eV.
[c]Weak shoulder at low E_r.
[d]Ref. 227.

Doering and McDiarmid [224] propose that the fourth valence excited state, $^1(1,2^*)$, causes a diffuse background around 7.5 eV. This conclusion is indirectly supported by the present spectra with low E_r; an additional diffuse background is observed around $\Delta E = 6$ eV, which could be the fourth triplet state $T_4\,^3(1,2^*)$.

A striking feature of the energy-loss spectra of Fig. 64 is the absence of distinct vibrational structure in all bands with the exception of T_2 and S_2. An interesting speculative explanation of this feature may be based on the orbital picture of Fig. 63. The orbitals 1 and 1* are bonding, 2 and 2* antibonding with respect to the mutual interaction of the two >C=C< moieties. With respect to this interaction the electron is promoted from an antibonding to a bonding orbital in the (2,1*) (T_1 and S_1) excited states. This promotion could thus lead to a substantial change in the equilibrium distance of the double bonds, resulting in significant activity of the corresponding low frequency bending vibration, obscuring the vibrational structure. The (1,1*) (bonding→bonding) promotion in the T_2 and S_2 excited states, on the other hand, could lead to a much smaller change of the equilibrium distance of the double bonds, a much lesser activity of the bending vibration, and an unobscured appearance of the strongly active C=C stretch vibration.

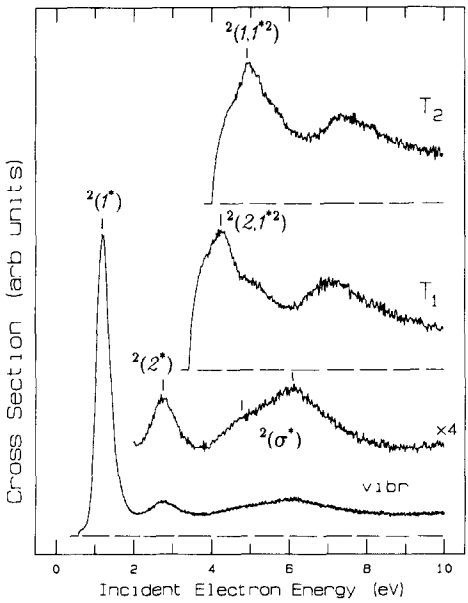

Fig. 65. Energy dependence spectra of norbornadiene. The lowest curve is recorded at $\Delta E = 0.55$ eV, that is approximately at the combination band of one quantum of C–H and one quantum of C=C stretch vibrations. The upper curves are recorded at $\Delta E = 3.4$ eV and $\Delta E = 4.0$ eV, at the approximate band centers of the T_1 and T_2 states.

11.2. Norbornadiene negative ion

The transmission spectrum of norbornadiene has been reported by Jordan et al. [228]. The energy dependence of vibrational excitation and the excitation of the first and second triplet state are shown in Fig. 65, the observed attachment energies are given in Table 9. The two shape resonances observed in ETS by Jordan et al. [228], $^2(1^*)\,(B_2)$ and $^2(2^*)\,(A_2)$, give rise to two peaks

TABLE 9

Attachment energies (eV) in norbornadiene

Present work	Channel	ETS [228]	Assignment
1.19	Vibr.	1.04	$^2(1^*)\,^2B_2$
2.75	Vibr.	2.56	$^2(2^*)\,^2A_2$
4.75	Vibr.		σ^*
6.1	Vibr.		σ^*
4.25	T_1		$^2(2,1^{*2})$ + other $^2B_1$
4.95	T_2		$^2(1,1^{*2})$ + other $^2A_1$
7.05	T_1		2p, 1h
7.35	T_2		2p, 1h

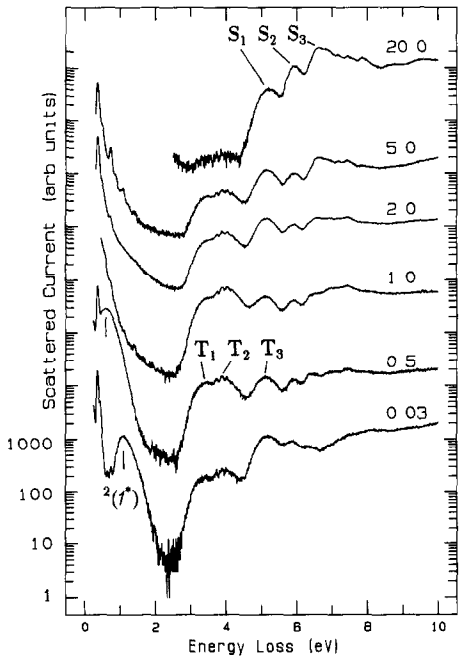

Fig. 66. Energy-loss spectra of norbornadiene, recorded at the residual energies indicated on the right side of the figure. The spectra are displayed on a semilogarithmic scale, offset by arbitrary amounts along the ordinate.

in the vibrational cross section. The lower intensity of the second of these two peaks is probably caused by the shorter lifetime of the higher-lying resonance, resulting in a smaller perturbation of the nuclear wavefunction. Two broader bands in the vibrational cross section, at 4.75 and 6.1 eV, are assigned to σ^* shape resonances.

Both electronic excitation cross sections of Fig. 65 exhibit a strong band about 1 eV above threshold. The most obvious assignment of these peaks are the two lowest configurations with the T_1 and T_2 states as parents, that is to $^2(2,1^{*2})\,(B_1)$ and $^2(1,1^{*2})\,(A_1)$, respectively. It must be pointed out, however, that T_1 is also the parent of the higher lying $^2(2,1^*2^*)\,(A_1)$ configuration, and T_2 of $^2(1,1^*2^*)\,(B_1)$. Interaction of configurations of the same symmetry will result in four states, each having to some degree both T_1 and T_2 as parents. The two peaks at 4.25 and 4.95 eV in the T_1 and T_2 excitation, respectively, are thus assigned to the core excited shape resonances dominated by the $^2(2,1^{*2})\,(B_1)$ and $^2(1,1^{*2})\,(A_1)$ configurations.

Figure 66 shows a series of energy-loss spectra recorded at various residual energies. The first shape resonance $^1(1^*)$ is seen to lead to an intense unspecific vibrational excitation. A progression of four vibrational levels with a spacing of 0.37_2 eV (3000 cm^{-1}) is observed with $E_r = 5$ eV, where the vibrational excitation proceeds via the σ^* resonances.

12. ACETALDEHYDE

Several electron-impact investigations of acetaldehyde have been reported in the literature. The electron energy loss spectrum of acetaldehyde at 2° and 100 eV incident energy was reported by Tam and Brion [229], who observed several singlet Rydberg states. An SF_6^- -scavenger spectrum revealing valence triplet states has been reported by Naff et al. [230]. A transmission spectrum of Van Veen et al. [231] and Jordan and Burrow [21] revealed a π^* resonance at 1.26 eV and several sharp structures in the 6–7 eV range. Trapped electron spectra [231] also revealed the $^3(n,\pi^*)$, the $^3(\pi,\pi^*)$, and the $^3(n,3s)$ transitions. Energy-loss spectra in the valence region have recently been reported by Walzl et al. [232]. A low resolution dissociative attachment experiment has been reported by Dorman [113]. Vibrational excitation in the π^* resonance region has recently been reported by Benoit et al. [234, 235]. This section presents a summary of and extends three previous publications [111, 172, 236].

12.1. Electronic structure of neutral acetaldehyde

Figure 67 shows global energy-loss spectra recorded with several residual energies. Pure vibrational excitation is found in the energy-loss region below 3 eV. The sharp peak at $\Delta E = 0.21$ eV, appearing at all residual energies, stems from the direct (i.e., nonresonant) excitation of the IR-active CO stretch vi-

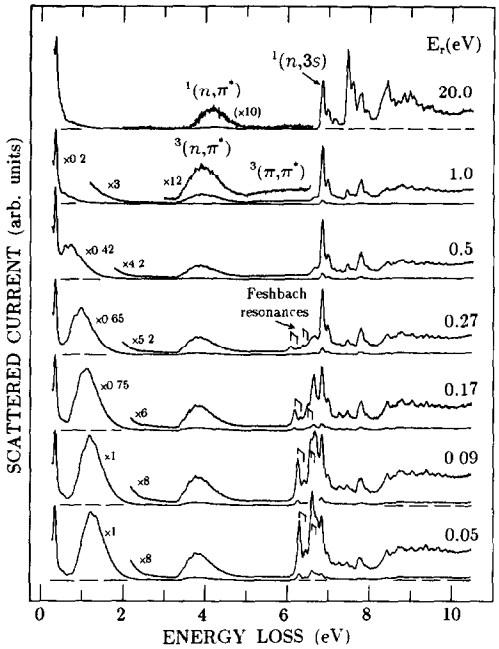

Fig. 67. Global energy-loss spectra in acetaldehyde. The true relative intensities of the spectra (except $E_r = 20$ eV) are indicated by the multiplication factors.

bration ν_4. The π^* resonance at 1.26 eV causes excitation of a quasi-continuum of high vibrational levels at low residual energies, resulting in a broad band in the energy-loss spectra, which appears at the incident energy of the resonance and consequently shifts to the left on the energy-loss scale as the residual energy is increased. Closer examination reveals that the weak fine structure on the band also shifts to the left, and thus is not due to individual vibrational levels of neutral acetaldehyde, but is caused by a boomerang-type vibrational motion of the temporary negative ion. This structure is also visible in the ET spectrum of Van Veen et al. [231], and in the vibrational excitation functions shown in the next section and those reported by Benoit et al. [234, 235]. The unspecific resonant vibrational excitation (see Section 15), that is the excitation of a quasi-continuum of vibrational levels near threshold without selectivity for any particular vibrational mode, is thus also encountered in acetaldehyde. The true relative intensities given in Fig. 67 indicate that the intensity of the electrons ejected through the unspecific vibrational excitation is approximately constant for all residual energies in the range $E_r = 0.05$–0.5 eV. Acetaldehyde thus represents in this respect an intermediate case between the small molecule N_2, where vibrational excitation is very weak at threshold, and the large molecule *p*-benzoquinone, where a peak at threshold was observed (ref. 196 and Section 15).

In the 3–6 eV energy-loss range three valence electronic excitations are encountered. The region above 6.5 eV is dominated by Rydberg transitions. The several sharp peaks in the 6–6.8 eV region, which shift to the left as the residual energy is increased, are due to Feshbach resonances. The spectra in Fig. 67 demonstrate clearly that threshold energy-loss spectra (obtained for example by the SF_6^- scavenger technique or the trapped electron method without variation of the well depth) of organic molecules are very difficult to interpret without the knowledge of the dependence on residual energy, because both the excited states of the neutral target and resonances cause bands in the spectrum which cannot easily be differentiated. It appears for example, that the band due to the lowest Feshbach resonance at 6.34 eV has been mistakenly interpreted as the $^3(\pi,\pi^*)$ state in the trapped electron spectrum of ref. 231.

Figure 68 shows the valence and low Rydberg excitation range in more detail. The $^3(n,\pi^*)$ band, excited at low residual energies, has the first vibrational feature at 3.51 eV. The higher onset of the first band in the spectrum with $E_r = 20$ eV indicates that the $^1(n,\pi^*)$ state is excited in this spectrum. The broad band around 6 eV is assigned as the triplet (π,π^*) state. The corresponding singlet state is probably located in the 8–9 eV region (HAM calculation: 9.0 eV [237]), interacts strongly with the Rydberg states and cannot be identified in the spectrum. The assignment of the singlet Rydberg states has been discussed by Robin [210] and Lucazeau and Sandorfy [238]. The two additional sharp bands appearing at low residual energies at 6.65 eV and 7.25 eV are assigned to triplet Rydberg states. This assignment is supported by the

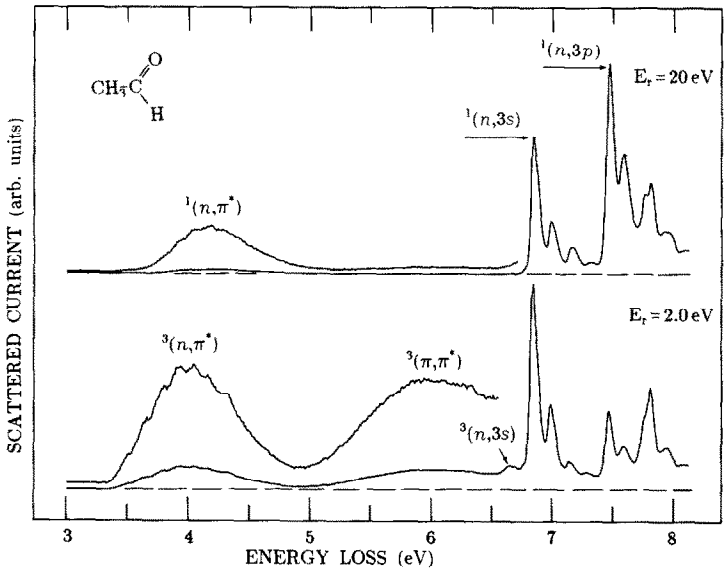

Fig. 68. Energy-loss spectra of acetaldehyde in the valence and low Rydberg range.

TABLE 10

Transition energies (eV) of acetaldehyde

Energy	Vibr. spacing	Assignment	HAM[a]
3.38 (onset) 4.0 (centre)	0.12	$^3(n,\pi^*)$	4.15
3.63 (onset) 4.18 (centre)	0.12	$^1(n,\pi^*)$	4.64
5.97 (maximum)	—	$^3(\pi,\pi^*)$	6.04
6.65 (0_0^0)	—	$^3(n,3s)$	
6.82 (0_0^0)	0.143	$^1(n,3s)$	
7.25 (0_0^0)	—	$^3(n,3p)$	
7.45 (0_0^0)	0.114	$^1(n,3p)$	

[a]Results of HAM calculation [237].

similar singlet–triplet splittings reported for formaldehyde [239]. The energies of the excited states observed below 7.5 eV are summarized in Table 10.

12.2. Acetaldehyde negative ion

12.2.1. Energy dependence spectra

The energy dependence of several vibrational and electronic excitations in acetaldehyde is shown in Fig. 69. Two resonances are visible in the vibrational excitation. The resonance at 1.2 eV has already been reported in ETS [21, 231], and assigned to a $^2(\pi^*)$ state with capture of the incoming electron into the $\pi^*(a'')$ orbital. The second resonance, the broad feature with a maximum at 6.8 eV, is slightly more pronounced in the C–H stretch excitation than in the C=O stretch excitation, and by analogy with similar results in other molecules it is assigned to one or several overlapping σ^* resonances.

The $^3(\pi,\pi^*)$ excitation exhibits a broad band at 8.1 eV. It is assigned to the $^2(\pi,\pi^{*2})$ core excited resonance on the grounds of the efficient decay into its parent $^3(\pi,\pi^*)$ state and absence in the ET spectrum, indicating a low attachment cross section. A sharp peak near threshold is caused by the $^2(3s^2)$ Feshbach resonance.

The excitation function of the $^3(n,\pi^*)$ state is qualitatively different from the $^3(\pi,\pi^*)$ excitation function, consisting essentially of a step function. This shape is surprising in two respects. First, in analogy with the $^2(\pi,\pi^{*2})$ resonance, a $^2(n,\pi^{*2})$ resonance could be expected (predicted to lie at 5.4 eV by the HAM calculation of Lindholm [237]), decaying into its $^3(n,\pi^*)$ parent state, and causing a peak in the $^3(n,\pi^*)$ excitation function. The absence of a distinct peak could be caused by the $^2(n,\pi^{*2})$ resonance occurring below its parent state, being very broad, or having a very low attachment cross section and not affecting significantly the excitation of the $^3(n,\pi^*)$ state. A second feature of the $^3(n,\pi^*)$ excitation function is the large value of the cross section at thresh-

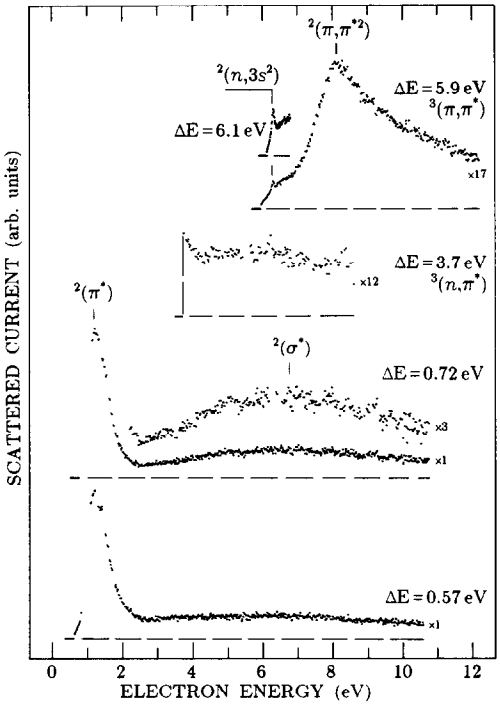

Fig. 69. Energy dependence spectra in acetaldehyde, recorded at the energy-losses indicated on the right. $\Delta E = 0.57$ eV corresponds mainly to the excitation of the combination of the C–H and C=O stretch frequencies, $\Delta E = 0.72$ eV to the excitation of two quanta of the C–H stretch. The true relative intensities of the individual curves are indicated by the multiplication factors.

old and its step-like onset. The step could be explained by (dipole-bound) resonances near the excitation threshold.

Figure 70 shows the excitation functions of the singlet and triplet (n,3s) Rydberg states. The singlet cross section has a step-wise onset and rises slowly and approximately linearly with increasing energy above threshold. The triplet cross section has a peak at threshold, another peak 0.12 eV above threshold, and then decreases linearly with increasing energy. The peak 0.12 eV above threshold, at an incident energy of 6.76 eV, is due to the $\Delta v = -1$ vibrational autodetachment of the $v = 1$ vibrational level of the F_2 Feshbach resonance. The threshold peak could be caused by the tail of the $v = 0$ level of the F_2 resonance, situated only 10–20 meV below.

It is interesting to note that the cross sections in the C=O group-containing molecule acetaldehyde qualitatively resemble the corresponding cross sections in CO, discussed in Section 6. The cross sections for the $^3(\sigma,\pi^*)$ state in CO and the $^3(n,\pi^*)$ state in CH_3CHO are both essentially step functions. The cross sections of the $^3(\pi,\pi^*)$ states in both molecules are small at threshold, increase gradually, and show a broad resonance feature (probably the $^2(\pi,\pi^{*2})$ core-

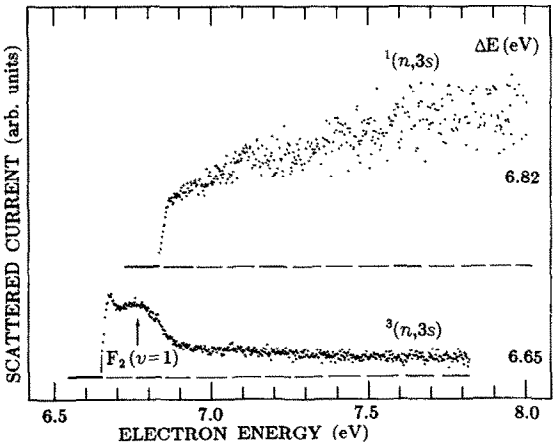

Fig. 70. Energy dependence of the excitation of the two lowest Rydberg states in acetaldehyde. Both curves are on the same vertical scale. The peak labelled by an arrow is due to vibrational autodetachment of the $v=1$ level of the F_2 (n, $3s3p$) Feshbach resonance.

excited shape resonance) about 1 eV above threshold. Qualitative similarity may also be discerned for the $^3(3s)$ and $^1(3s)$ states in both molecules. This suggests that the theoretical treatments of the electron scattering in CO (for example by Huo et al. [158]) may also serve as a model case for the understanding of scattering in carbonyl compounds.

The near threshold energy-loss spectra in Fig. 71 indicate that the Feshbach resonances in acetaldehyde decay preferentially by the ejection of a very slow electron, as manifested by the fact that the Feshbach resonances dominate the spectrum at threshold, but rapidly decrease in intensity with increasing residual energy and become barely visible at $E_r=0.5$ eV. The final state is consequently at nearly the same energy as the resonance in this decay channel and the process will be called "resonant autodetachment", by analogy with the resonant autoionization reported in the threshold photoelectron spectra of organic molecules [173–175]. The final states are probably high vibrational levels of the underlying broad $^3(\pi,\pi^*)$ valence state, but could also be very high vibrational states of the lower lying electronic states, including the electronic ground state.

Two Feshbach resonances may be discerned in acetaldehyde, both with vibrational structure, and are labelled F_1 and F_2 in Fig. 71. Their energies relative to the low-lying Rydberg states [142] identify them as the $^2(n,3s^2)$ and the $^2(n,3s3p)$ states, the parent state in both cases being the lowest Rydberg state $^3(n,3s)$. For each resonance one excited vibrational level is observed. The study of dissociative attachment of partially and fully deuterated acetaldehyde identified the vibrations excited as ν_7 (CH_3 def. and C–C stretch) in the resonance F_1 and ν_6 (CCH bend) in the resonance F_2 [236]. Qualitative potential curves

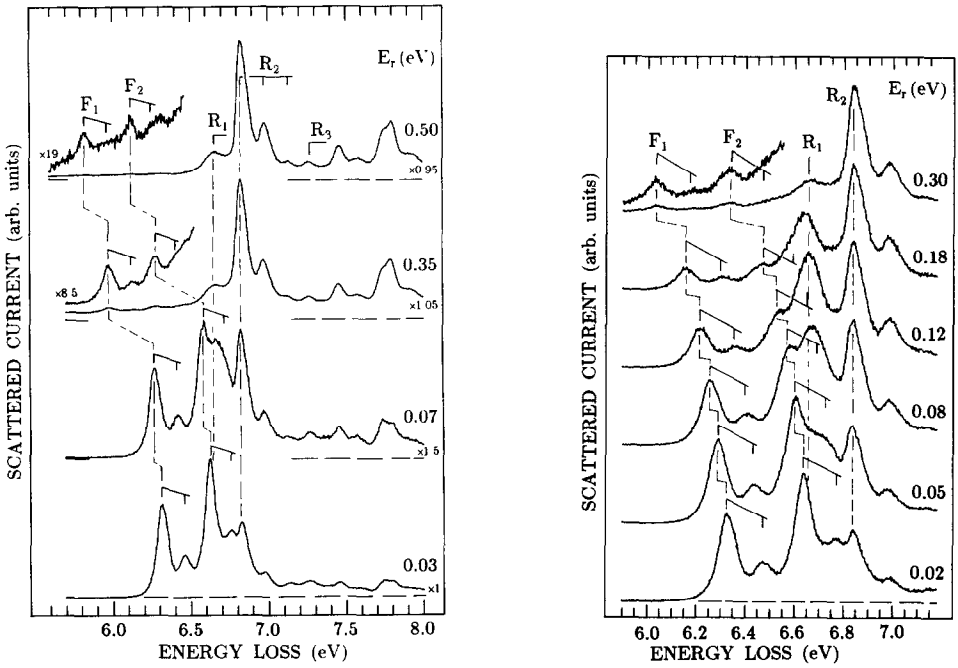

Fig. 71. Near threshold energy-loss spectra illustrating the resonant autodetachment of the Feshbach resonances F_1 (n,3s^2) and F_2(n,3s3p). R_1 and R_2 are the ^{3}(n,3s) and ^{1}(n,3s) Rydberg states. The curves are approximately on the same vertical scale in each part of the figure. The intensity of the signal due to decay of the Feshbach resonances decreases rapidly as the residual energy is increased. The R_1 ^{3}(n,3s) has an anomalously large intensity when observed at residual energies where it can be populated by vibrational autodetachment of the F_1 (v=1) Feshbach resonance level.

illustrating the Feshbach resonances and their parent Rydberg states are shown in Fig. 72 and the experimentally determined energies are given in Table 11.

Interestingly, the v=1 level of the F_2 resonance, at 6.76 eV, lies above the v=0 level of the ^{3}(n,3s^2) parent state at 6.65 eV. This opens up the possibility of a $\Delta v = -1$ vibrational autodetachment into the parent electronic state. This decay channel actually occurs and causes the 6.76 eV peak in the ^{3}(n,3s) excitation in Fig. 70 and the anomalously high intensity of the ^{3}(n,3s) Rydberg state in the E_r=0.05–0.18 eV spectra in Fig. 71.

12.2.2. Dissociative attachment spectra

High resolution spectra of the negative-ion yield from acetaldehyde reveal a structured band in the 6.3–7 eV region (shown in comparison with the threshold electron yield in Fig. 73). Using the mass filter this band is found to be due to an m/e=15 anion, that is to CH_3^-. A comparison of signal intensities with O^-/CO_2 for a given Penning gauge reading indicates that the cross section is

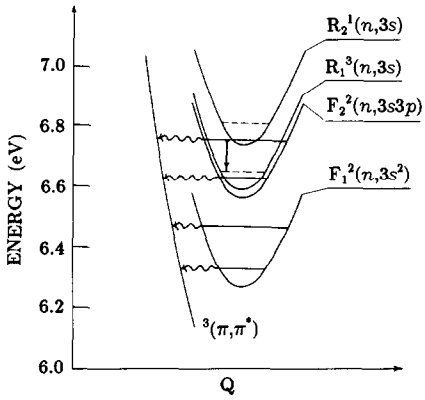

Fig. 72. Schematic potential curves of the low lying Rydberg states and Feshbach resonances in acetaldehyde. The horizontal wavy lines indicate the resonant autodetachment decay channel. (The label $^3(\pi,\pi^*)$ indicates only one of the several possible final channels.) The vertical arrow indicates vibrational autodetachment decay.

TABLE 11

Attachment energies in acetaldehyde (energies of band maxima in eV)

Energy	Channel[a]	Assignment		HAM[b]
1.2	Vibr., ETS[c]	$^2(\pi^*)$	shape	1.21
6.34[d]	TE, DA, ETS	$^2(n,3s^2)$	Feshbach	
6.64[e]	TE, DA, ETS	$^2(n,3s3p)$	Feshbach	
6.8	Vibr.	$^2(\sigma^*)$	shape	
8.1	$^3(\pi,\pi^*)$ excit.	$^2(\pi,\pi^{*2})$	core excited shape	8.58

[a]Energy dependence of vibrational excitation (vibr.), threshold electron spectra (TE), dissociative attachment (DA), electron transmission spectrum (ETS).
[b]Results of HAM calculation [237].
[c]Ref. 21.
[d]Vibrational spacing 0.138 ± 0.01 eV (ν_7).
[e]Vibrational spacing 0.122 ± 0.01 eV (ν_6).

of the order of 10^{-19} cm^2. The measurement of the ion kinetic energy distributions reveal that within our resolution all the CH_3^- ions are formed with zero kinetic energy. The shape and energy of the spectrum indicate that the CH_3^- ions are formed by decay of the F_1 and F_2 Feshbach resonances discussed in the preceding section.

In the dissociative attachment spectra of the partially deuterated molecule CH_3CDO we observe exclusively the $m/e = 15$ CH_3^- fragment [236]. The fragmentation of the anion is thus not accompanied by "scrambling" of the hydrogen atoms, contrary to the situation encountered in fragmentation of certain

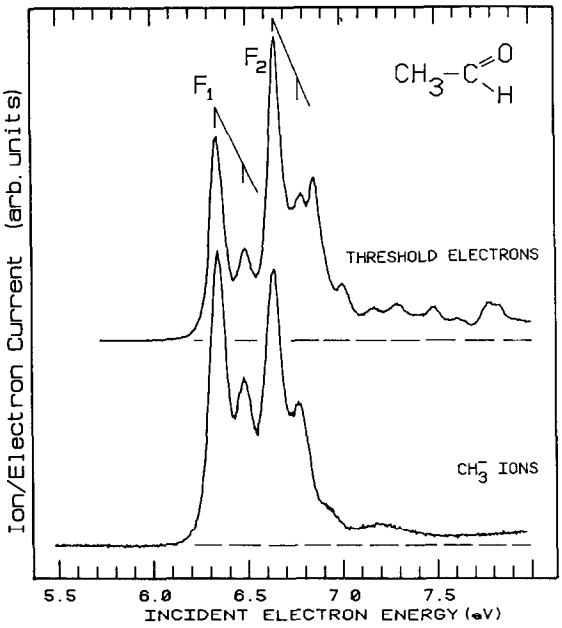

Fig. 73. Yields of CH_3^- ions and near-threshold ($E_r = 0.03$ eV) electrons. Both dissociation and resonant autodetachment are seen to be two competing decay channels of the same resonances F_1 and F_2.

states of the acetaldehyde cation [240, 241]. The fully deuterated molecule CD_3CDO yielded the $m/e = 18$ (CD_3^-) fragment, albeit with a weaker intensity compared to the CH_3^-/CH_3CHO signal.

We ascribe the absence of "hydrogen scrambling" in the dissociation of the negative ion to its short lifetime, caused by the competing fast autodetachment channel. The short lifetime does not leave time for the relatively large nuclear rearrangement such as hydrogen scrambling. (Scrambling has, however, recently been observed in OH^- formation in dissociative attachment on CH_3OH [242].)

The CH_3–CHO dissociation energy may be calculated from standard thermochemical data [243] to be 3.49 eV. The electron affinity of CH_3 was determined to be 0.08 eV by Ellison et al. [244]. The threshold for CH_3^- formation is therefore 3.41 eV, which means that about 3 eV of excess energy are released in the dissociation process. Since this energy does not appear as kinetic energy, it must be deposited as internal energy of the fragments. This may happen in the form of vibrational energy or the electronic excitation of the HCO fragment. (The $^2A''$ first excited state of HCO, near 2 eV [245], is energetically accessible.) Time-resolved energy-loss spectra [236] indicated that vibrationally autodetaching CH_3^- ions are also formed slowly (≈ 0.1 μs) in dissociative attachment to acetaldehyde.

Formation of H^- and O^- ions is also observed [25]. At higher sample pressure the CH_3CO^- ion with the mass 43 is observed at the energy of the Feshbach resonances F_1 and F_2. The pressure dependence indicates, however, that this ion is formed in a secondary reaction (proton abstraction) of the CH_3^- ion with acetaldehyde.

13. TROPONE

Tropone (2,4,6-cycloheptatriene-1-one) contains a planar seven-membered ring and its spectroscopy and electronic structure have been the subject of numerous investigations, aiming at, among others, determining its "aromatic character".

Veltin et al. [246] have measured the polarization of the absorption bands in hexane solvent using dichroism induced by an external electrostatic field and have interpreted the results with the help of simplified PPP-type calculations. The broad asymmetrical absorption band between 3.4 and 5.0 eV has been found to consist of a perpendicular and a parallel polarized transitions which have been assigned to two $^1(\pi,\pi^*)$ states. The $^1(n,\pi^*)$ transition has been assumed to be weak and completely buried under the two $^1(\pi,\pi^*)$ transitions. These conclusions have been further supported by the analysis of the spectra of a vinylogous tropone derivative by Hagen et al. [247]. Hosoya and Nagakura [248] have proposed, on the other hand, that the 4.2 eV band consists of the $^1(n,\pi^*)$ and a single $^1(\pi,\pi^*)$ transition. Kuroda and Kunii [249] have calculated the first two $^1(\pi,\pi^*)$ transitions at 3.73 and 4.2 eV and have thus supported the original assignment of Veltin et al. [246]. Yamaguchi et al. [250] have performed PPP-type calculations taking into account bond alternation and including the n-electrons on the oxygen atom, and have supported the assignment of ref. 246 of two $^1(\pi,\pi^*)$ transitions at 3.63 and 4.0 eV. (A third transition has been calculated at 4.78 eV.) The latter authors have also calculated the energies of the $^3(n,\pi^*)$, $^1(n,\pi^*)$ (at 4.74 eV), and $^3(\pi,\pi^*)$ transitions, and have presented a gas phase absorption spectrum. The assignment of ref. 246 has been further supported by the calculations of Yoshida and Kobayashi [251], and by the INDO/S-CI calculations of Buemi et al. [252]. The latter authors placed the $^1(n,\pi^*)$ transition at 4.88 eV.

The photoelectron spectrum (for example [253]) revealed closely lying $\pi(b_1)$ and $n(b_2)$ states at 8.89 and 9.25 eV, followed by a $\pi(a_2)$ band at 10.64 eV.

The present energy-loss spectra are displayed in Fig. 74. The spectrum recorded at $E_r = 20$ eV closely resembles the absorption spectrum. The spectrum recorded with $E_r = 1.0$ eV bears only little resemblance to the $E_r = 20$ eV spectrum, indicating the presence of several singlet–triplet transitions. The asymmetric appearance of the first triplet band with a maximum at 2.51 eV strikingly resembles the first singlet band at 4.7 eV, suggesting that the two bands correspond to the same pair of π,π^* transitions with similar singlet–triplet

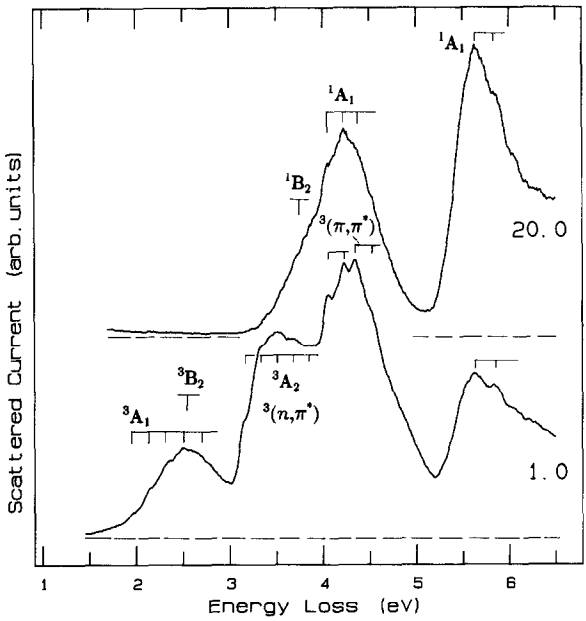

Fig. 74. Energy-loss spectra of tropone with proposed assignments.

splittings. This conclusion is supported by the calculated triplet energies of Yamaguchi et al. [250].

The energy-loss spectra of acetaldehyde (Figs. 67 and 68) show that whereas $^1(n,\pi^*)$ is weak in the $E_r=20$ eV spectrum, $^3(n,\pi^*)$ has an intensity comparable to or higher than the $^3(\pi,\pi^*)$ transition at low E_r. One of the two bands at 3.51 and 4.35 eV in the $E_r=1.0$ eV spectrum of tropone (Fig. 75) thus may well correspond to the $^3(n,\pi^*)$ transition. The structureless energy-dependence curve of the 3.36 eV transition (Fig. 76), somewhat closer in appearance to the also structureless energy dependence of the $^3(n,\pi^*)$ transition in acetaldehyde, renders the assignment of the 3.5 eV band to $^3(n,\pi^*)$ preferable. This assignment is consistent with the work of Yamaguchi et al. [250], who calculated the energy of the $^3(n,\pi^*)$ transition to be between 3.49 and 4.11 eV, depending on the value of the bond alternation parameter k. This assignment also places the $^3(n,\pi^*)$ energy of tropone close to the $^3(n,\pi^*)$ energy of the related *p*-benzoquinone [52].

The vibrational structure in the 4.05–4.5 eV region is more pronounced and more complex in the $E_r=1.0$ eV spectrum than in the $E_r=20$ eV spectrum, indicating the presence of additional transitions. The first two of these features, at 4.06 and 4.22_5 eV, coincide within experimental error with the vibrational features observed with $E_r=20$ eV, and, although they differ in being more distinct, could stem from the same $^1A_1{}^1(\pi,\pi^*)$ state. The following two features, at 4.34_5 and 4.52 eV, do not have a counterpart in the $E_r=20$ eV

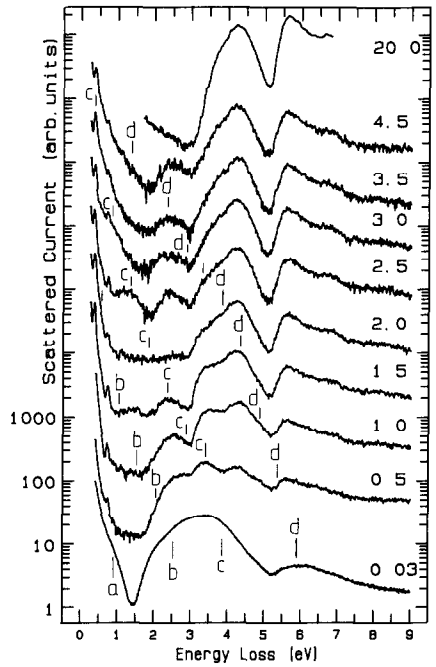

Fig. 75. Energy-loss spectra of tropone, recorded at the constant residual energies indicated at right. The spectra are shown on a semilogarithmic scale and are offset by arbitrary amounts along the ordinate. Positions of resonances are indicated by vertical lines and letters.

spectrum and probably correspond to an additional dipole and/or spin forbidden transition. Possible assignments include the $^1B_2{}^1(\pi,\pi^*)$ state calculated at 4.78 eV (and with small oscillator strength) by Yamaguchi et al. [250] and the $^3A_1{}^3(\pi,\pi^*)$ state whose singlet counterpart is observed at 5.63 eV.

Figure 75 shows a series of energy-loss spectra recorded at several residual energies. The threshold spectrum is strikingly dissimilar from the remaining spectra. Its shape is determined less by the electronically excited states, and more by the unspecific vibrational (and probably electronic) excitation by the four resonances *a*–*d*. The excited state at $\Delta E = 3.5$ eV is the strongest electronic band at $E_r = 0.5$ eV, but its intensity relative to the $\Delta E = 4.3$ band diminishes steadily with increasing E_r. In this respect the $\Delta E = 3.5$ eV resembles the $^3(n,\pi^*)$ state of acetaldehyde, supporting indirectly the assignment in Table 12.

Figure 76 shows several energy dependence spectra. Three resonances *b*, *c*, and *d* can be discerned in the vibrational cross section at 2.55, 3.85, and 5.85 eV. The threshold peak in this cross section is probably due to the resonance *a*, which is seen as a shoulder near 0.9 eV in the $E_r = 0.03$ eV spectrum of Fig. 75. The resonances *b* and *c* are probably localized to some degree on the heptatriene part of the tropone molecule and closely related to the two resonances

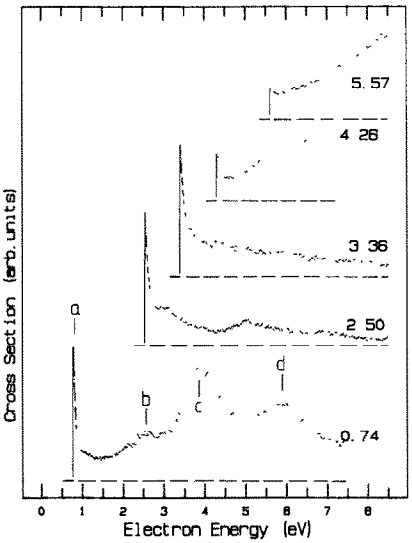

Fig. 76. Excitation functions in tropone, recorded at the energy losses indicated at right. Assuming the assignments given in Table 12 these energy-losses correspond to (from bottom to top): pure vibrational excitation (two quanta of C-H stretch); overlapping $^3A_1$ and $^3B_2{}^3(\pi,\pi^*)$ states; $^3A_2{}^3(n,\pi^*)$ state; $^1A_1{}^1(\pi,\pi^*)$ and overlapping states; $^1A_1{}^1(\pi,\pi^*)$ state.

TABLE 12

Transition energies (eV) in tropone; vibrational spacings are given in cm^{-1} ($\pm 80\ cm^{-1}$)

Origin	Band centre	Vibr. spacing	Theory[a]	Assignment
1.97_5	~2.2	1430	2.06	$^3A_1\pi,\pi^*$
—	~2.5	—	2.92	$^3B_2\pi,\pi^*$
3.155	3.51	1400	4.03	$^3A_2n,\pi^*$
—	~3.75	—	3.63	$^1B_2\pi,\pi^*$
4.05	4.23	1350	4.04	$^1A_1\pi,\pi^*$
4.34_5	4.34_5	~1400	—	$^3A_1{}^3(\pi,\pi^*)$ (?)
5.64	5.64	~1700	5.71	$^1A_1\pi,\pi^*$

[a]Ref. 250.

observed at 2.13 and 3.53 eV in hexatriene by Burrow and Jordan [254]. The resonance *a* is probably to a considerable degree located on the π^* orbital of the >C=O group and related to the $^2(\pi^*)$ resonance of acetaldehyde at 1.2 eV (preceding section). The lowest electron affinity of tropone is nearly certainly positive and the ground state of the tropone negative ion is closely related to the ground state of hexatriene anion $^2(\pi_1^*)$, because the hexatriene π_1^* orbital cannot mix with the π^* orbital of the >C=O group for symmetry reasons. The

resonance *d* could be a $^2(\sigma^*)$ shape resonance or a π resonance with both 1p and 2p, 1h character as a consequence of configuration mixing.

A second striking feature of the energy dependence spectra of Fig. 76 is the presence of intense threshold peaks in the $\Delta E = 2.5$ and $\Delta E = 3.36$ eV excitation functions. The two thresholds occur within the resonances *b* and *c*, which may be responsible for the threshold peaks. The 2.5 eV and 3.5 eV energy-loss bands cannot easily be discerned as such in the threshold spectrum of Fig. 75, however, and it is consequently impossible to exclude the possibility that the threshold peaks in the two excitation functions are due to unspecific excitation of the vibrational continuum of the electronic ground state at threshold. The threshold peak in the excitation of the $^3(n,\pi^*)$ state could also be due to a dipole-bound resonance, the $^3(n,\pi^*)$ state probably having a substantial dipole moment (because of the large average distance of the n and π^* orbitals).

14. 2,3-DIAZABICYCLO[2.2.1.]HEPT-2-ENE

2,3-Diazabicyclo[2.2.1]hept-2-ene is a rigid molecule containing a *cis*-azo group. Its photoelectron spectrum [255] revealed an n_- orbital at 8.9 eV, a π orbital at 11.5 eV and an n_+ orbital at 11.9 eV. Mirbach et al. [256] found the maximum of the first absorption band in hexane at 3.64 eV. The triplet energy has been determined by the energy transfer method to be 2.60 ± 0.043 eV [257]. The lowest triplet energy of the related azomethane has been determined to be 2.75 eV by energy-loss spectroscopy [84].

The present energy-loss spectra are shown in Fig. 77 and transmission spec-

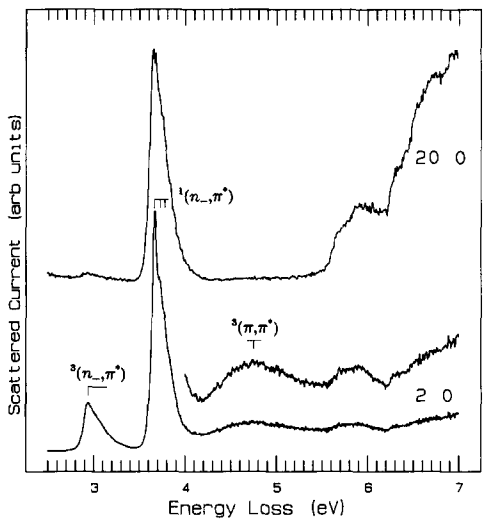

Fig. 77. Energy-loss spectra of 2,3-diazabicyclo[2.2.1]hept-2-ene.

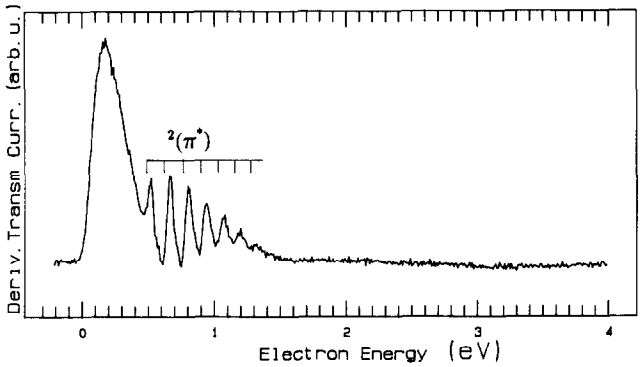

Fig. 78. Electron transmission spectrum of 2,3-diazabicyclo[2.2.1]hept-2-ene in the derivative representation.

TABLE 13

Transition energies (eV) in 2,3-diazabicyclo[2.2.1]hept-2-ene

Energy		Vibr. spacing (cm^{-1})	Assignment
Present work	Other		
2.94	2.602[a]		$^3(n_-,\pi^*)$
3.665	3.64[b]	460 ± 80	$^1(n_-,\pi^*)$
4.75			$^3(\pi,\pi^*)$
5.68			$(n_-,3s)$ Rydberg (?)

[a]Chemical method, ref. 257.
[b]Absorption in hexane, ref. 256.

trum in Fig. 78; the observed transition energies are summarized in Table 13. The energy of the $^1(n_-,\pi^*)$ transition agrees well with the solution value of ref. 256. The energy of the $^3(n_-,\pi^*)$ state lies slightly outside the error limits of the chemically determined value of Clark and Steel [257]. Chemical methods generally determine the adiabatic value of the triplet energy, that is the energy of the minimum of the triplet potential hypersurface, and differences between spectroscopically and chemically determined triplet energies may be due to the inability of the spectroscopic methods to determine the adiabatic energy when the minimum of the hypersurface lies strongly outside the Franck–Condon region. In the present case, however, the $^3(n_-,\pi^*)$ band is narrow and the 0_0^0 transition coincides with the band maximum, indicating only small changes of molecular geometry in the triplet state. The origin of the discrepancy must consequently be sought in solvent shift or inaccuracy of the chemical method.

The next band observable with $E_r = 20$ eV lies at 5.89 eV and could correspond to a Rydberg transition with a quantum defect with $\delta = 1.0$. A broad band with a maximum near 4.75 eV appears in the $E_r = 2.0$ eV and is assigned to a $^3(\pi,\pi^*)$ state.

The transmission spectrum shows a structured band with an origin at 0.49_5 eV and average vibrational spacing of 0.138 eV (1110 ± 40 cm^{-1}). The appearance of the band bears an unmistakable resemblance to the first ETS band of nitrogen (Fig. 21) and is assigned to the corresponding $^2(\pi^*)$ shape resonance. The energy of the present band is close to the attachment energy obtained by Modelli et al. [258] for the related di-tert-butyl-azomethane (0.63 eV).

The long vibrational progression observed in the ETS band indicates a strongly antibonding π^* orbital. The very narrow (n_-,π^*) bands are consequently somewhat surprising and indicate a strongly antibonding n_- orbital, much more so than for example the σ_g or σ_u orbitals in N_2. The only resolved active vibration in the $^1(n_-,\pi^*)$ band has a spacing of 460 ± 80 cm^{-1} and thus does not correspond to N=N stretch, but presumably to a C–N=N deformation vibration, indicating a nearly perfect match of the antibonding properties of the n_- and π^* orbitals with respect to the N=N bond length. The conclusion of an antibonding n_- orbital is consistent with the relatively broad n_- photoelectron band [255].

15. EXCITATION OF HIGH VIBRATIONAL LEVELS

A separate section is devoted to the excitation of high vibrational levels of the electronic ground state because many aspects common to a number of molecules have been encountered in the study of this process. The high sensitivity of the trochoidal electron spectrometer renders it particularly suitable for the study of low cross sections, which are generally encountered with the high vibrational levels.

This section concentrates on the measurement of the excitation of high vibrational levels via low-lying shape resonances in three classes of molecules. The first class are the diatomic molecules, where the measurements in H_2, N_2, and CO are presented. The second class are the large polyatomic molecules, with *p*-benzoquinone serving as a representative example. Finally the triatomic molecule CO_2 is studied since it represents an intermediate case between the diatomics with only one vibration and the polyatomics with many vibrations.

15.1. Diatomic molecules

15.1.1. Hydrogen

The shape of bands in the energy dependence of resonant vibrational excitation by electron impact is known to be a function of resonance lifetime. Res-

onances with lifetimes long compared to the vibrational period have sharp vibrational structure, a lifetime short relative to the vibrational period gives structureless bands, and intermediate lifetimes result in broad vibrational structure whose shape and spacing depend upon the channel of observation [18].

The $^2\Sigma_u$ resonance in H_2, responsible for the vibrational excitation in the low energy region, is one of the prototype cases of an extremely short lived resonance, with a lifetime comparable to the duration of the nonresonant scattering. One would thus expect no vibrational structure in the energy dependence curves. This expectation seemed confirmed by the available experimental data [139, 259].

Mündel et al. [260] and Domcke et al. [261] reported a theoretical study of vibrational excitation and dissociative attachment in H_2 employing a sophisticated treatment of the nuclear dynamics. A striking result of this study, contradicting the intuitive expectation outlined above, is a prediction of a pronounced vibrational structure in the energy dependence of the excitation of the higher vibrational levels ($v>3$). This unexpected theoretical prediction has been tested experimentally [59].

The experimental energy dependence curves are shown in Fig. 79. The shapes of the first three curves are in good agreement with the data of Ehrhardt et al. [259]. Structures observed in the curves with $v=3$ and higher confirm the theoretical predictions of Mündel et al. [260]. In agreement with the prediction the structure is barely visible in the $v=3$ curve and becomes progressively deeper with increasing values of v. Comparison of the experimental curves with

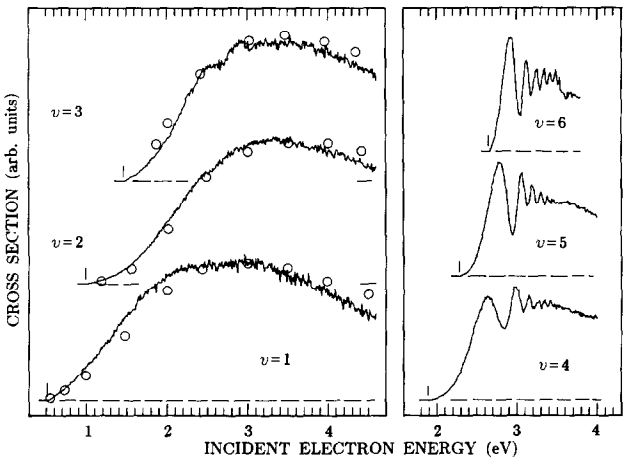

Fig. 79. Vibrational excitation cross sections in H_2. The curves are not on the same vertical scale; the relative intensities at curve maxima were given in ref. 59. The short vertical bars indicate threshold energies. The circles show the integral cross sections of Ehrhardt et al. [259], normalized to the present curves at the maximum of the $v=1$ cross section.

the theoretical results, obtained with three different approximations [260] is revealing. The adiabatic nuclei approximation does not reproduce the vibrational structure. The local-complex-potential model gives structure in the cross section; its shape is, however, qualitatively incorrect and the cross section does not have the correct magnitude. The results thus emphasize the necessity of moving beyond the local approximation for proper treatment of nuclear dynamics in H_2.

15.1.2. Nitrogen

The efficient vibrational excitation of N_2 by electron impact in the 2.3 eV region was the first observed manifestation of a resonance in electron molecule scattering [143]. Schulz [144] has found an unusual vibrational structure in the cross sections, whose explanation in terms of the "boomerang model" by Birtwistle and Herzenberg [145] has been one of the most impressive successes of the theory of resonant electron–molecule scattering.

The vibrational excitation by the 2.3 eV resonance has been further studied by Ehrhardt and Willmann [262] and the measurements have been extended up to $v=10$ by Boness and Schulz [263]. Schulz [18, 264] and Trajmar et al. [139] have extensively reviewed the existing experimental work.

The electron N_2 scattering in the 2.3 eV $^2\Pi_g$ resonance region has become a touchstone for the theories of the coupling of the electronic and nuclear motions. This is well reflected in the numerous theoretical publications on this subject, reviewed for example by Schulz [18, 264], Herzenberg [46] and Lane [48]. Recent studies [57, 265–269] prove that the subject remains of current interest.

The vibrational cross sections obtained with the present instrument are shown in Fig. 80 [148]. The curves for $v=1$ to $v=10$ excitations agree well with previous experimental data. The qualitative trends observed with increasing channel up to $v=10$ are (i) an increasing spacing between the peaks and (ii) an increasing dominance of the first peak in width and intensity. For $v=2$ to $v=10$ the first peak exhibits a "substructure" in the form of shoulders. All these essential features up to $v=10$ had been reproduced by theoretical work, for example refs. 270–272.

For $v=11$–17 the above mentioned trends are not continued. With the first peak approaching the threshold the peak spacing diminishes, the first peak becomes narrower, is no longer dominant in intensity and does not exhibit the "substructure". The discussion by Cederbaum and Domcke [273] of resonant scattering in the context of both the non-local and the local potentials had until recently been the only theoretical study applicable to N_2 in this final v range. These authors have calculated the vibrational cross sections up to $v=12$ for an exactly solvable model whose parameters were chosen to simulate the $^2\Pi_g$ resonance in N_2. An important conclusion of this study has been that whereas for the low values of v the local-complex-potential model yielded sat-

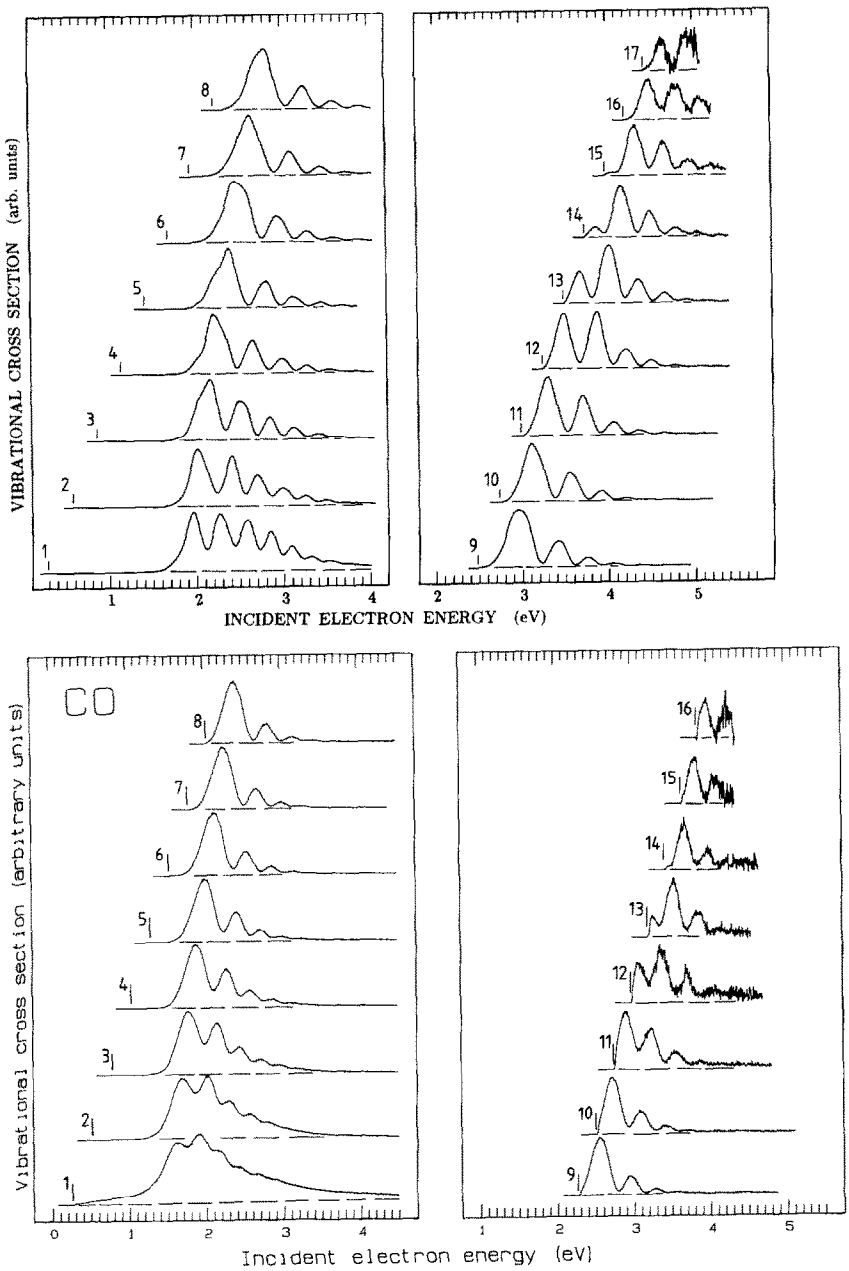

Fig. 80. Vibrational cross sections in N_2 (top) and CO (bottom). Thresholds are indicated by vertical lines. The curves are not on the same vertical scale.

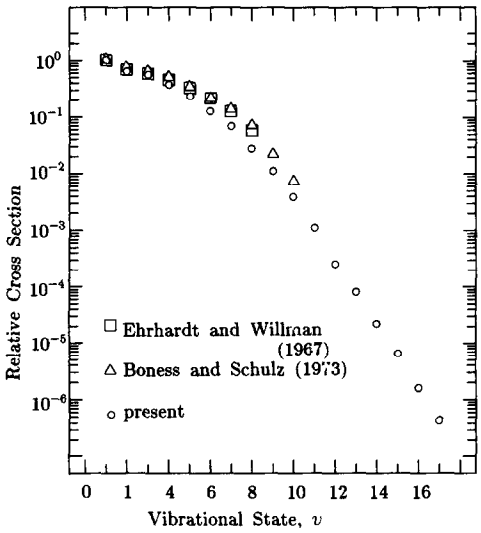

Fig. 81. Relative vibrational cross sections at curve maxima plotted against the quantum number of the final state.

isfactory results, for the higher channels a dramatic qualitative difference has been found between the results of the local and the "exact" treatment, using a non-local potential. Thus for the $v=12$ curve the local approximation has predicted a dominant first peak, whereas the non-local treatment has predicted correctly, in qualitative agreement with the present experiment, its diminishing intensity relative to the second peak.

More recently Morgan [274] has calculated the vibrational cross sections up to $v=19$ using the **R**-matrix method and her results are in excellent qualitative agreement with experiment. Other theoretical results in this final channel range have been presented by Huo et al. [268] and by Launay and Le-Dourneuf [269].

The experimental relative cross sections for N_2 at the curve maxima are shown in Fig. 81. They decrease with increasing channel number, the decrease being slow initially, but faster for the higher levels. For $v \geqslant 10$ the decrease is approximately exponential.

15.1.3. Carbon monoxide

The vibrational cross sections in CO have been measured by Schulz [144], Boness and Schulz [263], Ehrhardt et al. [259], Jung et al. [86], Tronc and Azria [275] and by Chutjian and Tanaka [276]. The present measurements aim at determining whether the shorter lifetime of the $^2\Pi$ resonance and the dipole moment of CO affect the excitation of high vibrational levels.

The cross sections obtained with the trochoidal electron spectrometer are shown in Fig. 80. Only relatively minor differences between the CO cross sec-

TABLE 14

Relative cross sections for the $0 \rightarrow v$ vibrational transitions in CO at their maxima (the accuracy of the relative values is $\pm 20\%$; powers of ten are in parentheses)

v	Energy (eV)	Rel. cross section
1	1.91	1
2	2.02	0.33
3	1.78	0.17
4	1.89	0.11
5	2.01	0.073
6	2.15	0.042
7	2.26	0.024
8	2.41	0.012
9	2.55	5.0(−3)
10	2.72	1.8(−3)
11	2.90	5.2(−4)
12	3.36	1.1(−4)
13	3.54	3.8(−5)
14	3.69	1.4(−5)
15	3.83	2.4(−6)
16	3.97	5.3(−7)

tions and the N_2 cross sections may be observed. The cross section for the IR-active $v=1$ transition is much larger in CO below the resonance region. The shorter lifetime of the resonance in CO causes the structure to be shallower in the $v=1$ to $v=4$ cross sections. Further, the "substructures", that is the weak shoulders observed in the $v=3$ to $v=10$ cross sections in N_2, are absent in CO, a fact possibly related to the shorter lifetime of the resonance in CO. A subtle difference may be discerned in the threshold behaviour of the $v=11$ to $v=16$ cross sections: the onset is steeper in CO and more gradual in N_2. Apart from these differences the shapes of the cross sections are very similar in both molecules, in particular for the higher channels.

Relative differential cross sections at their maxima have been obtained by measuring the signal intensities at the maxima of the curves of Fig. 80 at constant pressure and correcting them for the variation of the analyzer sensitivity with residual energy. Under the assumption that the angular dependencies are the same for all v values these relative differential cross sections are equal to the relative integral cross sections. The resulting values are given in Table 14. (The absolute values have been reviewed by Trajmar et al. [139].) The relative cross sections are very similar for CO and N_2, indicating that the small dipole moment of CO and the shorter lifetime of the resonance have little effect on the relative cross sections.

15.2. Polyatomic molecules

The decay of the shape resonances in H_2, N_2, and CO described above resulted in strong excitation of low vibrational levels, with the cross section decreasing rapidly with increasing exit channel. A similar observation is made in polyatomic molecules and in addition the excitation is often characterized by a pronounced selectivity: in general only few of the many available vibrational modes are observed. Thus predominant excitation of the N–O stretch vibration via the 2.3 eV resonance in N_2O has been observed by Azria et al. [277] and Andric and Hall [278] and interpreted by Dubé and Herzenberg [279] within the impulse approximation in terms of different slopes of the negative ion potential surface along the different normal coordinates. Later it was shown that even in large polyatomic molecules with many vibrations, like benzene [168] and ethylene [280] only very few vibrations are excited by resonant electron scattering, the change of the geometry in the negative ion and symmetry selection rules [168, 280, 281] being the determining factors.

On the other hand trapped electron [282, 283] and ion scavenger [284] studies have shown intense (in comparison to electronic excitation) threshold electron peaks at energies of low-lying shape resonances for many polyatomic molecules. These early results have indicated that the polyatomic molecules are also excited to very high vibrational levels, leaving the scattered electron with nearly zero kinetic energy.

This section studies the excitation of high vibrational levels in several polyatomic molecules. Qualitatively similar results have been obtained with a number of organic molecules, and are illustrated here on the example of *p*-benzoquinone [52].

The transmission [171, 258] and vibrational excitation [52] spectra in *p*-benzoquinone have revealed three low-lying resonances, *a*, *b*, *c*, at 0.8 eV, 1.4 eV and 2.1 eV (probably the ^2A_u, $^2B_{3u}$, $^2B_{3u}$ states, see also Modelli et al. [285]), which all appear to have some π^* shape resonance character because of configuration interaction [51], and a broad σ^* shape resonance *d* with a maximum around 5 eV. The vibrational excitation caused by these resonances is illustrated in Fig. 82. With all four resonances distinct peaks are observed on the left side of the spectrum, where the energy-loss is relatively small and the energy of the departing electron relatively large. These distinct peaks point to high selectivity of the excitation process because the density of the vibrational states is very large even for relatively small vibrational energies for a molecule of this size. The selectivity is associated with the changes of the molecular geometry in the negative ion. The π^* orbitals are antibonding along the C=C and C=O bonds and their occupation causes lengthening of these bonds and excitation of the ν_2 (and perhaps also ν_3) vibration, which contains the C=C and C=O stretch motions. The 5 eV resonance with occupation of a σ^* orbital, antibonding along the C–H bonds, strongly excites the C–H stretch vibration.

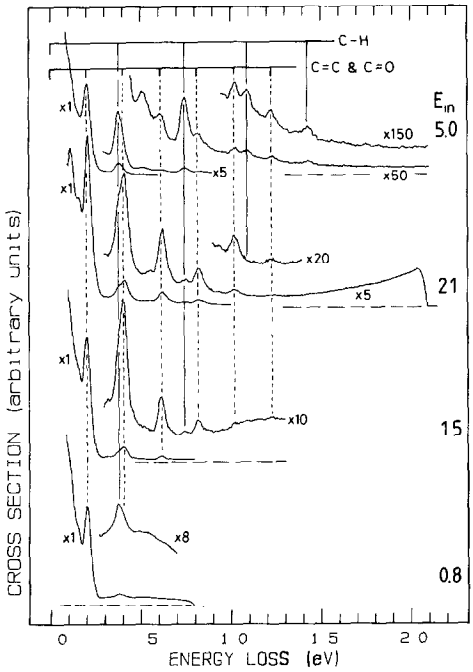

Fig. 82. Energy-loss spectra in *p*-benzoquinone (not on the same vertical scale), recorded at constant incident energies corresponding to the π^* resonances *a*, *b*, *c*, and the σ^* resonance *d*.

A signal is observed even for very high energy losses up to the value of the incident energy for the three π^* resonances, however. In contrast to the low energy losses no distinct vibrational levels may be discerned at high energy losses with the available resolution, indicating that the excitation is unselective, with many (or all) of the vibrational states present being excited with comparable intensities. In the following the selective excitation mechanism will be called the "specific" vibrational excitation and the unselective mechanism the "unspecific" excitation.

The intensity of the unspecific excitation as a function of increasing energy-loss (decreasing scattered electron energy) is different for the three resonances. It decreases for the lowest resonance at 0.8 eV, remains approximately constant for the 1.5 eV resonance, and increases for the 2.1 eV resonance, resulting in a peak of zero-energy electrons.

The role of the resonances in the unspecific excitation may be seen in the constant E_r spectra of Fig. 83. At low residual energies unspecific excitation results in strong peaks at the energies of the π^* resonances (*a*, *b*, and *c*). These peaks shift to the left on the energy-loss scale with increasing residual energy, indicating that they are fixed on the incident energy scale. No structure due to individual vibrational levels appears on these peaks, confirming the unselec-

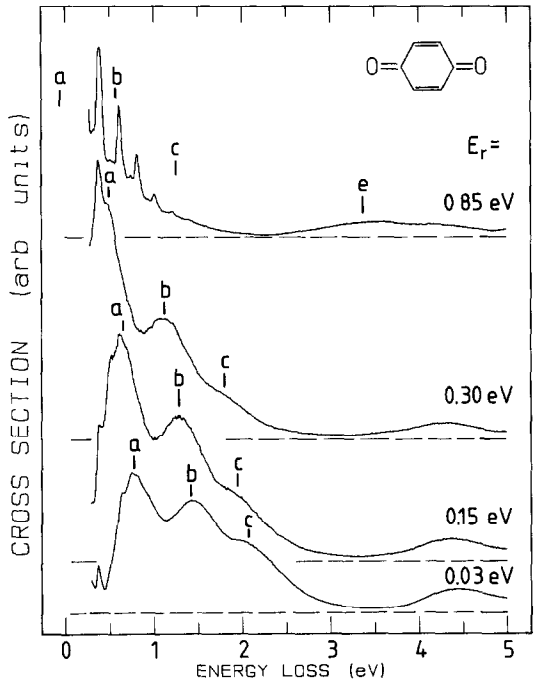

Fig. 83. Energy-loss spectra in *p*-benzoquinone (on the same vertical scale), recorded at constant energies above threshold. Incident energies corresponding to the resonances are indicated.

tivity of the unspecific vibrational excitation. The weak structure on the peak *a* in the spectra with $E_r = 0.03$ and 0.15 eV is probably the boomerang structure of the negative ion, which is also seen in the transmission spectrum. The specific vibrational excitation of long progressions in the ν_2 vibration is observed in the spectrum recorded with $E_r = 0.85$ eV, that is higher above threshold, in the low energy-loss region on the left side of Fig. 83. The spectra in Fig. 83 thus prove that the same resonances *a*, *b*, and *c* are involved in both the specific and the unspecific excitation.

The specific and unspecific vibrational excitation have been observed in many polyatomic molecules with low-lying shape resonances, for example acetaldehyde (Fig. 67), benzene (Fig. 32), naphthalene (Fig. 56), and octatetraene [286] and appear to be characteristic for all larger polyatomic molecules with low-lying shape resonances.

15.3. Carbon dioxide

After the recognition of the presence of the two types of vibrational excitation in many large polyatomic molecules it appeared interesting to examine the excitation of high vibrational levels in a small polyatomic molecule like

CO_2 to determine whether the excitation is selective near threshold and what kind of selectivity is encountered [287].

Vibrational excitation via the first shape resonance $^2\Pi_u$ at 3.6 eV has been studied over a large range of energy-losses by Boness and Schulz [103] and Cadez et al. [288]. Both groups observed a strong selectivity expected for the specific vibrational excitation; the occupation of the antibonding π^* orbital causes the CO_2^- state to have longer C=O distances and to be bent and consequently a long progression in the ν_1 symmetric stretch and weaker excitation of the bending vibration ν_2 have been observed (their relative intensity being a function of scattering angle). On the other hand the excitation of high vibrational levels in threshold spectra has also been reported (Hubin-Franskin and Collin [289], Dance et al. [290], Cvejanovic et al. [291]).

Figure 84 shows the vibrational excitation spectrum obtained with the trochoidal electron spectrometer at an incident electron energy within the $^2\Pi_u$ resonance. For energy-losses up to about 3 eV the spectrum agrees well with the previously published spectra, in particular with the $E_{in}=4.2$ eV, $\theta=20°$ spectrum of Cadez et al. [288], which has been recorded under similar scattering conditions. For very high energy losses the spectra are not incompatible, but the improved signal/noise ratio of the present spectrum permits a closer examination of the energy-loss region above 3 eV. Up to an energy-loss of about 3 eV specific excitation is observed. The spectrum is dominated by a long progression in the ν_1 symm. stretch vibration, the bending vibration ν_2 being weaker at low scattering angles. The intensity of the peaks does not drop quite linearly because of the pronounced boomerang structure observed in the vibrational cross sections (ref. 103 and Fig. 88).

At the energy-loss range 3.0–3.4 eV no distinct vibrational peaks are observed. At energy losses above 3.4 eV vibrational structure reappears, but the

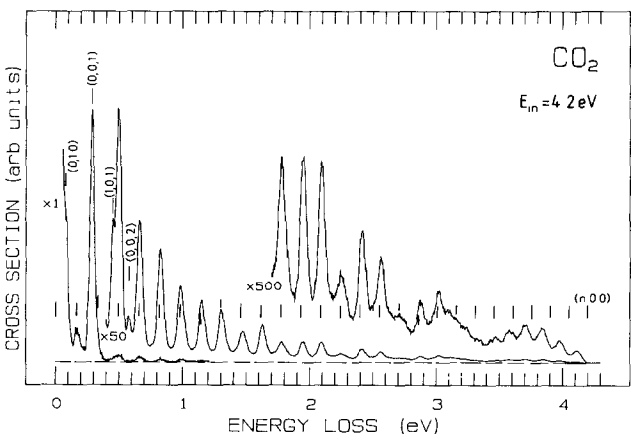

Fig. 84. Energy-loss spectrum in CO_2, recorded at a constant incident energy of 4.2 eV.

peaks lie in between the extrapolated positions for the $n\nu_1$ progression and must correspond to excitation of vibrations other than the $n\nu_1$ progression.

Figure 85 shows four spectra recorded at other incident energies within the first shape resonance. All four spectra may be divided qualitatively into three regions. Region I is dominated by the $n\nu_1$ progression, region II shows very complex structure, and in region III the peaks lie in between the extrapolated positions for the $n\nu_1$ progression.

The spectra of Fig. 85 indicate that the "complex" region II occurs approximately at a constant energy above threshold. Insight into the behaviour of the three regions may thus be gained by considering the spectra recorded at con-

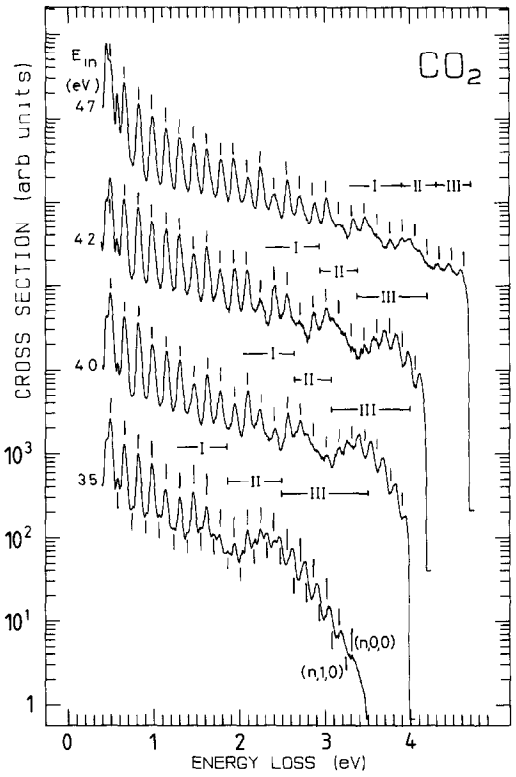

Fig. 85. Energy-loss spectrum in CO_2, recorded at the four constant incident energies indicated, and shown on a semilogarithmic scale to accommodate the large variations of signal intensity across the spectra. The vertical lines above the spectra indicate the calculated energies of the $(n,0,0)$ progression, the lines under the lowest curve the energies of the $(n,1,0)$ progression. The spectra are qualitatively divided into region I, dominated by $(n,0,0)$ excitation, region III characterized by the selectivity of the "second" type (see text), and a complex transition region II. Note that the $(n,1,0)$ progression is visibly excited in the $E_{in}=3.5$ eV spectrum in region I, but the peaks observed in region III of this spectrum fall neither onto the $(n,0,0)$ nor onto the $(n,1,0)$ progression.

stant energies above threshold, shown in Fig. 86. A long progression in the ν_1 vibration is observed at $E_r = 2.5$ eV, that is in the specific excitation region I. The observed peak positions agree with the predicted positions [292] up to about $18\nu_1$. At $E_r = 1.25$ eV, approximately in the "complex" region II, the $n\nu_1$ progression is still observed, but together with a large number of other, partially resolved peaks, whose energies or intensities do not exhibit any apparent regularity and which could not be assigned. At $E_r = 0.5$ eV, in the near-threshold region, a series of equidistant peaks whose energies fall in between the extrapolated $n\nu_1$ positions are observed.

High signal-to-noise ratio spectra of region III, recorded at three residual energies close to threshold, are shown in Fig. 87. The peaks do not shift to the left with increasing residual energy, that is they are locked to a given energy-loss and not to a given incident energy, indicating that the structure is not due to vibration of CO_2^-. Upon closer inspection these peaks are found to be significantly broader than the instrumental resolution and to exhibit a number of weak shoulders, that is to consist of groups of closely-spaced levels.

Finally, the energy dependence of the excitation of several representative energy losses is shown in Fig. 88. The cross sections are shown for two pairs of adjacent $(n,0,0)$ peaks ($n = 13, 14; 18, 19$), and at the two energy losses in between each pair. The cross sections have distinctly different shapes; the curves recorded at the "in between" energy losses have a steeper onset and fall off more rapidly after the first maximum then the curves recorded at the adjacent energy losses corresponding to $n\nu_1$ excitation.

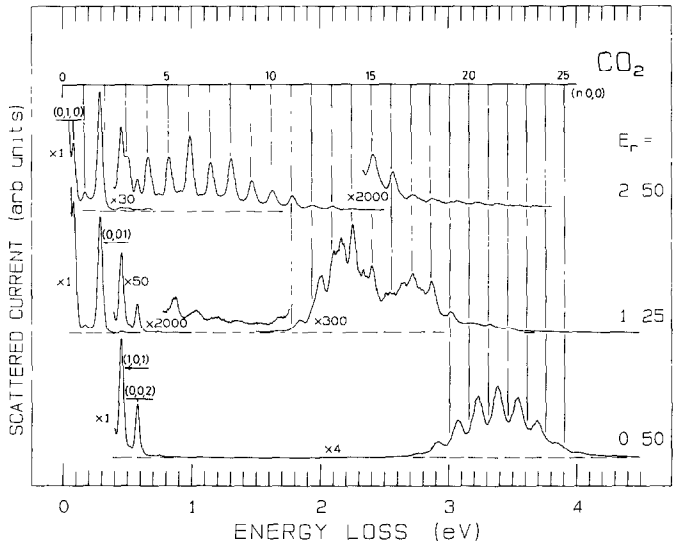

Fig. 86. Constant-residual-energy spectra in CO_2. The three spectra are not on the same vertical scale.

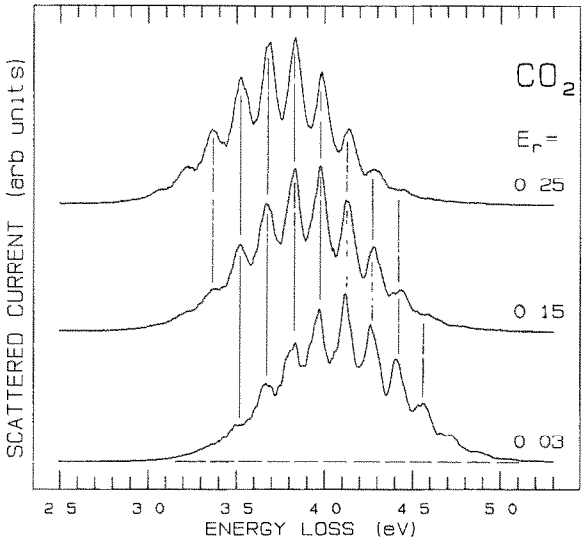

Fig. 87. Constant-residual-energy spectra recorded under conditions where the "second" (see text) type of selectivity prevails. The three spectra are not on the same vertical scale.

The vibrational excitation near threshold in CO_2 thus has some resemblance to the unspecific excitation in larger molecules in the sense that it does not follow the selectivity of the specific excitation and that many more vibrational levels are excited than in the specific, farther above threshold excitation. It differs from the larger molecules since although many vibrations are excited near threshold, they can still be partially resolved, and that a second kind of selectivity is observed near threshold, the many vibrations not being excited with equal intensity, but with intensity modulated with a period close to the symm. stretch vibration.

The mechanism of the "second" selectivity is not understood at present. It should be noted, however, that the second type of selectivity in the present experiment is observed under conditions where 3–4 eV of vibrational energy are deposited in the CO_2 molecule. The motions of the nuclei are probably largely chaotic at this high energy, because of the very high density of states and the strong coupling of the vibrations. The appropriate description of the vibrational motion is thus not in terms of normal modes, but in terms of trajectories, as has been done in the case (of an electronically excited state) of DCN [293], using the semiclassical spectral quantization technique. In this context it is interesting to observe that the experimental results are qualitatively reminiscent of the "spectroscopic order out of spectroscopic chaos" phenomena advanced theoretically for this type of systems by Taylor [294]. Taylor [294] proposes that in a region of a high density of states such as the quasicontinuum of molecular vibrations at high vibrational energy, where the usual

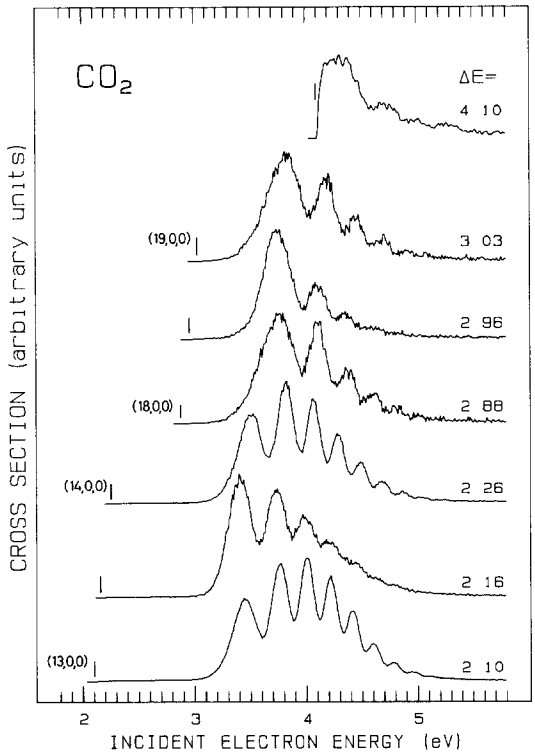

Fig. 88. Selected vibrational cross-sections in CO_2. The curves are not on the same vertical scale.

normal and local mode models had been thought to break down, there is embedded a high density of localized states which as a group resemble mode separable states. The consequence is that, in a spectral region with very many spectroscopic lines with mixed intensity and energy patterns that defy assignment, many fewer and broader regularly spaced peaks should emerge in a low resolution experiment, which correspond to groups of the localized states. One might speculate that the broadened peaks (Fig. 87) observed in the inherently low resolution electron energy-loss experiment could correspond to such groups of localized states.

15.4. Conclusions

The local-complex-potential model (boomerang model) is adequate for resonances with moderate lifetimes, and for cross sections not including thresholds, like the excitation of low vibrational levels in N_2. It has the advantage of giving a transparent physical picture of the excitation process. It becomes inadequate, however, for very short-lived resonances and near excitation thresh-

old. In these situations the non-local potential treatment proves to be successful. The **R**-matrix method could also well reproduce the N_2 cross sections.

It appears that for any larger polyatomic molecule two types of vibrational excitation via low-lying shape resonances occur.

One is the specific vibrational excitation, which occurs higher than about 0.5–1 eV above threshold, is highly selective with respect to the vibrational modes excited, and has been studied in several molecules. The dominant factors determining the selectivity are the changes in molecular geometry upon the transition from the neutral molecule to the negative ion. In symmetrical molecules symmetry selection rules apply and in some cases vibronic interactions between two resonances may cause the excitation of particular vibrations (ref. 169; see also Section 7.2.2.). In general the cross section of the specific vibrational excitation decreases very rapidly with increasing vibrational quantum excited.

The present report concentrates on the second type, the unspecific excitation, which results in slow scattered electrons ($E_r \leqslant 0.5$ eV) and excites a quasi-continuum of vibrational states without any apparent selectivity. Depending on the compound and resonance involved the cross section may decrease (but slower than the specific cross section), may remain approximately constant, or may even increase with increasing energy loss, resulting in a peak of threshold electrons. Thus, there is a tendency for the scattered electron to lose a large fraction or all of its energy to the vibrational degrees of freedom of the target molecule. Many low-lying shape resonances in many "large" molecules studied so far result in both the specific and the unspecific vibrational excitation.

A theoretical study which may point towards the interpretation of the unspecific vibrational excitation has been presented by Gauyacq [295, 296]. He has studied a model system with two vibrations, one large, representing the specific excitation, and the second very small, representing the vibrational quasi-continuum. When the two vibrations have been treated together, this model has been able to reproduce the essential qualitative features of the unspecific excitation, that is a strong excitation of the quasi-continuum and the tendency of the electron to lose almost all its energy.

APPENDIX: THE TROCHOIDAL ELECTRON SPECTROMETER

The principle of operation and a general description of the instrument has been given in Section 4.2.2. This section gives a technical description of the instrument, that is the operational and instrumental details which should be of interest to researchers wishing to construct and operate similar instruments.

A.1. Monochromator–analyzer system

The mechanical structure of the electron-optical system of the present instrument follows closely the original design of a trochoidal monochromator by

Stamatovic and Schulz [101, 102]. The basic unit is a stack of circular molybdenum plates with apertures, and other elements like the "D"-shaped elements providing the perpendicular electric field, and the target chamber. These elements are kept in alignment by precision ruby or metal balls and the entire stack is squeezed between end plates by means of three threaded rods with nuts. The present instrument, shown in Fig. A1, has three stacks, one each for the monochromator, the target chamber, and the analyzer subunits. Characteristic plate and aperture dimensions are given in Table A1. The shapes of representative electrodes are shown in Fig. A2.

The electrons are taken from a thoria-coated iridium-ribbon filament of the type used for Bayard–Alpert ion gauges. The heating current (5–6 A) is brought to the filament by a quadrupolar four-wire arrangement to prevent disturbing magnetic fields. The electrons are then collimated by an axial magnetic field of about 80 gauss and pass through a series of apertures held at different potentials. Typical operating potentials are given in Fig. A1. The plate M1 is the draw-out electrode and is held about 3 V positive with respect to the filament-centre (FC) potential. The electrode M2 is used to pulse the incident electron beam during time-resolved experiments and may be omitted in instruments operating only in the continuous mode. M3 and M4 are the resolution-defining

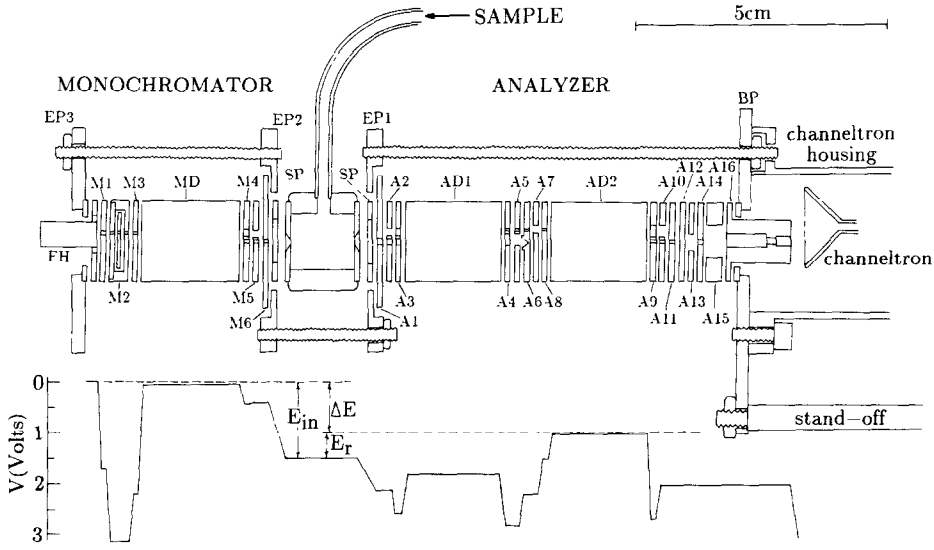

Fig. A1. Cross-section diagram of the trochoidal electron spectrometer. The individual monochromator electrodes M1–M6, filament holder FH, target chamber TC, spacers SP, and analyzer electrodes A1–A16 are separated by precision ruby balls. The entire stack is then squeezed between the base plates BP–BP3 by means of threaded rods. The main base plate BP is mounted on the vacuum flange by means of the "stand-offs". The lower portion of the figure shows the typical operating potentials in the instrument.

TABLE A1

Electrode dimensions

Dimension	Electrodes	Size (mm)
Plate diameter	M6 & A1	25.4
	Other	15.8
Plate thickness		1.0
Ruby ball circle		12.7
Ruby ball diameter		1.588
Spacing between plates		0.76
Length of "D's"		20.0
Gap between "D's"		3.2
Aperture offsets	M1-M3	1.6
	A4-A8	2.5
Aperture diameters	M1-M3	0.46
	M5, M6	0.6
	A1-A3	1.0
	A4-A6	0.6
	A8, A9	0.4
	A10, A11, A14	0.6

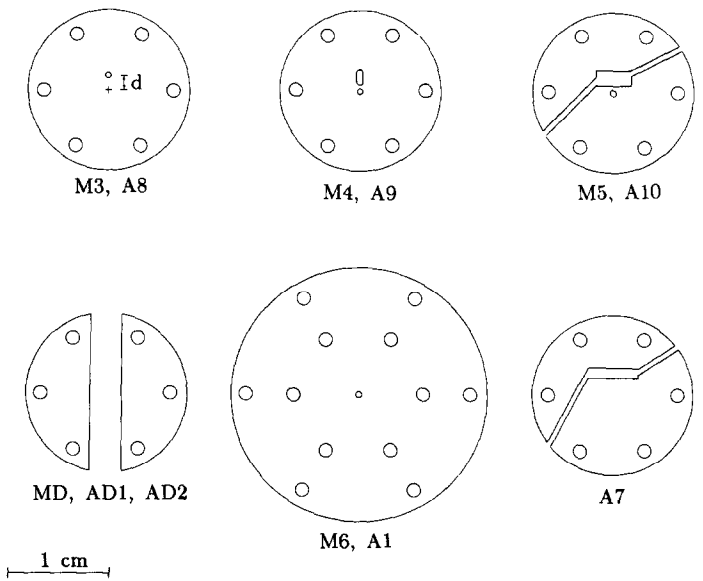

Fig. A2. Axial views of several representative electrodes.

electrodes and their apertures have smaller diameters than most other electrodes. The electrodes M5, M6, and the spacer SP are separated by conducting (beryllium-copper) balls short-circuiting them together and are thus held at

the same potential. Slightly larger ruby balls (2 mm diameter) are used between the spacers SP and the target chamber TC to improve the local pumping speed around the target chamber entrance and exit apertures.

The resolution of the first version of the instrument deteriorated due to electrons from the high-energy wing of the thermal energy distribution from the filament which were reflected from the plate M4, and after a second reflection at M3 entered the monochromator exit aperture, causing a high-energy "impurity" in the incident beam. A "fast electron trap", similar to the design described by Tam and Wong [112] is therefore incorporated in the plates M4 and M5 of the present version of the instrument. It consists of a vertical slit at the position of the expected impact of the fast electrons (i.e., vis-a-vis of the monochromator entrance aperture in M3) and a weak perpendicular electric field across the horizontal slit in the plate M5 (see Fig. A2). This field horizontally offsets the electrons which may be reflected from the electrode M6 so that they cannot re-enter the monochromator through the vertical slit in the plate M4. Similar reflection -preventing devices are placed at the entrance and the exit of the first analyzer and the exit of the second analyzer.

The electrons are accelerated to their final energy between the plate M6 and the target chamber. The inelastically scattered electrons are decelerated to a suitable energy between the target chamber and plate A1. The function of the first analyzer stage is to separate the weak inelastically scattered beam from the intense unscattered electron beam. It has relatively large apertures and is operated at low resolution, that is with high pass energy. The faster unscattered electrons are collected at the plate A6, the scattered electrons are transferred to the second analyzer stage, which has small entrance and exit apertures and is operated with smaller pass energy, that is at high resolution.

The choice of proper aperture diameters is crucial for correct operation of the spectrometer. Tests with the first version of the instrument have shown that plates with small apertures, which "skim" the main beam, cause a large background of stray electrons. This background appears to be due to electrons which have been inelastically nearly-forward scattered at the aperture edges and consequently have the right forward and perpendicular velocities to pass the analyzer. The number of apertures with small diameters is therefore kept as low as possible, limited to the four resolution-defining apertures M3, M4, A8, and A9 with approximately 0.4 mm diameter. The remaining apertures are larger. The target-chamber windows and the apertures A1–A3 are most critical in this respect and have 1 mm diameter. The choice of the actual aperture diameters has been based on the above qualitative consideration and is to some degree arbitrary; no attempt has been made to determine whether other diameters would provide a superior performance.

The second reflection suppressing device, comprising the vertical slit in A4 and a horizontal slit in A5, prevent backscattering of the main beam from the collector A6. The horizontal slit with adjustable electric field in the plate A7

permits a small horizontal deflection of the inelastically scattered beam to match it properly with the second analyzer entrance aperture A8. The slits in the plates A9 and A10 represent another reflection suppressing device. Finally, the energy analyzed electrons are counted behind the aperture A11. Tam and Wong [112] have reported the use of an iron torus to improve the rejection of electrons with large transverse energies. The present instrument includes a mumetal spacer A15 to test the properties of this device. It appears that electrons with large transverse energies are sufficiently rejected by the small analyzer apertures A8 and A9, and that the ferromagnetic torus is not effective in the present design. The mumetal spacer A15 and the deflectors A12 and A13 thus do not appear to be necessary for the function of the instrument and will not be included in future versions of the instrument.

A standard channeltron is used to count the electrons, but the special circumstances under which it is used have some consequences on its performance. It appears that the 80 gauss magnetic field present in the instrument focusses the secondary electrons within the channeltron. This focussing, together with the fact that the incoming electrons hit only a very small spot in the channeltron's cone, causes the secondary electrons within the channeltron to follow only very specific trajectories and to hit only very small spots on the continuous dynode surface. These spots deteriorate quickly and the gain of the channeltron is degraded much faster than in the absence of the magnetic field. This effect requires two precautions to be taken:

(a) Very high count rates, or high count rates over prolonged periods of time, should be avoided. Thus the incident and residual energies should not be set equal while the channeltron high voltage is on, preventing the unscattered beam from reaching the channeltron. The instrument should not be left counting unnecessarily on an intense inelastic peak. The channeltron is protected by a circuit which turns the high voltage off when the count rate exceeds 10^5 counts s^{-1}.

(b) The gain of the channeltron may be recovered by turning it 60° in its housing, causing the incoming electrons to hit a different spot on the channeltron's cone. This appears to change the electron trajectories within the channeltron, which then hit fresh, unused spots on the dynode surface.

A.2. Electronic circuit

A schematic diagram of the entire electronic circuit is shown in Fig. A3. The voltages for the individual monochromator and analyzer electrodes are derived from the monochromator and analyzer adjustable voltage sources modules. The basic unit of these sources is the low output impedance voltage source based on the LM317 voltage regulator. The output voltage may be manually varied in the range 1.25–32 V using a ten-turn potentiometer. A partial diagram of the monochromator adjustable voltage source module is shown in Fig.

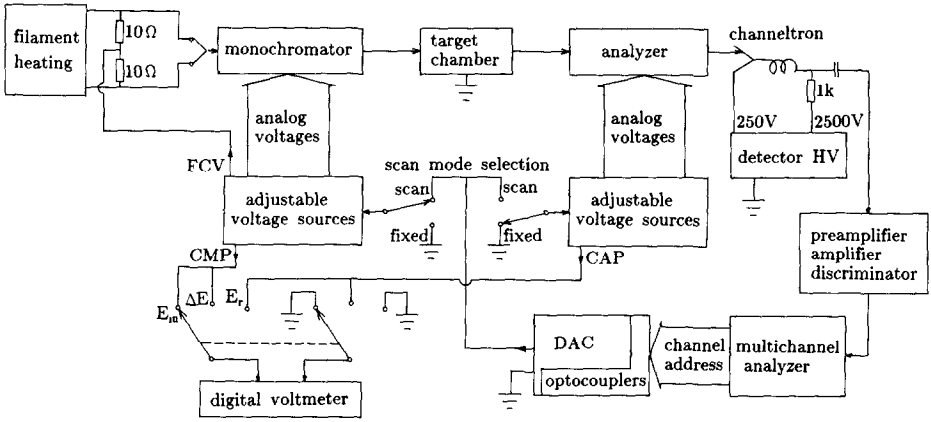

Fig. A3. Schematic diagram of the electronic circuit of the trochoidal electron spectrometer.

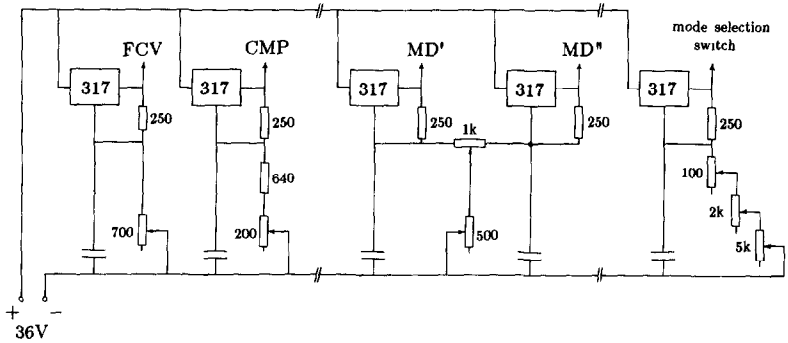

Fig. A4. A partial circuit diagram of the monochromator adjustable voltage source.

A4. The first voltage regulator generates the filament-centre voltage (FCV). The voltages for the electrodes M1–M5 are generated in the same manner. The second regulator shown in Fig. A4 generates the "corrected monochromator potential" (CMP), a voltage which is fed to a precision digital voltmeter and during the calibration of the instrument is adjusted so as to make the voltmeter's reading identical to the true incident energy. The circuit providing the voltages for the two "D's" is designed to change only the "D's" mean potential when the 500 Ω potentiometer is varied and to change only the potential difference between the two "D's" when the 1 kΩ potentiometer is varied. The incident electron energy may be manually varied by changing the output voltage of the rightmost voltage regulator, whose output is connected either to ground (fixed incident energy) or to the voltage ramp generator (scanned incident voltage) through the mode selection switch. Three potentiometers are used in series to provide fine and coarse adjustment of the incident energy. The analyzer adjustable voltage source is designed in a similar manner.

During most of the work described here the data have been accumulated by a Canberra Model 30 multichannel analyzer modified to provide the current channel address for the digital-to-analog converter (DAC) generating the voltage ramp. The spectra have subsequently been transferred to a PDP-11/34 computer for plotting and storage. During the later stages of the work an Olivetti M24 personal computer has been converted into a multichannel analyzer by means of a universal counter and parallel interface expansion cards. The same type of computer is also used to process spectra and prepare figures. The improved control of the acquisition process afforded by the computer results in an improved overall performance of the instrument, illustrated by the following two specific examples:

(a) The acquisition program includes the "adjustment mode" in which a single energy-loss band (such as the $E^3\Sigma_g^+$ band in N_2) is scanned repetitively and displayed normalized to the full vertical height after each scan to facilitate the comparison of its shape with previous scans even when the signal intensity changes. The resolution (FWHM) is calculated and displayed after each scan, together with the count rate. This feature provides an improved feedback on the effect of any changes in the operating conditions and permits a more efficient empirical adjustment of the instrument. Fig. A5 shows a spectrum recorded after a "computer-aided" adjustment of the instrument. The bands have an apparent width of 25 meV, better than 30 meV, which is the best resolution obtained with the MCA-operated instrument (Fig. 19).

(b) Adjustment of the instrument for distortion-free energy-dependence curves is facilitated by the computer's ability to continuously display the spectrum corrected for the analyzer's transmission function.

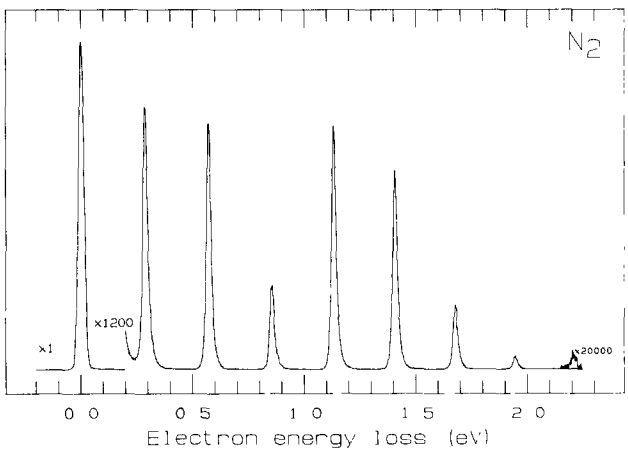

Fig. A5. Energy-loss spectrum in N_2, recorded with a constant incident energy of 2.3 eV. The peak at $\Delta E = 0$ is caused by the unscattered electron beam. The width of the inelastic features is around 25 meV.

A.3. Vacuum and sample-inlet systems

A global view of the instrument is shown in Fig. A6. The monochromator and analyzer stacks are mounted horizontally in a cross-shaped vacuum chamber. The chamber is welded from a standard stainless tube (150 mm diameter) and sealed with "O"-rings. It is pumped by a 150 mm diffusion pump with incorporated water-cooled baffle and filled with Santovac 5 oil. This arrangement does not result in problems due to oil contamination even after several years of operation without cleaning. The top arm of the chamber contains a liquid-nitrogen cooled trap which decreases the pressure of sample vapour during operation. Typical background pressure while measuring condensable organic vapours is 2×10^{-7} mbar. This low pressure permitted stable operation for several days with most samples, thus allowing extended accumulation times.

The sample introduction system is very compact to reduce its internal surface and facilitate its heating during measurements of involatile compounds. It permits the simultaneous introduction of an organic vapour and a calibrating gas through two needle valves.

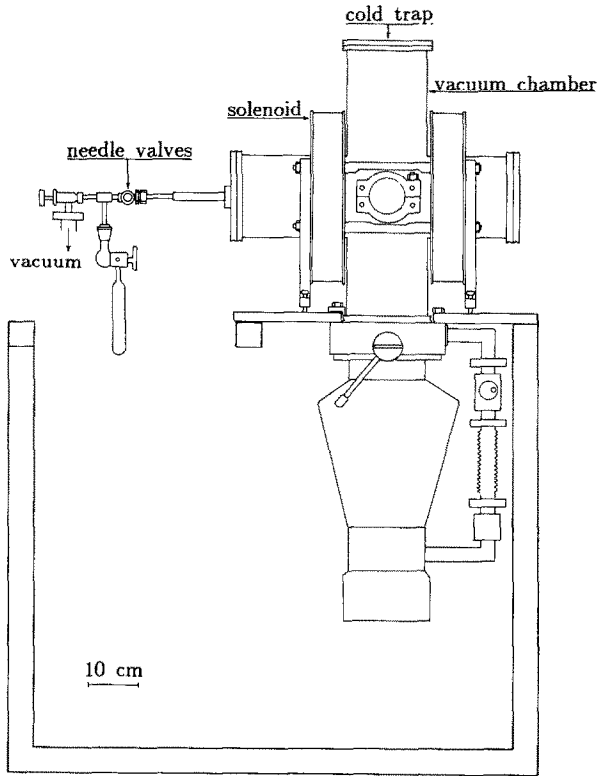

Fig. A6. Outside view of the spectrometer.

A.4. Operation

A.4.1. Transmission spectroscopy

The electrodes A1–A16 are externally short-circuited and the total current collected on them is measured with a sensitive electrometer in this mode of operation. The direct phase sensitive detection of the derivative of the transmitted current commonly used in ET spectroscopy has not yet been incorporated in the present spectrometer. Instead, the transmitted current is digitized by means of a voltage-to-frequency converter (VFC), whose output pulses are counted by the multichannel analyzer. The derivative of the transmitted current may be then calculated digitally by the computer.

The details of the operation of an ET spectrometer have been analyzed and discussed in detail by Johnston and Burrow [74]. These authors have shown that the detailed mechanism of the rejection of scattered electrons in a magnetically collimated instrument is far more complicated than might appear on the first sight, that a large fraction of the scattered electrons (dependent on the operating conditions) may not be rejected in these instruments, and that an improper operation may result in several types of artifacts. All these findings also apply to the present instrument.

The diameters of the target chamber entrance and exit apertures in the present instrument (1 mm) are smaller than in most modern ETS instruments ($\approx$3 mm). As a consequence, application of a retarding potential behind the target chamber leads to "focussing", that is to artifact wavy structure in the transmitted current and the present spectrometer can in most instances only be used in the low rejection mode, that is without retardation. On the other hand the small apertures cause the "geometrical" rejection mechanism to become active at low energies. The Larmor radius of an electron scattered elastically at 90° becomes equal to the aperture radius at an incident energy of 1.4 eV. The instrument thus relies on the backscattering rejection mechanism at low energies and geometrical rejection at higher energies. The onset of the geometrical rejection mechanism may be accompanied by wavy structure in the spectrum, which may be reduced to below disturbance level by alignment of the magnetic field and empirical adjustment of the potentials on M4 and M5.

A.4.2. Energy-loss and energy-dependence spectroscopy

The instrument may record energy-loss spectra with constant incident or residual energies, or energy-dependence spectra, depending upon which combination of incident and residual energies is varied during the scan. The incident electron current remains constant when E_{in} is varied and the sensitivity of the instrument therefore remains constant when constant E_r spectra are recorded. The transmission of the analyzer, however, increases rapidly with decreasing residual energy. The constant E_{in} and the constant ΔE spectra must

be corrected for this variation. The uniform energy distribution of electrons from near-threshold ionization of helium [297–298], used for calibration of instrument sensitivity by Pichou et al. [107] and Phillips [300], is used to determine the analyzer transmission function. The results are shown in Fig. A7. First-order prediction of the trochoidal analyzer transmission function is based on the assumption that only electrons spiralling with Larmor radii smaller than a certain value given by the size of the analyzer entrance aperture can enter the analyzer. Thus only electrons with a perpendicular velocity less then a certain fixed value given by the aperture size and the magnetic field strength will be detected. This results in an analyzer acceptance angle inversely proportional to electron velocity or analyzer transmission inversely proportional to the electron energy. When the raw data, curve (a) in Fig. A7, is corrected for this variation, an essentially flat function is obtained, the only imperfection being a slow linear rise of the signal with increasing residual energy, due to some second-order effects not included in the above argument. Therefore a small empirical correction, linear in energy, was applied to the data after the $1/E$ correction. The result, curve (b) in Fig. A7, is constant to within $\pm 20\%$ from 0.05 to 2.5 eV.

Two remarks concerning the acceptance angle should be made. First, from the above discussion it follows that the acceptance angle is a function of residual energy. An upper limit on the perpendicular electron velocity may be obtained from the instrument energy resolution. Assuming a 30 meV band-width of the analyzer part alone results in an upper limit on acceptance half-angle of 20° at $E_r = 0.25$ eV, 10° at $E_r = 1.0$ eV, and 4.5° at $E_r = 5$ eV. The true angular resolution is better than the upper limits because the finite perpendicular electron energies are only one of several factors limiting the analyzer resolution. The instrument thus has good angular resolution at large residual energies, but

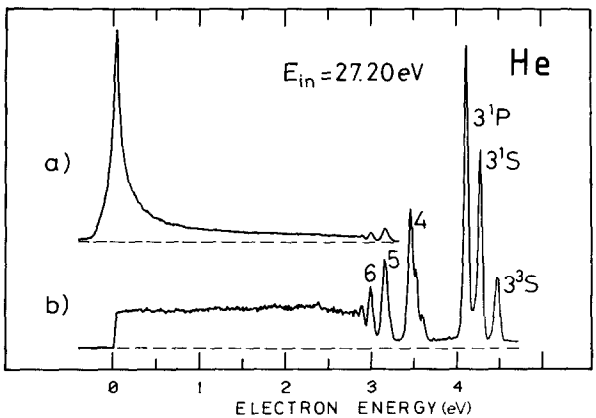

Fig. A7. Spectrum of the near-threshold ionization continuum in He, used for calibration of the instrument's transmission function. Curve (a) is the raw data, curve (b) is corrected.

the acceptance half angle can approach 90° at threshold. This property might influence the shape of energy-dependence curves near threshold for strongly angle dependent cross sections.

Second, experiments with a pulsed incident beam revealed that the instrument collects efficiently both forward and backward scattered electrons. The experiment is illustrated in Fig. A8. Two groups of arrival times are observed, the first being due to forward scattered electrons, and the second being due to backward scattered electrons, which are reflected on the potential barrier at the monochromator exit (see Fig. A1), traverse the target chamber and also enter the analyzer, albeit delayed in time with respect to the forward scattered electrons. The measured cross sections are thus a superposition of forward and backward scattering.

The weighting factors of the superposition cannot be determined from the data in Fig. A8 because the available measurements of angular distributions in electronic excitation in He do not extend to 0° and 180°. The reflection of the backward scattered electrons is expected to be very efficient, however, since there is no evident loss mechanism. The effect could in principle be used to measure precise ratios of 0° and 180° cross sections and thus to extend the angular distribution measurements from the electrostatic instruments, which generally do not reach angles larger than 120°–140°.

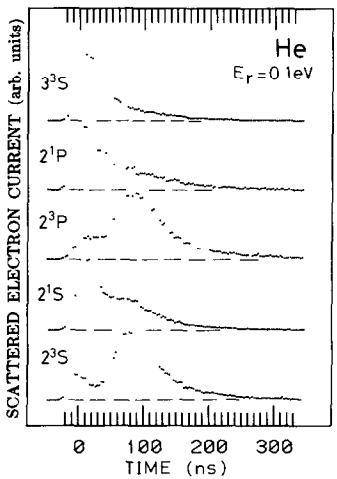

Fig. A8. Spectra of arrival times of inelastically scattered electrons after exciting the four lowest excited states in He. The residual energy was 0.10 eV. The incident electron beam is pulsed with 10 ns pulse width and 1 MHz repetition frequency. The arrival times are measured with a time-to-amplitude converter and a multichannel analyzer in the pulse-height analysis mode. The first group is the forward scattered electrons. The group delayed about 70 ns is the backward scattered electrons, which have been reflected at the monochromator entrance. The spectra indicate that, at 100 meV above threshold, 180° scattering is prevalent in the excitation of the 2^3S and 2^3P states, but is unimportant in the excitation of the 2^1P and 3^3S states.

In conclusion, several practical considerations concerning the instrument's operation are mentioned:

(a) It is often difficult to measure small energy losses, because they are obscured by the low energy tail of the very intense unscattered electron beam entering the analyzer. The performance at the low energy-loss (<0.7 eV) region may be improved by using the electrodes M4 and M6 as a retardation analyzer to eliminate the low-energy tail from the main beam energy distribution. With this adjustment energy-loss peaks as low as 0.2 eV may be measured.

(b) The adjustment requirements for measuring low energy losses (M4 and M5 "tight", functioning as a retarding analyzer) and for undistorted, "focussing"-free energy dependence curves (M4 and M5 "open", that is 0.5–2 eV positive with respect to filament centre) are mutually exclusive. Consequently, it becomes increasingly difficult to measure distortion-free energy-dependence curves as the energy loss is decreased, being very difficult for $\Delta E < 1$ eV and practically impossible for $\Delta E < 0.3$ eV.

(c) Artifact bands, caused by scattering of the main beam from the analyzer apertures, sometimes occur in the constant E_r energy-loss spectra. These artifacts are relatively easy to identify, since they persist when the sample gas is turned off. These bands may usually be removed by adjusting the direction of the magnetic field, and by lowering the potential on the electrodes A1–A3.

(d) In general it is not necessary to "tune" the incident beam through the entire instrument up to the channeltron in a "focussing-free" manner (i.e., without losses and variations in energy dependence). The incident beam only needs to remain highly constant up to the target chamber. Except for extremely forward-peaked cross sections the electrons are "reoriented" in the scattering process, so that reasonably distortion-free inelastic energy-dependence curves are obtained even when the energy-dependence of the main beam collected at the channeltron is seriously distorted. The distortion of the energy-dependence curves may consequently be more serious for extremely forward-peaked cross sections, where the "reorientation" does not occur. With careful alignment of the magnetic field the main beam may, however, be tuned all the way down to the channeltron with little distortion, opening the possibility of modifying the trochoidal electron spectrometer to become a high quality instrument for the measurement of total cross section, with good rejection of scattered electrons.

As a consequence of points (a) and (b) recording of the energy-dependence of pure vibrational excitation is one of the most difficult experiments, because it is extremely difficult to entirely eliminate the "focussing", that is the wavy distortions of the spectra, particularly at low ΔE. The distortions can be minimized by lengthy empirical adjustments of the direction and strength of the magnetic field and of all potentials within the instruments. The roles of the different parameters are often interdependent, the optimum adjustment may

be different for different energy-losses, and will change with time and when the sample gas is changed. Often minimal distortion of the energy-dependence curves is obtained only when optimum sensitivity and resolution are sacrificed. Suitable test curves are the excitation of the $v=1$, 2, and 3 vibrational levels in H_2. Energy dependence of larger ΔE values (electronic excitation) is easier to measure.

ACKNOWLEDGEMENTS

I wish to express my sincere appreciation to Professor E. Haselbach for his continuing support and encouragement during the entire period of my work in Fribourg. I further thank my colleagues Dr. Thomas Bally and Prof. Paul Suppan for innumerable discussions and continuous help in everyday matters. My special thanks go to R. Dressler, who contributed in a decisive manner to the results by his engagement and excellent work on the dissociative attachment experiment. I thank P.D. Burrow, K.D. Jordan, and A. Modelli for valuable comments. I am indebted to E. Brosi, P.-H. Chassot, and M. Gremaud for their help in the construction of the apparatuses. The experiments could never have been accomplished without their creativity and exact work in designing and fabricating the mechanical and electronical components. This work is part of project No. 2.800-0.88 of the Schweizerischer Nationalfonds zur Förderung der wissenschaftlichen Forschung.

REFERENCES

1 H.S.W. Massey, E.W. McDaniel and B. Bederson (Eds.), Applied Atomic Collision Physics, Vols. 1-5, Academic Press, New York, 1984.
2 L.G. Christophorou (Ed.), Electron-Molecule Interactions and their Applications, Vols. 1 and 2, Academic Press, Orlando, 1984.
3 I. Shimamura and K. Takayanagi (Eds.), Electron-Molecule Collisions, Plenum Press, New York, 1984.
4 C.F. Barnett and M.F.A. Harrison (Eds.), Plasmas, Applied Atomic Collision Physics, Vol. 2, Academic Press, New York, 1984.
5 E.W. McDaniel and W.L. Nighan (Eds.), Gas Lasers, Applied Atomic Collision Physics, Vol. 3, Academic Press, New York, 1984.
6 L.G. Christophorou and R.S. Hunter, in L.G. Christophorou (Ed.), Electron-Molecule Interactions and their Applications, Vol. 2, Academic Press, Orlando, 1984, Chap. 5.
7 J.W. Coburn, in H.S.W. Massey, E.W. McDaniel and B. Bederson (Eds.), Applied Atomic Collision Physics, Vol. 4, Academic Press, New York, 1984, Chap. 13.
8 R. Hartmann, Metalloberfläche, 39 (1985) 411, and references cited therein.
9 J.F. Waymouth, in H.S.W. Massey, E.W. McDaniel and B. Bederson (Eds.), Applied Atomic Collision Physics, Vol. 5, Academic Press, New York, 1984, Chap. 14.
10 A. Fontijn, in H.S.W. Massey, E.W. McDaniel and B. Bederson (Eds.), Applied Atomic Collision Physics, Vol. 5, Academic Press, New York, 1984, Chap. 13.

11 H.S.W. Massey and D.R. Bates (Eds.), Atmospheric Physics and Chemistry, Applied Atomic Collision Physics, Vol. 1, Academic Press, New York, 1984.
12 M.A. Biondi, in S.C. Brown (Ed.), Electron-Molecule Scattering, John Wiley, New York, 1979,Chap. 2.
13 R.G. Roble, Chem. Eng. News, 64 (24) (1986) 23.
14 J.E. Lovelock, in H.S.W. Massey, E.W. McDaniel and B. Bederson (Eds.), Applied Atomic Collision Physics, Vol. 5, Academic Press, New York, 1984, Chap. 1.
15 L.G. Christophorou, D.R. James and R.Y. Pai, in H.S.W. Massey, E.W. McDaniel and B. Bederson (Eds.), Applied Atomic Collision Physics, Vol. 5, Academic Press, New York, 1984, Chap. 4.
16 M. Inokuti, in H.S.W. Massey, E.W. McDaniel and B. Bederson (Eds.), Applied Atomic Collision Physics, Vol. 4, Academic Press, New York, 1984, Chap. 3.
17 T. Czvikovszky, Rad. Phys. Chem., 26 (1985) 547.
18 G.J. Schulz, Rev. Mod. Phys., 45 (1973) 378, 423.
19 H. Dieck, B. Bruder and K.-D. Franz, Chem. Ber., 116 (1983) 136; H. Dieck and E. Haupt, Chem. Ber., 116 (1983) 1540.
20 T. Shida, E. Haselbach and T. Bally, Acc. Chem. Res., 17 (1984) 180.
21 K.D. Jordan and P.D. Burrow, Acc. Chem. Res., 11 (1978) 341.
22 P.D. Burrow, J.A. Michejda and K.D. Jordan, J. Chem. Phys., 86 (1987) 9.
23 K.D. Jordan and P.D. Burrow, Chem. Rev., 87 (1987) 557.
24 M. Allan, Helv. Chim. Acta, 65 (1982) 2008.
25 R.A. Dressler, The Dissociative Decay of Short-Lived Polyatomic Anions Formed by Electron Impact, Ph.D. Thesis, University of Fribourg, 1985.
26 J. Franck and G. Hertz, Verh. Dtsch. Phys. Ges., 16 (1914) 457.
27 R.S. Berry, S.A. Rice and J. Ross, Physical Chemistry, John Wiley, New York, 1980.
28 H.S.W. Massey and E.H.S. Burhop, Electronic and Ionic Impact Phenomena, Oxford University Press, London, 1969.
29 M.A. Biondi, A. Herzenberg and C.E. Kuyatt, Phys. Today, October 1979, p. 44.
30 R.N. Compton and R.H. Huebner, Adv. Radiat. Chem., 2 (1970) 281.
31 L.G. Christophorou, Atomic and Molecular Radiation Physics, Wiley-Interscience, London, 1971.
32 D.F. Dance and I.C. Walker, Chem. Phys. Lett., 18 (1973) 601.
33 L.G. Christophorou, Adv. Electron. Electron Phys., 46 (1978) 55.
34 L.G. Christophorou, M.W. Grant and D.L. McCorkle, Adv. Chem. Phys., 36 (1977) 413.
35 M.J.W. Boness, I.W. Larkin and L. Moore, Chem. Phys. Lett., 1 (1967) 292.
36 L. Sanche and G.J. Schulz, Phys. Rev. A, 5 (1972) 1672.
37 L. Sanche and G.J. Schulz, J. Chem. Phys., 58 (1973) 479.
38 I. Nenner and G.J. Schulz, J. Chem. Phys., 62 (1975) 1747.
39 (a) M. Guerra, G. Distefano, D. Jones, F.P. Colonna and A. Modelli, Chem. Phys., 91 (1984) 383;
(b) M. Guerra, D. Jones, G. Distefano, A. Foffani and A. Modelli, J. Am. Chem. Soc., 110 (1988) 375.
40 A.E. Howard and S.W. Staley, ACS Symp. Ser., 263 (1984) 183.
41 J.C. Giordan, J.H. Moore and J.A. Tossel, ACS Symp. Ser., 263 (1984) 193.
42 B. Ciommer, K.M. Nguyen, H. Schwarz, G. Frenking, G. Kwiatkowski and E. Illenberger, Chem. Phys. Lett., 104 (1984) 216.
43 V. Balaji, K.D. Jordan, P.D. Burrow, M.N. Paddon-Row and H.K. Patney, J. Am. Chem. Soc., 104 (1982) 6849.
44 H. Fischer, in H.G. Viehe et al. (Eds.), Substituent Effects in Radical Chemistry, D. Reidel, Dordrecht, Holland, 1986, p. 123.
45 K.D. Jordan and P.D. Burrow, Chem. Phys., 45 (1980) 171.

46 A. Herzenberg, in I. Shimamura and K. Takayanagi (Eds.), Electron-Molecule Collisions, Plenum Press, New York, 1984, Chap. 3, pp. 191-274.
47 M.A. Morrison, Aust. J. Phys., 36 (1983) 239.
48 N.F. Lane, Rev. Mod. Phys., 52 (1980) 29.
49 J. Simons and K.D. Jordan, Chem. Rev., 87 (1987) 535.
50 (a) K. Takayanagi, in I. Shimamura and K. Takayanagi (Eds.), Electron-Molecule Collisions, Plenum Press, New York, 1984, pp. 1-87.
(b) S. Trajmar and D.C. Cartwright, in L.G. Christophorou (Ed.), Electron-Molecule Interactions and their Applications, Vol. 1, Academic Press, Orlando, 1984, pp. 155-249.
51 Y. Harada, Mol. Phys., 8 (1964) 273.
52 M. Allan, Chem. Phys., 84 (1984) 311.
53 K.D. Jordan and P.D. Burrow, ACS Symp. Ser., 263 (1984) 165.
54 P.D. Burrow, J.A. Michejda and J. Comer, J. Phys. B, 9 (1976) 3225.
55 M. Le Dourneuf, V.K. Lan and J.M. Launay, J. Phys. B, 15 (1982) L685.
56 Vo Ky Lan, M. Le Dourneuf and J.M. Launay, in J. Hinze (Ed.), Electron-Atom and Electron-Molecule Collisions, Plenum Press, New York, 1983, p. 161.
57 M. Le Dourneuf and J.M. Launay, Lect. Notes Chem., 35 (1984) 69. (F.A. Gianturco and G. Stefani (Eds.), Wavefunctions and Mechanisms from Electron Scattering Processes, Springer, Berlin, 1984, p. 69.)
58 D. Teillet-Billy, Attachment Dissociatif sur des Molécules Polaires et très Polaires, Thesis (Pour le grade de Docteur ès Sciences), Université de Paris-Sud, Orsay, 1985.
59 M. Allan, J. Phys. B, 18 (1985) L451.
60 D. Teillet-Billy and J.P. Gauyacq, J. Phys. B, 17 (1984) 4041.
61 A. Huetz, I. Cadez, F. Gresteau, R.I. Hall, D. Vichon and J. Mazeau, Phys. Rev. A, 21 (1980) 622.
62 D. Teillet-Billy, L. Malegat and J.P. Gauyacq, Excitation Electronique dans les Collisions Electron-O_2, in C. Tavard and C. DalCappelo (Eds.), XIème Colloque sur la Physique des Collisions Atomiques et Electroniques, Université de Metz (France), 1986, Vol. 1, p. 152.
63 J.P. Gauyacq, D. Teillet-Billy, L. Malégat, R. Abouaf and C. Benoit, Electronic excitation in $e^- - O_2$ collisions: Excitation of the $(\pi_u^4\pi_g^2)$ and $(\pi_u^3\pi_g^3)$ O_2 states, 15. ICPEAC, Brighton, U.K., 1987, contributed papers, Abstr. 313.
64 E.N. Lassettre and A. Skerbele, Methods Exp. Phys. B, 3 (1974) 868.
65 B.S. Hudson, B.E. Kohler and K. Schulten, Excited States, 6 (1982) 1.
66 R.J. Hall and F.H. Read, in I. Shimamura and K. Takayanagi (Eds.), Electron-Molecule Collisions, Plenum Press, New York, 1984, Chap. 5, p. 351.
67 E.N. Lassettre, A. Skerbele and M.A. Dillon, J. Chem. Phys., 50 (1969) 1829.
68 L.D. Ziegler and B.S. Hudson, Excited States, 5 (1982) 41.
69 S. Trajmar and D.F. Register, in I. Shimamura and K. Takayanagi (Eds.), Electron-Molecule Collisions, Plenum Press, New York, 1984, pp. 427-493.
70 E.N. Lassettre, J. Chem. Phys., 43 (1965) 4479.
71 F.H. Read and G.L. Whiterod, Proc. Phys. Soc. London, 85 (1965) 71.
72 K.N. Klump and E.N. Lassettre, Chem. Phys. Lett., 51 (1977) 99.
73 R. Azria, Y. Le Coat and J.P. Guillotin, J. Phys. B, 13 (1980) L505.
74 A.R. Johnston and P.D. Burrow, J. Electron. Spectrosc. Relat. Phenom., 25 (1982) 119.
75 A. Kupperman, J.K. Rice and S. Trajmar, J. Phys. Chem., 72 (1968) 3894.
76 G.C. King, J.W. McConkey and F.H. Read, J. Phys. B, 10 (1977) L541.
77 D. Vichon, F. Gresteau, A. Huetz and J. Mazeau, J. Mol. Spectrosc., 73 (1978) 405.
78 L. Vuskovic, S.K. Srivastava and S. Trajmar, J. Phys. B, 11 (1978) 1643.
79 D.C. Wilden, P.J. Hicks and J. Comer, J. Phys. B, 12 (1979) 1579.
80 D. Spence, J. Chem. Phys., 74 (1981) 3898.
81 J.P. Doering and R. McDiarmid, J. Chem. Phys., 73 (1980) 3617.

82 T. Abuain, I.C. Walker and D.F. Dance, J. Chem. Soc., Faraday Trans. 2, 80 (1984) 641.
83 N.A. Borisevich, V.V. Gruzinski, V.A. Suchkov, S.M. Kazakov and O.V. Khristoforov, Spectrosc. Lett., 18 (1985) 731.
84 A. Kuppermann, W.M. Flicker and O.A. Mosher, Chem. Rev., 79 (1979) 77.
85 R.J. Celotta and H.H. Huebner, in C.R. Brundle and A.D. Baker (Eds.), Electron Spectroscopy, Vol. 3, Academic Press, 1979, p. 41.
86 K. Jung, Th. Antoni, R. Müller, K.-H. Kochem and H. Ehrhardt, J. Phys. B, 15 (1982) 3535.
87 F.H. Read and G.C. King, in I. Shimamura and M. Matsuzawa (Eds.), Symposium on Electron-Molecule Collisions, Invited Papers, University of Tokyo, 1979, p. 155.
88 M. Tronc, G.C. King and F.H. Read, J. Phys. B, 12 (1979) 137.
89 G.C. King and F.H. Read, in B. Crasemann (Ed.), Atomic Inner Shell Physics, Plenum Press, 1985, Chap. 9, p. 317.
90 R.A. Dressler, M. Allan and E. Haselbach, Chimia, 39 (1985) 385.
91 F. Linder, Crossed-Beam Experiments at Thermal Energies, Invited Lecture, XII. SPIG, Sibenik, Yugoslavia, 1984.
92 J. Ferch, B. Granitza and W. Raith, J. Phys. B, 18 (1985) L445.
93 E.P. Wigner, Phys. Rev., 73 (1948) 1002.
94 H. Ehrhardt, K. Jung, K.-H. Kochem and W. Sohn, in F.A. Gianturco and G. Stefani (Eds.), Lecture Notes in Chemistry, Vol. 35, Springer, 1984, pp. 32–38.
95 C.E. Kuyatt, Methods Exp. Phys. A, 7 (1968) 1.
96 H.S.W. Massey, Negative Ions, 3rd edn., Cambridge University Press, Cambridge, 1976.
97 G.J. Schulz, Phys. Rev., 116 (1959) 1141.
98 D.E. Golden and H.W. Bandel, Phys. Rev., 38 (1965) A14.
99 R.E. Kennerly, Phys. Rev. A, 21 (1980) 1876.
100 I.C. Walker, Chem. Soc. Rev., 3 (1974) 467.
101 A. Stamatovic and G.J. Schulz, Rev. Sci. Instrum., 39 (1968) 1752.
102 A. Stamatovic and G.J. Schulz, Rev. Sci. Instrum., 41 (1970) 423.
103 M.J.W. Boness and G.J. Schulz, Phys. Rev. A, 9 (1974) 1969.
104 J.A. Simpson, Rev. Sci. Instrum., 35 (1964) 1698.
105 E. Harting and F.H. Read, Electrostatic Lenses, Elsevier, Amsterdam, 1976.
106 S. Daviel, B. Wallbank, J. Comer and P.J. Hicks, J. Phys. B, 15 (1982) 1929.
107 F. Pichou, A. Huetz, G. Joyez, M. Landau and J. Mazeau, J. Phys. B, 9 (1976) 933.
108 K. Rohr and F. Linder, J. Phys. B, 9 (1976) 2521.
109 J.M. Phillips and S.F. Wong, Phys. Rev. A, 23 (1981) 3324.
110 W. Sohn, K. Jung and H. Ehrhardt, J. Phys. B, 16 (1983) 891.
111 M. Allan, Int. J. Quantum Chem., 31 (1987) 161.
112 W.-C. Tam and S.F. Wong, Rev. Sci. Instrum., 50 (1979) 302.
113 F.H. Dorman, J. Chem. Phys., 44 (1966) 3856.
114 P.J. Chantry, Phys. Rev., 172 (1968) 125.
115 R.A. Dressler and M. Allan, Chem. Phys., 92 (1985) 449.
116 C. Schermann, I. Cadez, P. Delon, M. Tronc and R.I. Hall, J. Phys. E, 11 (1978) 746.
117 Y. Le Coat, R. Azria and M. Tronc, J. Phys. B, 15 (1982) 1569.
118 J.K. Olthoff, J.A. Tossell and J.H. Moore, J. Chem. Phys., 83 (1985) 5627.
119 I. Illenberger, Ber. Bunsenges. Phys. Chem., 86 (1982) 247.
120 M. Allan and S.F. Wong, J. Chem. Phys., 74 (1981) 1687.
121 E.N. Lassettre, A. Skerbele and V.D. Meyer, J. Chem. Phys., 45 (1966) 3214.
122 E.N. Lassettre, A. Skerbele, M.A. Dillon and K.J. Ross, J. Chem. Phys., 48 (1968) 5066.
123 J. Mazeau, in M. Matic (Ed.), The Physics of Ionized Gases, Invited Lectures and Progress Reports, SPIG'80, Dubrovnik, Yugoslavia, 1980, p. 97.
124 D. Spence and P.D. Burrow, J. Phys. B, 12 (1979) L179.

125 J. Mazeau, F. Gresteau, R.I. Hall and A. Huetz, J. Phys. B, 11 (1978) L557.
126 A. Loftus and P.H. Krupenie, J. Phys. Chem. Ref. Data, 6 (1977) 113.
127 J. Geiger and B. Schröder, J. Chem. Phys., 50 (1969) 7.
128 E.N. Lassettre, Can. J. Chem., 47 (1969) 1733.
129 G. Joyez, R.I. Hall, J. Reinhardt and J. Mazeau, J. Electron Spectrosc. Relat. Phenom., 2 (1973) 183.
130 M. Leoni and K. Dressler, J. Appl. Math. Phys. ZAMP, 22 (1971) 794.
131 K. Dressler and M. Leoni, in E.E. Koch, R. Haensel and C. Kunz (Eds.), Vacuum Ultraviolet Radiation Physics, Pergamon/Vieweg, Braunschweig, 1974, p. 179.
132 A. Chutjian, D.C. Cartwright and S. Trajmar, Phys. Rev. A, 16 (1977) 1052.
133 S.W. Sharpe and P.M. Johnson, J. Chem. Phys., 85 (1986) 4943.
134 D. Stahel, M. Leoni and K. Dressler, J. Chem. Phys., 79 (1983) 2541.
135 E.S. Chang and K. Yoshino, J. Phys. B, 16 (1983) L581.
136 H. Lefebvre and C.M. Moser, J. Chem. Phys., 43 (1965) 1394.
137 T. Betts and V. McKoy, J. Chem. Phys., 54 (1971) 113.
138 S. Chung, C.C. Lin and E.T.P. Lee, J. Chem. Phys., 82 (1985) 342.
139 S. Trajmar, D.F. Register and A. Chutjian, Phys. Rep., 97 (1983) 219.
140 D. Spence, J. Chem. Phys., 66 (1977) 669.
141 D.W. Turner, C. Baker, A.D. Baker and C.R. Brundle, Molecular Photoelectron Spectroscopy, Wiley-Interscience, London, 1970.
142 D. Spence, Phys. Rev. A, 15 (1977) 883.
143 R. Haas, Z. Phys., 148 (1957) 177.
144 G.J. Schulz, Phys. Rev. A, 135 (1964) 988.
145 D.T. Birtwistle and A. Herzenberg, J. Phys. B, 4 (1971) 53.
146 A.G. Engelhardt, A.V. Phelps and C.R. Risk, Phys. Rev. A, 135 (1964) 1566.
147 A.V. Phelps, Rev. Mod. Phys., 40 (1968) 399.
148 M. Allan, J. Phys. B, 18 (1985) 4511.
149 M. Tronc and L. Malegat, in F.A. Gianturco and G. Stefani (Eds.), Lecture Notes in Chemistry, Vol. 35, Springer, 1984, p. 24.
150 J. Mazeau, F. Gresteau, R.I. Hall and J. Reinhardt, J. Phys. B, 6 (1973) 862.
151 H. Hotop and W.C. Lineberger, J. Phys. Chem. Ref. Data, 4 (1975) 539.
152 J. Mazeau, C. Schermann and G. Joyez, J. Electron Spectrosc. Relat. Phenom., 7 (1975) 269.
153 B. Wallbank, S. Daviel, J. Comer and P.J. Hicks, J. Phys. B, 16 (1983) 3065.
154 P. Hammond, G.C. King, J. Jureta and F.H. Read, J. Phys. B, 18 (1985) 2057.
155 K. Kimura, S. Katsumata, Y. Achiba, T. Yamazaki and S. Iwata, Handbook of He I Photoelectron Spectra of Fundamental Organic Molecules, Japan Scientific Societies Press, Tokyo; Halsted Press, New York, 1981.
156 N. Swanson, R.J. Celotta, C.E. Kuyatt and J.W. Cooper, J. Chem. Phys., 62 (1975) 4880.
157 D.S. Newman, M. Zubek and G.C. King, J. Phys. B, 16 (1983) 2247.
158 W.M. Huo, H. Pritchard, K. Watari, M.A.P. Lima and V. McKoy, in J. Geddes, H.B. Gilbody, A.E. Kingston, C.J. Latimer and H.J.R. Walters (Eds.), Abstr. 15th ICPEAC, Brighton, 1987, p. 290.
159 J. Mazeau, F. Gresteau, G. Joyez, R. Reinhardt and R.I. Hall, J. Phys. B, 5 (1972) 1890.
160 D.G. Wilden and J. Comer, J. Phys. B, 13 (1979) 627.
161 L. Sanche and M. Michaud, Chem. Phys. Lett., 80 (1981) 184.
162 A. Bolovinos, J. Philis, E. Pantos, P. Tsekeris and G. Andritsopoulos, J. Chem. Phys., 75 (1981) 4343.
163 J. Philis, A. Bolovinos, G. Andritsopoulos, E. Pantos and P. Tsekeris, J. Phys. B, 14 (1981) 3621.
164 K. Krogh-Jespersen, R.P. Rava and L. Goodman, Chem. Phys. Lett., 64 (1979) 413.

165 P.D. Burrow, J.A. Michejda and K.D. Jordan, J. Am. Chem. Soc., 98 (1976) 6392.
166 D. Mathur and J.B. Hasted, J. Phys. B, 9 (1976) L31.
167 R. Azria and G.J. Schulz, J. Chem. Phys., 62 (1975) 573.
168 S.F. Wong and G.J. Schulz, Phys. Rev. Lett., 35 (1975) 1429.
169 H. Estrada, L. Cederbaum and W. Domcke, J. Chem. Phys., 84 (1986) 152.
170 J. Comer and F.H. Read, J. Phys. B, 4 (1971) 368.
171 M. Allan, Chem. Phys., 81 (1983) 235.
172 R.A. Dressler and M. Allan, Chem. Phys. Lett., 118 (1985) 93.
173 P.T. Murray and T. Baer, Int. J. Mass Spectrom. Ion Phys., 30 (1979) 165.
174 G. Dujardin, S. Leach, O. Dutuit, T. Govers and P.-M. Guyon, J. Chem. Phys., 79 (1983) 644; P.-M. Guyon and L.F.A. Ferreira, Electronic versus Vibronic Autoionization, Invited Paper, Workshop on Atomic and Molecular Autoionization, Argonne Natl. Laboratory, 1985.
175 H.-P. Fenzlaff and E. Illenberger, Int. J. Mass Spectrom. Ion Processes, 59 (1984) 185.
176 M.D. Robin, Higher Excited States of Polyatomic Molecules, Vol. III, Academic Press, New York, 1985, p. 359.
177 K.C. Smyth, J.A. Schiavone and R.S. Freund, J. Chem. Phys., 61 (1974) 1789.
178 A.P. Hitchcock and C.E. Brion, J. Electron Spectrosc. Relat. Phenom., 10 (1977) 317.
179 J.A. Horsley, J. Stöhr, A.P. Hitchcock, D.C. Newbury, A. Johnson and F. Sette, J. Chem. Phys., 83 (1985) 6099.
180 J. Kuhn, P. Čársky and R. Zahradník, Collect. Czech. Chem. Commun., 39 (1974) 2175.
181 E. Lindholm and L. Asbrink, Lecture Notes in Chemistry, Vol. 38, Molecular Orbitals and their Energies, Studied by the Semiempirical HAM Method, Springer, Berlin, 1985.
182 F. Benett and W. Hug, unpublished results, 1982.
183 E. Haselbach and A. Schmelzer, Helv. Chim. Acta, 54 (1971) 1299.
184 T. Bally and B. Albrecht, 1987, unpublished results; program available from T. Bally upon request.
185 T. Shida and S. Iwata, J. Am. Chem. Soc., 95 (1973) 3473.
186 G.A. George and G.C. Morris, J. Mol. Spectrosc., 26 (1968) 67.
187 E.E. Koch, A. Otto and K. Radler, Chem. Phys. Lett., 16 (1972) 131.
188 D.M. Hanson and G.W. Robinson, J. Chem. Phys., 45 (1965) 4174.
189 E.B. Priestley and A. Haug, J. Chem. Phys., 49 (1968) 622.
190 R.H. Huebner, S.R. Mielczarek and C.E. Kuyatt, Chem. Phys. Lett., 16 (1972) 464.
191 N.M. Pisanias, L.G. Christophorou and J.G. Carter, Chem. Phys. Lett., 13 (1972) 433.
192 J.R. Platt, J. Chem. Phys., 17 (1949) 484.
193 O.C. Hofer and R.M. Hedges, Chem. Phys. Lett., 6 (1970) 67.
194 R.A. Dressler, L. Neuhaus and M. Allan, J. Electron Spectrosc. Relat. Phenom., 31 (1983) 181.
195 B. Dick and G. Hohlneicher, Chem. Phys. Lett., 84 (1981) 471.
196 M. Allan, in F.A. Gianturco and G. Stefani (Eds.), Lecture Notes in Chemistry, Vol. 35, Springer, Berlin, 1984, p. 14.
197 B. Dick and G. Hohlneicher, Chem. Phys. Lett., 83 (1981) 615.
198 L.E. Lyons and G.C. Morris, J. Mol. Spectrosc., 4 (1960) 480.
199 D. Rund and H. Port, Chem. Phys., 78 (1983) 357.
200 R.E. Kellog, J. Chem. Phys., 44 (1966) 411.
201 R. Pariser, J. Chem. Phys., 23 (1956) 250.
202 M.R. Padhye, S.P. McGlynn and M. Kasha, J. Chem. Phys., 24 (1956) 588.
203 H. Fukumura, K. Kikuchi and H. Kokubun, Chem. Phys. Lett., 92 (1982) 29.
204 M. Beer and H.C. Longuet-Higgins, J. Chem. Phys., 23 (1955) 1390.
205 W.G. Herkstroeter, J. Am. Chem. Soc., 97 (1975) 4161.
206 D. Klemp and B. Nickel, Chem. Phys., 78 (1983) 17.

207 E. Heilbronner and K. Wieland, Helv. Chim. Acta, 30 (1947) 947.
208 O.E. Weigang, Jr., J. Chem. Phys., 33 (1960) 892.
209 T. Kitagawa, Y. Harada, H. Inokuchi and K. Kodera, J. Mol. Spectrosc., 19 (1966) 1.
210 M.D. Robin, Higher Excited States of Polyatomic Molecules, Vol. II, Academic Press, New York, 1975.
211 E.W. Thulstrup, P.L. Case and J. Michl, Chem. Phys., 6 (1974) 410.
212 W. Gerhartz and J. Michl, J. Am. Chem. Soc., 100 (1978) 6877.
213 R. Boschi, E. Clar and W. Schmidt, J. Chem. Phys., 60 (1974) 4406.
214 J.H.D. Eland and C. Danby, Z. Naturforsch., Teil A, 23 (1968) 355.
215 M.D. Robin, Higher Excited States of Polyatomic Molecules, Vol. III, Academic Press, New York, 1985, p. 379.
216 P.D. Burrow, personal communication.
217 G.J. Verhaart, P. Brasem and H.H. Brongersma, Chem. Phys. Lett., 62 (1979) 519.
218 R.H. Huebner, W.F. Frey and R.N. Compton, Chem. Phys. Lett., 23 (1973) 587.
219 I. Nykl, A. Fojtík, P. Hobza, P. Čársky, R. Zahradník and T. Shida, Collect. Czech. Chem. Commun., 38 (1973) 1459.
220 P. Čársky and R. Zahradník, Top. Curr. Chem., 43 (1973) 1.
221 W.E. Wentworth, E. Chen and J.E. Lovelock, J. Phys. Chem., 70 (1966) 445.
222 E.P. Grimsrud, S. Chowdhury and P. Kebarle, J. Chem. Phys., 83 (1985) 3983.
223 R.P. Frueholz, W.M. Flicker, O.A. Mosher and A. Kuppermann, J. Chem. Phys., 70 (1979) 1986.
224 J.P. Doering and R. McDiarmid, J. Chem. Phys., 75 (1981) 87.
225 P. Bischof, J.A. Hashmall, E. Heilbronner and V. Hornung, Helv. Chim. Acta, 52 (1969) 1745.
226 R. Hoffmann, E. Heilbronner and R. Gleiter, J. Am. Chem. Soc., 92 (1970) 706; R. Hoffmann, Acc. Chem. Res., 4 (1971) 1.
227 M.D. Robin and N.A. Kuebler, J. Chem. Phys., 44 (1966) 2664.
228 K.D. Jordan, J.A. Michejda and P.D. Burrow, Chem. Phys. Lett., 42 (1976) 227.
229 W.-C. Tam and C.E. Brion, J. Electron Spectrosc. Relat. Phenom., 3 (1974) 467.
230 W.T. Naff, R.N. Compton and C.D. Cooper, J. Chem. Phys., 57 (1972) 1303.
231 E.H. Van Veen, W.L. Van Dijk and H.H. Brongersma, Chem. Phys., 16 (1976) 337.
232 K.N. Walzl, C.F. Koerting and A. Kuppermann, J. Chem. Phys., 87 (1987) 3796.
234 C. Benoit, R. Abouaf and S. Cvejanovic, Abstr. 11ème Colloque sur la Physique des Collisions Atomiques et Moleculaires, Metz, France, June 1986, p. 42.
235 C. Benoit, R. Abouaf and S. Cvejanovic, Chem. Phys., 117 (1987) 295.
236 R.A. Dressler and M. Allan, J. Electron Spectrosc. Relat. Phenom., 41 (1986) 275.
237 E. Lindholm, private communication, 1987.
238 G. Lucazeau and C. Sandorfy, J. Mol. Spectrosc., 35 (1970) 214.
239 S. Taylor, D.G. Wilden and J. Comer, Chem. Phys., 70 (1982) 291.
240 H.W. Jochims, W. Lohr and H. Baumgärtel, Chem. Phys. Lett., 54 (1978) 594.
241 G.J. Fisanick and T.S. Eichelberger IV, J. Chem. Phys., 74 (1981) 6692.
242 E. Illenberger, J. Chem. Phys., 88 (1988) 7453.
243 H.M. Rosenstock, K. Draxl, B.W. Steiner and J.T. Herron, J. Phys. Chem. Ref. Data, 6 (1977) Suppl. 1. Quoted by R. Bombach, J.-P. Stadelmann and J. Vogt, Chem. Phys., 60 (1981) 293.
244 G.B. Ellison, P.C. Engelking and W.C. Lineberger, J. Am. Chem. Soc., 100 (1978) 2556.
245 J.W.C. Johns, S.H. Priddle and D.A. Ramsay, Discuss. Faraday Soc., 35 (1963) 90.
246 E. Veltin, E. Heilbronner and H. Labhart, Helv. Chim. Acta, 46 (1963) 2041.
247 R. Hagen, E. Heilbronner and P.A. Straub, Helv. Chim. Acta, 50 (1967) 2504.
248 H. Hosoya and S. Nagakura, Theor. Chim. Acta, 8 (1967) 319.
249 H. Kuroda and T. Kunii, Theor. Chim. Acta, 7 (1967) 220.

250 H. Yamaguchi, Y. Amako and H. Azumi, Tetrahedron, 24 (1967) 267.
251 Z. Yoshida and T. Kobayashi, Theor. Chim. Acta, 20 (1971) 216.
252 G. Buemi, F. Zuccarello and A. Raudino, J. Mol. Struct. (Theochem), 76 (1981) 137.
253 M. Allan, E. Heilbronner and E. Kloster-Jensen, J. Electron Spectrosc. Relat. Phenom., 6 (1975) 181.
254 P.D. Burrow and K.D. Jordan, J. Am. Chem. Soc., 104 (1982) 5247.
255 K.N. Houk, Y.-M. Chang and P.S. Engel, J. Am. Chem. Soc., 97 (1975) 1824.
256 M.J. Mirbach, K.-Ch. Liu, M.F. Mirbach, W.R. Cherry, N.J. Turro and P.S. Engel, J. Am. Chem. Soc., 100 (1978) 5122.
257 W.D.K. Clark and C. Steel, J. Am. Chem. Soc., 93 (1971) 6347.
258 A. Modelli and P.D. Burrow, J. Phys. Chem., 88 (1984) 3550.
259 H. Ehrhardt, D.L. Langhans, F. Linder and H.S. Taylor, Phys. Rev., 173 (1968) 222.
260 C. Mündel, M. Berman and W. Domcke, Phys. Rev. A, 32 (1985) 181.
261 W. Domcke and C. Mündel, in D.C. Lorents, W.E. Meyerhof and J.R. Peterson (Eds.), Electronic and Atomic Collisions, Elsevier, Amsterdam, 1986, p. 195.
W. Domcke, C. Mündel and L.S. Cederbaum, Comments. At. Mol. Phys., 20 (1987) 293.
262 H. Ehrhardt and K. Willmann, Z. Phys., 204 (1967) 462.
263 M.J.W. Boness and G.J. Schulz, Phys. Rev. A, 8 (1973) 2883.
264 G.J. Schulz, in G. Bekefi (Ed.), Principles of Laser Plasmas, John Wiley, New York, 1976, Chap. 2; also reprinted in S.C. Brown (Ed.), Electron-Molecule Scattering, Wiley Interscience, 1979, Chap. 1.
265 M. Berman, A. Estrada, L.S. Cederbaum and W. Domcke, Phys. Rev. A, 28 (1983) 1363.
266 W. Domcke, N. Berman, H. Estrada, C. Mündel and L.S. Cederbaum, J. Phys. Chem., 88 (1984) 4862.
267 B.M. Nestman and S.D. Peyerimhoff, J. Phys. B, 18 (1985) 4309.
268 W.M. Huo, T.L. Gibson, M.A.P. Lima and V. McKoy, Phys. Rev. A, 36 (1987) 1632.
269 J.M. Launay and M. LeDourneuf in J. Geddes, H.B. Gilbody, A.E. Kingston, C.J. Latimer and H.J.R. Walters (Eds)., Abstr. 15th ICPEAC, Brighton, 1987, p. 288.
270 W. Domcke and L.S. Cederbaum, Phys. Rev. A, 16 (1977) 1465.
271 L. Dubé and A. Herzenberg, Phys. Rev. A, 20 (1979) 194.
272 B.I. Schneider, M. LeDourneuf and Vo Ky Lan, Phys. Rev. Lett., 43 (1979) 1926.
273 L.S. Cederbaum and W. Domcke, J. Phys. B, 14 (1981) 4665.
274 L.A. Morgan, J. Phys. B, 19 (1986) L439.
275 M. Tronc and R. Azria, in I. Shimamura and M. Matsuzawa (Eds.), Invited Papers, Symposium on Electron-Molecule Collisions, University of Tokyo, 1979, p. 105.
276 A. Chutjian and H. Tanaka, J. Phys. B, 13 (1980) 1901.
277 R. Azria, S.F. Wong and G.J. Schulz, Phys. Rev. A, 11 (1975) 1309.
278 L. Andric and R.I. Hall, J. Phys. B, 17 (1984) 2713.
279 L. Dubé and A. Herzenberg, Phys. Rev. A, 11 (1975) 1314.
280 I.C. Walker, A. Stamatovic and S.F. Wong, J. Chem. Phys., 69 (1978) 5532.
281 G.A. Gallup, Phys. Rev. A, 34 (1986) 2746.
282 N.M. Pisanias, L.G. Christophorou, J.G. Carter and D.L. McCorkle, J. Chem. Phys., 58 (1973) 2110.
283 D.F. Dance and I.C. Walker, Proc. R. Soc. London, Ser. A, 334 (1973) 259.
284 C.D. Cooper, W.T. Naff and R.N. Compton, J. Chem. Phys., 63 (1975) 2752.
285 A. Modelli, D. Jones, S. Rossini and G. Distefano, Chem. Phys. Lett., 123 (1986) 375.
286 M. Allan, L. Neuhaus and E. Haselbach, Helv. Chim. Acta, 67 (1984) 1776.
287 M. Allan, Abstr. 10th Colloque sur la Physique des Collisions Atomiques et Electroniques, Aussois, France, 1984, p. 32.
288 I. Cadez, F. Gresteau, M. Tronc and R. Hall, J. Phys. B, 10 (1977) 3821.

289 M.-J. Hubin-Franskin and J.E. Collin, J. Electron Spectrosc., Relat. Phenom., 7 (1975) 139.
290 D.F. Dance, G.A. Keenan and I.C. Walker, J. Chem. Soc. Faraday Trans. 2, 74 (1978) 440.
291 S. Cvejanovic, J. Jureta and D. Cvejanovic, J. Phys. B, 18 (1985) 2541.
292 I. Suzuki, J. Mol. Spectrosc., 25 (1968) 479.
293 J. Ozment, D.T. Chuljan and J. Simons, J. Chem. Phys., 82 (1985) 4199.
294 H.S. Taylor, Int. J. Quantum Chem., 31 (1987) 747.
295 J.P. Gauyacq, in J. Geddes, H.B. Gilbody, A.E. Kingston, C.J. Latimer and H.J.R. Walters (Eds.), Abstr. 15th ICPEAC, Brighton, 1987, p. 301.
296 J.P. Gauyacq, Progress Report, SPIG'88, Sarajevo, Yugoslavia, 1988, to be published.
297 G.H. Wannier, Phys. Rev., 90 (1953) 817.
298 S. Cvejanovic and F.H. Read, J. Phys. B, 7 (1974) 1841.
299 D. Spence, Phys. Rev. A, 11 (1975) 1539.
300 J.M. Phillips, J. Phys. B, 15 (1982) 4259.